THE ORTHO TO PARA TRANSITION IN MUONIC MOLECULAR HYDROGEN

A Dissertation

Presented to

The Faculty of the Department of Physics

The College of William and Mary in Virginia

In Partial Fulfillment

Of the Requirements for the Degree of

Doctor of Philosophy

---

by

Jessica H.D. Clark

2002

APPROVAL SHEET

This dissertation is submitted in partial fulfillment of

the requirements for the degree of

Doctor of Philosophy

Jessica H.D. Clark

Approved, October 2002

David S. Armstrong

Marc Sher

J. Dirk Walecka

Robert E. Welsh

Marvin Blecher
Virginia Polytechnic Institute and State
University

For my family
and dear friends.

CONTENTS

ACKNOWLEDGMENTS

I am overwhelmed by the amount of support and encouragement I have been given over these years of graduate school. Without all of you, this process could not have been as rewarding as it has been. I have made every attempt to recognize everyone who should be thanked; however, I realize the danger in making a list like this. If I have forgotten you, please understand that the omission is unintentional.

Experiment Support

I need to thank everyone on the TRIUMF E766 collaboration: David Armstrong, Tim Gorringe, Mike Hasinoff, Dennis Wright, Paul King, Piotr Żołnierczuk, Sugata Tripathi, and Trevor Stocki. I am grateful for the friendship and companionship of Trevor, Piotr, and Sugata during our time at TRIUMF. I would also like to thank Tim and Mike for their guidance and leadership during the experiment and data analysis.

I would like to recognize the TRIUMF support staff for their help during the experiment. The following TRIUMF technical staff were instrumental in the setup and maintenance of the experiment: Dennis Healey (target), Walter Kellner (target), Pierre Amaudruz (DAQ), Willi Anderson (solenoid), and Grant Sheffer (electronics). I would also like to thank Rich Helmer, Glen Marshall, and Elie Korkmaz for the use of their liquid scintillators and Willi Bertl for the loan of the protium storage and gas handling system.

During the engineering run in November 1996, Rhett Woo, Ermias Gete, and

Belal Moftah provided additional support. Two UBC summer students (Greg Orosi and David Caplan) assisted during the Summer 1999 run. The initial Monte Carlo code development and simulation work for the experimental design was performed by Paige (McKenzie) Varner (thanks for leaving me a great project, Paige).

The following organizations provided financial support for both personnel and equipment: The Jeffress Foundation, The William and Mary Endowment, NSF, NSERC, and the Henry Luce Foundation (Clare Boothe Luce Fellowship Program).

I would like to thank the members of my committee and other readers for their careful reading of this dissertation.

APS Support

I have to, of course, thank everyone at the American Physical Society for their support over the past two(+) years. Judy Franz and Tom McIlrath are very relieved that I have finally completed my degree. Alan Chodos has been more patient and understanding during this entire process than I have probably deserved, but without his encouragement I may never have finished.

To all my friends at the APS—Vinaya, Sara, Arlene, Laleña, James, and the rest of the gang— don't worry, I promise not to stop showering now that I'm a "full-fledged" physicist!

William and Mary Support

When I took my first physics course as a freshman at the College of William and Mary in 1991, I had no idea that I had stumbled into a place that would come to mean a great deal to me over the years. The supportive and friendly environment provided by the exceptional faculty and staff in this department make it an ideal place to learn and grow. I am especially grateful to those faculty in the Physics Department that have provided support and even friendship over the years—Dirk

Walecka, Gene Tracy, Morty Eckhause, and Marc Sher.

Every W&M physics graduate student over the past 20-30 years knows that this department would be nothing without Sylvia Stout, Dianne Fannin, and Paula Perry. These three women are always there to provide a shoulder, a good laugh, or anything else you may need. Their love and friendship have helped me through some tough times and I will always be grateful to them.

I also need to recognize some of the other graduate students who came to be special friends over the years—my office mate Eric (I can't believe we finally made it), my old lunch-buddy Bryan, and the amazing and wonderful Paul King. And, I am grateful to all the graduate students who added fun to my life over the years.

Personal Support

I truly believe that I never could have made it through without all the love and support I received from my family and dear friends. My parents were always quick to offer love when I was down, and encouragement when I needed a boost. My father even provided me with a home that I could call my own. The "Little Mother" was always a bright spot in my life. And, I am grateful that my brother, Josh, and I continue to build a friendship based on mutual experiences and respect. To the rest of my family, I am thankful for your love. I will always be sad that Papa didn't get to see the end of this process, but I know that he would have been endlessly proud of my accomplishment!

My friends, especially Lissa, Amy, and Lisa, were unending in their love and encouragement during the good and bad times. I hope I can repay the favor one day.

Arlene Modeste Knowles provided hours and hours of coaching while I was writing this dissertation. She helped me work through my muddled explanations and even "talked me off the ledge" during the more difficult sections and the dreaded

figure captions. She is in training to become a professional coach, and I am confident that there will be no end to what her clients will achieve with her support.

And this acknowledgment section wouldn't be the same if I didn't recognize all the unconditional love I've received over the years from my beloved furry friends.

And Finally...

There are two people without whom this dissertation would not exist. First, Pat Hausman has served over the past three years as Mom, "roommate," and dear, dear friend. She provided me with a Home (in every meaning of the word) in Williamsburg after I moved to Maryland. My trips to the College would not have been as productive or enjoyable without her. These past years have presented Pat with formidable challenges and changes. She has reacted to each one with a grace and dignity that I can only hope to emulate one day. I have learned much from her and am endlessly grateful for her friendship.

Finally, I need to express my deep gratitude and appreciation to my advisor and friend, David Armstrong. As an advisor he has repeatedly gone above and beyond the call of duty. I have heard graduate school compared to a marathon. For the first 18 miles, David was always there, giving me gentle encouragement. For the last eight miles, his job became more difficult (especially since I moved to Maryland and took a full-time job). He had to figure out ways to keep pushing me towards the end. And for the final two miles I'd say that he had to pick me up and throw me across the finish line[1]. I realize that I may never have finished without his added effort. He is a truly gifted mentor, and I am proud to call him a friend. Thank you!

[1] Thanks for the analogy, Sue!

LIST OF TABLES

LIST OF FIGURES

ABSTRACT

A precise measurement of the induced weak pseudoscalar coupling constant of the proton, g_p, is of interest as a basic test of chiral symmetry breaking. This is the least well-known weak form factor of the nucleon. Muon capture experiments [Jonkmans *et al.*, Phys. Rev. Lett. **77**(1996)4512] have been used to measure g_p. However, the interpretation of these muon capture experiments requires knowledge of the relative population of the muonic atomic and molecular states for muons in liquid hydrogen. In particular, λ_{op}, the transition rate between the ortho- and para-molecular states of the $p\mu p$ molecule, needs to be known with precision. The only previous measurement [Bardin *et al.*, Phys. Lett. **104B**(1981)320.] of λ_{op} yielded a value of $(4.1 \pm 1.4) \times 10^4$ s^{-1}, significantly different than the theoretical prediction [Bakalov *et al.*, Nucl. Phys. **A384**(1982)302.] of 7.1×10^4 s^{-1}. A measurement of λ_{op} using the time distribution of neutrons from muon capture was performed at TRIUMF during June-July 1999 and November 1999. The λ_{op} measured in this experiment is $(13.8 \pm 1.6) \times 10^4$ s^{-1}. The uncertainty is dominated by the statistical precision of the fit and the background due to the deuterium contamination in the protium target. The implications of this result for g_p are discussed.

THE ORTHO TO PARA TRANSITION IN MUONIC MOLECULAR HYDROGEN

CHAPTER 1

Theoretical Motivation and Background

1.1 Introduction

Quantum chromodynamics, QCD, is the fundamental quantum field theory of the strong interaction which binds quarks, through the exchange of gluons, into the observed hadronic (strongly interacting) particles. However, unlike quantum electrodynamics, QCD is not calculable using perturbation theory at 'large' ($\geq 10^{-15}$ m) distances or 'low' energies (< 1 GeV). This means that perturbative QCD cannot be used to directly calculate hadronic structure. Therefore, the description of hadronic structure and low-energy interactions at present must be based on theoretical models. One can use the basic symmetries of QCD to guide development of these models, but experimental observations are critical for determining model parameters and for testing the assumptions used. And, since hadrons comprise 99.9 % of the mass of the visible universe, understanding their structure and interactions is crucial to our understanding of the universe.

The experiment described in this thesis is motivated by the use of the muon as a leptonic probe of the proton's structure and its weak couplings; of particular interest is the induced pseudoscalar coupling, g_p, of the proton. The process used is the capture of a bound negative muon on a proton. When muons are used in this manner, it is crucial to understand the muonic molecular physics of the initial system involving the proton and muon. This experiment is designed specifically to investigate one aspect of these molecular effects, the ortho-para transition in muonic molecular hydrogen (λ_{op}), in order to allow g_p to be extracted from previous

measurements of muon capture. It should be noted as an aside, however, that these muonic molecular effects are themselves of intrinsic interest, for example in the investigation of muon-catalyzed fusion.

1.2 Overview of Weak Interactions

The weak interaction governs processes that change a quark or lepton of a given flavor into a different flavor. The weak interaction is also unique in that it violates parity, charge conjugation, and time-reversal invariance. Unlike the strong force which affects only hadrons, fundamental weak interactions affect both hadrons and leptons.

This work primarily deals with the weak process of negative muon capture, described by

$$\mu^- + p \rightarrow n + \nu_\mu \tag{1.1}$$

and at the quark level by

$$\mu^- + u \rightarrow d + \nu_\mu \ . \tag{1.2}$$

Some properties of the muon are listed in Table 1.1. The effective weak inter-

Spin	$\frac{1}{2}\ \hbar$
Mass	$106\,\mathrm{MeV/c^2}$
Charge	$\pm e = 1.6 \times 10^{-19}$ C
Mean lifetime	$2.197\,\mu$s

Table 1.1: Some properties of the muon [1].

action Hamiltonian for this process has the form

$$\mathcal{H}_W(\mathbf{x}) = -\frac{G_F}{\sqrt{2}} J_\lambda^\dagger(\mathbf{x}) J^\lambda(\mathbf{x}) + h.c. \tag{1.3}$$

where G_F is the Fermi coupling constant and J_λ is the weak current. J_λ can

be described as

$$J_\lambda(\mathbf{x}) = J_\lambda^h + J_\lambda^l \ , \tag{1.4}$$

that is, the sum of the hadronic (J_λ^h) and leptonic (J_λ^l) components of the weak current. Muon capture is classified as a semi-leptonic weak interaction, meaning that the weak current is not purely leptonic, as in muon decay ($\mu^- \to e^- + \nu_\mu + \overline{\nu_e}$), but involves hadrons, and therefore the strong interaction, as well.

Leptonic current

Leptons couple weakly through two-component fields expressed in the following form

$$\phi \equiv \frac{1}{2}(1-\gamma_5)\psi \ . \tag{1.5}$$

In general, the lepton current in the weak Hamiltonian takes the general form

$$J_\lambda^l = \overline{\phi}_a O_i \phi_b = \frac{1}{4}\overline{\psi}_a(1+\gamma_5)O_i(1-\gamma_5)\psi_b \tag{1.6}$$

where ψ_j are the lepton fields and O_i represents the following operators:

$$\begin{aligned} \text{scalar, } S &= 1 \\ \text{pseudoscalar, } P &= \gamma_5 \\ \text{tensor, } T &= \sigma_{\mu\nu} \\ \text{vector, } V &= \gamma_\mu \\ \text{axial vector, } A &= \gamma_\mu\gamma_5 \end{aligned} \tag{1.7}$$

where γ_i and $\sigma_{\mu\nu}$ are the Dirac γ-matrices and Pauli matrices. For scalar, pseudoscalar, or tensor operators the current is experimentally found to vanish. Empirically, the leptonic component of the current is found to have the following form

$$J_\lambda^l = \overline{\psi}_a \gamma_\lambda (1-\gamma_5)\psi_b \ . \tag{1.8}$$

This "V-A" coupling is now understood to be a particular case of the electroweak theory [2, 3, 4] in the limit of low energy. This V-A theory has been tested extensively using purely leptonic processes such as muon decay.

Hadronic current

In a semileptonic weak process like muon capture, the strong interactions of the quarks induce extra structure in the hadronic currents. The basic V-A form remains, but the individual vector and axial vector current terms include couplings which are functions of the momentum transfer of the process (*i.e.* can be described using form factors). These induced couplings are required as part of a complete description of the structure of the nucleon.

The most general vector and axial vector components of the hadronic current are

$$V_\lambda = i\overline{\psi}_n \left[g_v \gamma_\lambda + \frac{g_m}{2M_N} \sigma_{\lambda\nu} q_\nu + i \frac{g_s}{m_\mu} q_\lambda \right] \psi_p \tag{1.9}$$

and

$$A_\lambda = -\overline{\psi}_n \left[g_a \gamma_\lambda \gamma_5 + i \frac{g_p}{m_\mu} \gamma_5 q_\lambda + i \frac{g_t}{2M_N} \sigma_{\lambda\nu} q_\nu \gamma_5 \right] \psi_p \tag{1.10}$$

where M_N and m_μ are the nucleon and muon masses. The g_α are coupling "constants" which are, in general, complex functions of q^2, the four-vector momentum transfer between the neutron and proton ($q = p_n - p_p$ where p_n and p_p are the proton and neutron momenta). The terms g_v and g_a are the conventional vector and axial vector coupling constants. In purely leptonic interactions these constants are the only ones that contribute and each have a value of one, resulting in $\gamma_\lambda(1 - \gamma_5)$ (V − A) current structure. The other coupling constants g_m, g_p, g_s, and g_t measure the strength of the "induced" weak magnetic, pseudoscalar, scalar, and tensor currents respectively.

1.2.1 Determination of the Weak Coupling Constants

The induced coupling constants are restricted by several theoretical constraints on both strong and weak interactions. The strong interaction is invariant under G-parity, which is a combination of a rotation in isospace and charge conjugation. Therefore, under a G-parity transformation, the induced currents in V_λ and A_λ must be symmetric. However, the g_s and g_t currents do not conserve G-parity which implies

$$\begin{aligned} g_s &= 0 \ , \\ g_t &= 0 \ . \end{aligned} \tag{1.11}$$

To this date, no convincing experimental evidence of the existence of these currents has been found [5].

Just as electric charge must be conserved in electromagnetic theory, the conserved vector current hypothesis (CVC) [6] requires that the weak vector current be conserved, *i.e.*,

$$\partial_\lambda V_\lambda = 0 \ . \tag{1.12}$$

CVC establishes a connection between electromagnetism and weak interactions by relating the weak vector and isovector electromagnetic currents. Hence, g_v and g_m can be expressed in terms of the electromagnetic form factors of the nucleon (as functions of q^2) which can be obtained from elastic electron scattering reactions, such as those performed at the Thomas Jefferson National Accelerator Facility [7]. The low energy limits for these currents are

$$\begin{aligned} g_v &= 1 \ , \\ g_m &= 3.706 \end{aligned} \tag{1.13}$$

as $q^2 \to 0$. A part of the electroweak part of the Standard Model, CVC has been well verified experimentally.

Unlike the weak vector current, the axial vector current A_λ is not exactly conserved (if it were, the pion would not decay). The two remaining coupling terms, g_a and g_p, may be constrained by the partially conserved axial vector current (PCAC) hypothesis [8, 9], which states that A_λ would only be conserved in a world with massless pions. Therefore, the divergence of the axial current is assumed to be proportional to the pion field, ϕ_π, *i.e.*

$$\begin{aligned} \partial_\lambda A_\lambda &= f_\pi m_\pi^2 \phi_\pi \\ &\xrightarrow{m_\pi \to 0} 0 \end{aligned} \tag{1.14}$$

where f_π is the pion decay constant and m_π is the pion mass. PCAC can be applied to A_λ to show that

$$2M_N g_a - q^2 \frac{g_p}{m_\mu} = \frac{\sqrt{2} f_\pi m_\pi^2 G_{\pi NN}}{q^2 + m_\pi^2} \tag{1.15}$$

where $G_{\pi NN}$ is the strong coupling constant for the pion-nucleon vertex. As $q^2 \to 0$, this expression reduces to

$$g_a = \frac{f_\pi G_{\pi NN}}{\sqrt{2} M_N} = 1.32 \pm 0.02 \ , \tag{1.16}$$

referred to as the Goldberger-Treiman relation [10], where

$$G_{\pi NN}(0) = G_{\pi NN}(q^2) = G_{\pi NN} \tag{1.17}$$

that is, that the off-mass shell behavior of the pion-nucleon coupling is assumed to vary slowly with q^2. This estimate for g_a is slightly different from the value measured using neutron β-decay, $g_a = 1.262 \pm 0.005$ [11]. The (5%) difference between these values is called the Goldberger-Treiman discrepancy [12]. Using equation (1.15), the relation between g_a and g_p can be expressed as

$$g_p = \left[\frac{2 M_N m_\mu}{q^2 + m_\pi^2} \right] g_a \ . \tag{1.18}$$

This relation shows that g_p has a pole at the pion mass. A simple interpretation is that single pion exchange (the lightest available pseudoscalar particle) dominates the

induced pseudoscalar contribution (g_p). Despite the fact that g_p is a strong function of q^2, its value at a specific q^2 is often used as a reference point. For ordinary muon capture (OMC) on the proton

$$\mu^- + p \rightarrow n + \nu_\mu \tag{1.19}$$

the kinematics give

$$q^2 = 0.88 m_\mu^2 \ . \tag{1.20}$$

Using this relation, equation (1.18) yields

$$g_p = 7.1 g_a = 8.56 \ . \tag{1.21}$$

The prediction for g_p given above is often referred to as either the PCAC prediction, the Goldberger-Treiman value, or the Wolfenstein estimate; it has not been well-verified experimentally (see Section 1.4). Expressed in terms of the weak currents, g_p is proportional to the momentum transfer q. Therefore, its effect on low momentum-transfer processes such as β-decay is negligible. However, the effect of g_p is measurable in muon capture processes where q^2 is much larger, and the corresponding observables are consequently much more sensitive to g_p.

The PCAC hypothesis is not firmly grounded theoretically. The value of g_p can also be predicted in more modern terms based on the chiral symmetries of QCD. This approach, using heavy baryon, or nucleon, chiral perturbation theory (HBχPT), provides a systematic low-energy expansion of the effective strong interaction with an expansion parameter of $\mathcal{O}(m_\pi/M_N)$. Applying this method [13] yields

$$\begin{aligned} g_p &= \frac{2 m_\mu G_{\pi NN} f_\pi}{m_\pi^2 + q^2} - \frac{1}{3} g_a(0) m_\mu M_N r_A^2 + \text{higher}-\text{order terms} \\ &= 8.44 \pm 0.23 \end{aligned} \tag{1.22}$$

where r_A^2 is the axial radius of the nucleon, defined through $g_a(q^2) = g_a(0)(1 + q^2 r_A^2/6 + \mathcal{O}(q^4))$. The original Goldberger-Treiman relation dominates as the first

term in the expansion with the remaining correction terms following from χPT. To quote Bernard, Kaiser, and Meissner [13],

> "... an accurate empirical determination of this quantity [g_p] therefore poses a stringent test of the underlying dynamics which is believed to be realized in the effective low-energy theory of QCD (*i.e.* chiral perturbation theory). "

1.3 Muon Chemistry

Of the six induced coupling constants, g_p is the least well-determined experimentally (more on this in Section 1.4). As stated earlier, g_p is a strong function of q^2; therefore, the large momentum transfer of muon capture makes it the main source of information on g_p, as opposed to low momentum transfer processes like β-decay or e-capture. The simplest observable dependent on g_p is then the rate of muon capture on the proton.

There are, however, inherent experimental difficulties in performing muon capture experiments. The outgoing particles—neutrons and neutrinos—are difficult to detect. The rate of muon capture scales by Z^4, where Z is the number of protons in the nucleus [14], making experiments performed on complex nuclei more feasible. However, it is theoretically unclear if g_p remains unchanged within this nuclear medium. In addition, nuclear structure uncertainties make the extraction of g_p sensitive observables difficult within complex nuclei. Therefore, although adversely affected by a low capture rate, muon capture on a free proton is preferred since it avoids these nuclear uncertainties.

Since the weak interaction is spin-dependent, the capture rates for muonic atoms are strongly dependent on the initial spin state of the system. In order to interpret muon capture experiments, the details of the relevant muonic atomic and molecular states of the initial system must be understood.

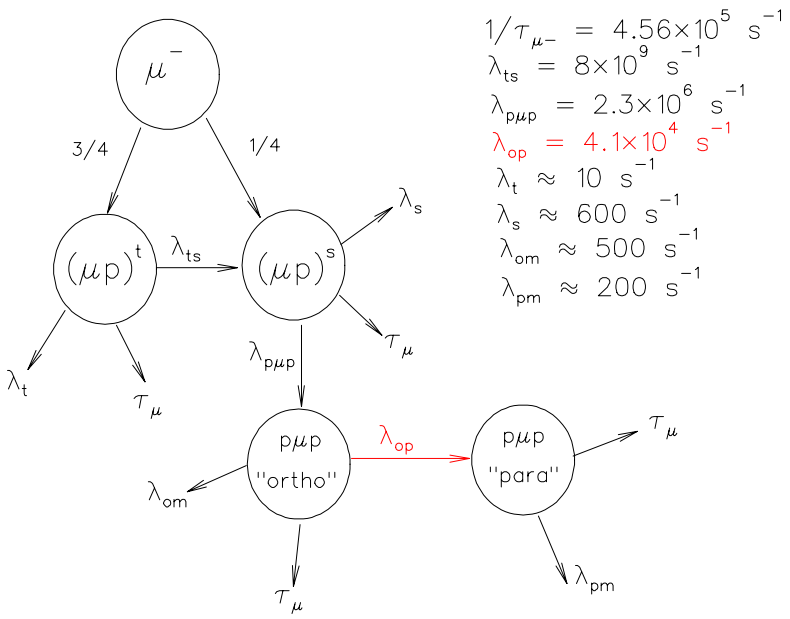

Figure 1.1: Kinetics of μ^- stopping in protium (isotopically pure, deuterium-depleted hydrogen). All transition rates are normalized to liquid-hydrogen density. The value of λ_{op} indicated is from Bardin *et al.* [15].

When a μ^- is brought to rest in hydrogen, a muonic atom is formed. The μp atom is initially formed in a highly excited state. The atom then de-excites through Auger emission of the atomic electron and radiative decay, and eventually reaches the $n = 1$ ground state [16]. The resulting ground-state μp atom is 200 times smaller than a regular hydrogen atom. The μp atom is formed in a statistical mixture of $\frac{1}{4}$ singlet ($F = 0$) and $\frac{3}{4}$ triplet ($F = 1$) hyperfine states, but the $F = 1$ state is rapidly ($\lambda_{ts} \approx 1$ ns) converted to the singlet ground state. The μp atom can collide with other H_2 molecules forming, through Auger emission, a $p\mu p$ molecule. The formation rate of the molecule is $\lambda_{p\mu p} = 2.3 \times 10^6\,\mathrm{s}^{-1}$. (See Figure 1.1 for a pictorial representation of the muon history in hydrogen.) The $p\mu p$ molecule has a para-molecular ground state and a higher-energy ortho-molecular state. Table 1.2 shows the quantum numbers for each $p\mu p$ state. The ortho and para states have different compositions in terms of singlet and triplet μp components. The ortho state is $\frac{3}{4}$

	orbital angular momentum	nuclear spin
ortho	$L = 1$	$I = 1$
para	$L = 0$	$I = 0$

Table 1.2: Quantum numbers of the $p\mu p$ molecule.

singlet, $\frac{1}{4}$ triplet, while the para state is $\frac{1}{4}$ singlet and $\frac{3}{4}$ triplet. The conversion rate of the ortho state to the para state is represented by λ_{op}. The determination of this de-excitation rate in liquid hydrogen is the goal of this thesis. Figure 1.2 shows the principal atomic and molecular states and transitions relevant to muon capture by the proton.

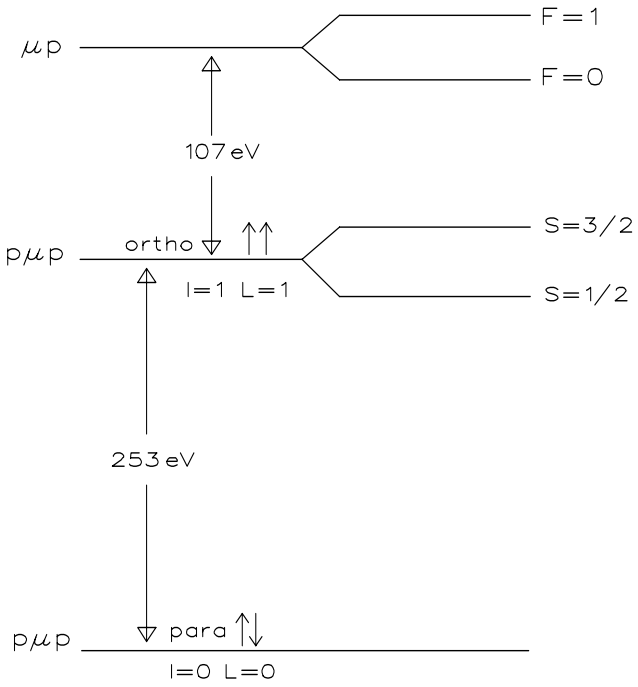

Figure 1.2: Simplified representation of the energy levels and hyperfine splittings of the μp and $p\mu p$ system. A discussion of the transitions between the energy levels is given in Section 1.5. A more detailed version of this diagram can be found in Bakalov *et. al.* [17]. The measurement of the transition rate between the ortho and para energy states is the goal of this thesis.

At any point along this progression from a free μ^- to a μp atom to a $p\mu p$ molecule, the μ^- can just decay. In fact, 99.9% of the time it does decay, while 0.1% of the time the muon is captured on the proton instead. The muon capture

rate differs drastically among the different initial spin states of the μp system. The capture rate from the triplet state, λ_t, is $\approx 12\,\mathrm{s}^{-1}$, while the rate from the singlet state, λ_s, is dramatically faster, $\approx 660\,\mathrm{s}^{-1}$ [18]. The contrasting mixtures of singlet and triplet in the ortho- and para-molecular states, therefore imply that the capture rates in these two molecular states λ_{om} and λ_{pm} are correspondingly different. Thus, a knowledge of the relevant fraction of molecules in the ortho and para state in the experimental target is essential for the interpretation of muon capture in hydrogen experiments. A more detailed discussion of the molecular formation and energy transitions follows in Section 1.5.

1.4 Measurements of g_p in Hydrogen

A large body of work exists concerning experimental measurements of g_p for protons in complex nuclei. Although interesting, this work will not be discussed here. Reference [19] gives a current review of this field.

Recall that there are daunting experimental difficulties associated with muon capture on a free proton, mainly arising from the small branching ratio ($\sim 10^{-3}$) for this process. Consequently, there have only been a handful of measurements of g_p to date for the free proton. The situation is summarized in Table 1.3. In all, there are eight separate measurements, using differing techniques and observables.

Early Measurements

The first six hydrogen measurements involved direct detection of the monoenergetic, 5.2 MeV recoil neutrons from muon capture. The first two experiments [21, 20] were bubble chamber studies and the large error bars were due to statistics limitations. The next two experiments [22, 23] utilized liquid hydrogen for higher statistics but significant backgrounds and difficulty determining detector efficiencies produce large errors making these values rather imprecise. The fifth and sixth ex-

Experiment/ Location	Target	Technique	extracted g_p, for $\lambda_{op} = 0$	extracted g_p, for $\lambda_{op} = 4.1 \times 10^4\,\mathrm{s}^{-1}$
CERN-Bologna[20] (1962)	Bubble Chamber	neutron	17.3 ± 5.1	15.5 ± 5.1
Chicago[21] (1962)	Bubble Chamber	neutron	19.6 ± 8.4	17.7 ± 8.9
Columbia[22] (1962)	Liquid H_2	neutron	8.6 ± 7.9	6.0 ± 8.0
Columbia[23] (1963)	Liquid H_2	neutron	13.4 ± 4.2	11.0 ± 4.3
CERN-Bologna[24] (1969)	Gas H_2	neutron	7.9 ± 5.9	
Dubna[25] (1974)	Gas H_2	neutron	10.3 ± 3.9	
Saclay[15, 26, 27] (1981)	Liquid H_2	electron; lifetime	13.8 ± 2.0	7.1 ± 3.0
TRIUMF[28, 29] (1995)	Liquid H_2	photon (RMC)	13.3 ± 1.3	12.6 ± 1.3

Table 1.3: Experimental results for g_p from muon capture on a proton. To show the dependence of each measurement on the value of λ_{op}, the values of g_p are given for two different ortho-para conversion rates. Unless otherwise noted, each experiment utilized ordinary muon capture. The technique is indicated by the particle detected. The χPT prediction is 8.44 ± 0.23. An earlier version of this table is given in Ref. [15]. The extracted values for g_p are modified when recent improvements to the values of g_a and τ_{μ^+} are applied [30]. This will be discussed in Chapter 4.

periments [24, 25] in this group are the only ones using gaseous targets. Although also limited by statistics, these measurements are not dependent on the effects of λ_{op}, unlike the first four.

Lifetime measurement

A newer technique, used by a group at Saclay, determined the muon capture rate by comparing the effective lifetime of μ^- in liquid hydrogen ($l\mathrm{H}_2$) to that of μ^+ [15, 26]. The difference between the two lifetimes is due to muon capture, which does not take place for μ^+. That difference can be used to deduce the capture rate. They detected the muon decay electrons in six three-layer plastic scintillator telescopes surrounding a 24 cm diameter liquid protium (isotopically pure, deuterium-depleted hydrogen) target. The target walls were Cu so that μ^-s stopping in walls disappeared rapidly. The μ^- beam arrived in $3\mu s$ long bursts pulsed at 3000 Hz. The resulting time spectra were recorded out to $65\mu s$ after each beam-burst. Multiple event rejection was applied in the electronics. A total of 1.3×10^5 events was recorded resulting in a 30 ppm measurement of τ_{μ^-}. Comparing τ_{μ^-} to τ_{μ^+} yielded $\lambda_{capture} = (460 \pm 20)\,\mathrm{s}^{-1}$. The result for g_p extracted from this $\lambda_{capture}$ depends on λ_{op}. Using the value for λ_{op} as determined by this same group in their neutron measurement (discussed below in Section 1.5.2), the value $\lambda_{om} = (531 \pm 33)\mathrm{s}^{-1}$ was extracted which yields $g_p = 7.1 \pm 3.0$, in reasonable agreement with the prediction of Equation 1.22.

There are three key features of this result. The lifetime technique avoids the difficult task of detecting the 5.2 MeV neutrons. However, an extremely precise measurement of the lifetimes is needed. This particular measurement is extra sensitive to λ_{op} due to the time "blank" used in the experiment— 1μs after the end of a 3μs beam-burst.

The Saclay group averaged their g_p result with those of the previous measure-

ments' published values[1], resulting in a World Average of

$$g_p^{world} = 8.7 \pm 1.9 \ , \tag{1.23}$$

also in reasonable agreement with the prediction of Equation 1.22. As pointed out by Gorringe and Fearing [30], this measured value of g_p is modified somewhat when recent improvements to the values of g_a and τ_{μ^+} are applied.

Radiative Muon Capture

The most recent and most precise measurement of g_p was the first to measure the relatively rare process of radiative muon capture (RMC) by a free proton [28, 29], described by

$$\mu^- + p \rightarrow n + \nu_\mu + \gamma \tag{1.24}$$

where the energy of the radiated photon ranges up to 105 MeV. The experiment used a $l\mathrm{H}_2$ (liquid hydrogen) target[2] on the M9A beam line channel at TRIUMF (see Chapter 2). The radiated photons were detected in a large-solid-angle, medium resolution e^+e^- pair spectrometer based on a four-layer cylindrical drift chamber. The branching ratio (B.R.) for this process is very low; therefore, backgrounds were a major difficulty in this measurement. After background subtraction, 279 ± 26 events were collected, yielding a branching ratio of $(2.10 \pm 0.21) \times 10^{-8}$. Using Beder and Fearing's calculation [31] of the RMC process, this B.R. corresponds to

$$g_p^{RMC} = 12.4 \pm 0.9 \pm 0.4 \ . \tag{1.25}$$

where the first error represents statistical and systematic uncertainties and the second error is due to the uncertainty in λ_{op} (see Section 1.5.2).

Recall that the χPT (and PCAC) theory prediction for g_p is 8.44 ± 0.23, which, at face value, is in agreement with the g_p^{world} result from ordinary muon capture

[1] The first two bubble chamber measurements were only released in conference proceedings.
[2] The same target used by the present experiment, described in Chapter 2.

(OMC). The newer RMC value is in sharp disagreement with the χPT prediction. However, the relative dependencies of these measurements on the molecular complication of λ_{op} can be seen in Figure 1.3. As will be discussed in the next section, the only previous experimental and theoretical results for λ_{op} do not agree. Clearly, an improved measurement of this quantity is needed for the interpretation of these results. This is the key motivation for this thesis.

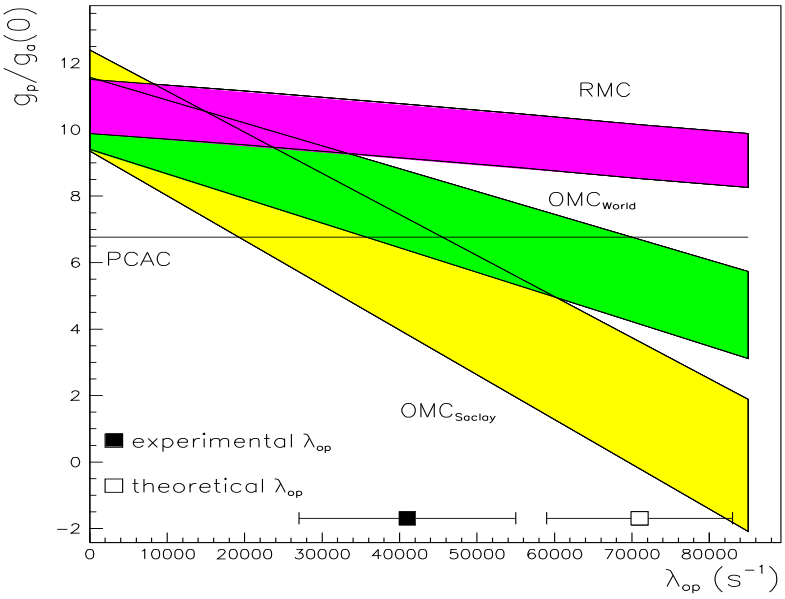

Figure 1.3: The pseudoscalar coupling g_p determined from radiative muon capture (RMC), the Saclay ordinary muon capture (OMC_{Saclay}) experiment, and the world average of all OMC measurements, OMC_{World} *vs.* the ortho-para transition rate λ_{op}. The PCAC (χPT) prediction is noted, as well. The previous experimental and theoretical values for λ_{op} (see Section 1.5) are indicated.

1.5 The Ortho to Para Transition

The importance of the formation of the $p\mu p$ molecule in collisions of the μp atom with H_2 molecules was recognized early on; pioneering theoretical work came from Weinberg [32], and independently from Zel'dovich and Gershtein [33]. The μ^- binds the two protons covalently into a small, charge = +1 object (this net charge prevents μ^- transfer from the $p\mu p$ to higher-Z impurities). Recall that there

are two bound states of the $p\mu p$, the "para" ground state with rotational angular momentum L=0 and total nuclear spin I=0, and the "ortho" state, 148 eV higher in energy, with L=1 and I=1. Initial theoretical work [32, 33], indicated that λ_{op} was negligible.

The formation of the $p\mu p$ by electron ejection in a collision of the μp with H_2 is an E0 process for the para state and E1 (electric dipole) for the ortho state, and so direct para formation is strongly inhibited; detailed calculations by Ponomarev and Faifman [34] yield $\lambda_{p\mu p}^{\rm ortho} = 2.2 \times 10^6$ s^{-1} and $\lambda_{p\mu p}^{\rm para} = 7.2 \times 10^3$ s^{-1}, in good agreement with experiment ($\lambda_{p\mu p} = (2.3 \pm 0.3) \times 10^6$ s^{-1} for the sum of both $p\mu p$ states).

1.5.1 Theoretical Prediction for λ_{op}

Bakalov *et al.* [17] used a relativistic treatment of the three-body system, $p\mu p$, to calculate λ_{op}. The total nuclear spin, I, and S, the total spin of the molecule, are not exactly conserved quantities in a relativistic treatment. Total momentum, J=S+L, is, however, conserved. The calculation involves the expansion of the exact wavefunction in a limited basis of non-relativistic states, with an anticipated error of 10 % in λ_{op} due to the use of this truncated basis.

Conversion between the ortho and para states via E1 radiative or Auger emission is forbidden in a non-relativistic approximation by the selection rule ΔI=0. However, within the molecule, spin interactions produce admixtures of large and small components of spinors within the wavefunction in each of the states. The nuclear spin, I, of the large components in the ortho state is equal to that of the small components in the para state and *vice versa*. Therefore, 'large' $\leftrightarrow$ 'small' electric dipole transitions can occur. Thus, relatively fast E1 transitions can happen mainly via Auger emission, in which an atomic electron is ejected electromagnetically. This is sometimes referred to as 'internal conversion,' as in nuclear physics. The radia-

tive transition, in which a real photon is emitted instead, is much slower for the $p\mu p$ molecule and can be safely neglected.

Since the ortho-para transition will proceed mainly via Auger emission of an atomic (or molecular) electron, the electronic environment in which the $p\mu p$ muonic system is embedded is clearly of crucial importance. The $p\mu p$ molecule is small and compact, with mass and charge not unlike the deuteron nucleus. The $p\mu p$ molecule can bond with other hydrogen atoms within the system, forming a mesic molecular complex with both 'muonic' (the $p\mu p$ system) and 'electronic' (the H atom) bonding, *i.e.* $[(p\mu p)pe]^+$. The positively charged $p\mu p$ can bind with an electron to form the neutral $(p\mu p)e$ system, analogous to the deuterium atom. Adopting the notation of Ponomarev, this system is denoted as M≡$[(p\mu p)\ e]$. In analogy with a more familiar system, the $p\mu p$ can be formed in an electronically bound system $(MH)^+$, similar to a deuteron in an $(HD)^+$ molecular ion. Thus the exotic *muonic* molecule functions as a close analog of a nucleus hidden in an ordinary *electronic* hydrogen molecule.

The $(MH)^+$ ion, once formed, can then interact with ordinary H_2 molecules forming the following three ion-molecular complexes[3]:

$$(MH)^+ + H_2 \longrightarrow \begin{cases} MH + H_2^+ & \text{(a)} \\ MH_2^+ + H & \text{(b)} \\ M + H_3^+ & \text{(c)} \end{cases} . \tag{1.26}$$

The relative Auger conversion rates for these three complexes ($K_a, K_b,$ and K_c) scale with the electron density at the $p\mu p$ location and the values are known[4], as are the relative formation rates of these complexes ($W_a, W_b,$ and W_c). With these known, only ${\lambda_{op}}^{(a)}$ is needed in order to calculate λ_{op}. Using the truncated basis calculation described above, Bakalov *et al.* calculated ${\lambda_{op}}^{(a)} = (9.5 \pm 1.0) \times 10^4\,\mathrm{s}^{-1}$. Using the known or calculated values of $K_a, K_b,$ and K_c and $W_a, W_b,$ and W_c, they then arrived

[3]Again, these reactions are analogous to the well-known reactions $DH^+ + H_2 \rightarrow DH + H_2^+$, $DH^+ + H_2 \rightarrow DH_2^+ + H$, *etc.*

[4]with relative error 10% [17]

at

$$\lambda_{op} = (7.1 \pm 1.2) \times 10^4\,\mathrm{s}^{-1}. \tag{1.27}$$

The uncertainty in the prediction arises from (1) the error in the relative values of K_a, K_b, K_c ($\approx 12\%$) and (2) $\approx 10\%$ in ${\lambda_{op}}^{(a)}$ due to the truncated basis.

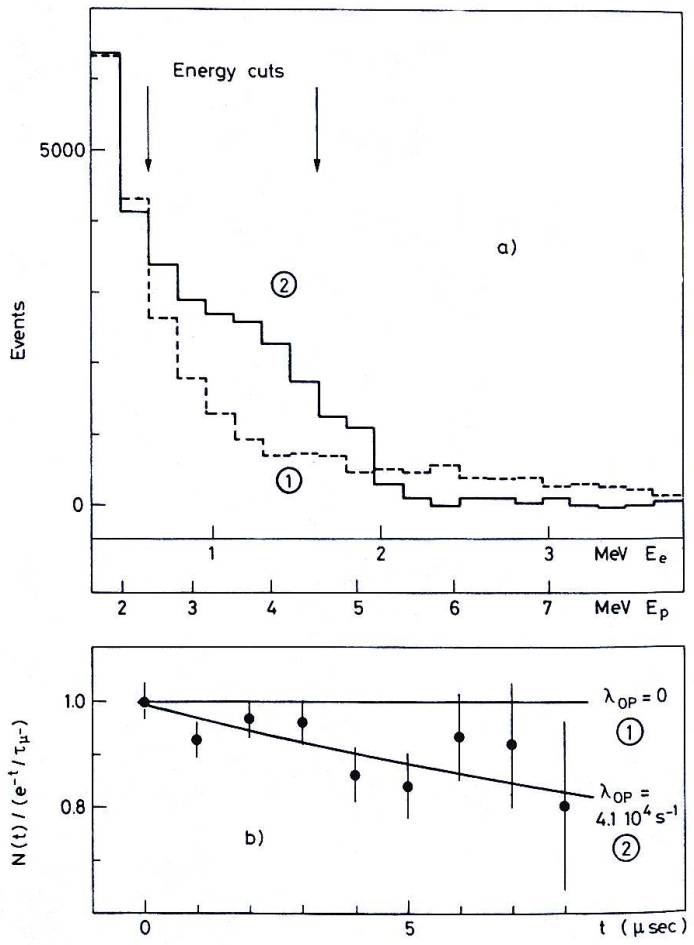

Figure 1.4: Results of the only previous measurement of λ_{op} [15, 27]. a) Neutron energy spectrum showing ①the background and ②the background-subtracted spectrum; energy window for 5.2 MeV neutron window indicated; b) time dependence of 5.2 MeV neutron candidates (points) with expected time distribution for two values of λ_{op} (lines). The data have had the free muon exponential decay divided out. For more information, see [15, 27].

1.5.2 Experimental Measurement of λ_{op}

The only previous direct measurement of λ_{op} is by Bardin *et al.* at Saclay [15, 27], using a similar setup to that of the g_p experiment by the same group de-

scribed in Section 1.4. That experiment detected the OMC neutrons using six liquid scintillation counters in conjunction with plastic scintillators for charged particle vetoes. Two complementary pulse shape discrimination (PSD) techniques were used to distinguish neutron events from photons. The experiment yielded 18000 "good" neutron events (Fig. 1.4 a) out of 45000 candidate events within a 3–5 MeV energy window and a time window starting 1.5 μs after the beam pulse and running for 7 μs, with 1 μs bins. Substantial backgrounds, each with different time dependencies, arose from cosmic rays, pileup of two photons[5], muon capture in the Cu target walls, and neutrons from photonuclear (γ, n) reactions. A complex, non-exponential distortion in the time spectrum resulted from accelerator-related, time-dependent backgrounds.

The resulting time spectrum is shown in Fig. 1.4b, where the characteristic μ^- lifetime has been divided out. From the effective neutron lifetime, $\tau_n^{\mu^-} = (2084 \pm 30)$ ns, the extracted value[6] for λ_{op} is

$$\lambda_{op} = (4.1 \pm 1.4) \times 10^4 \text{ s}^{-1} \quad . \tag{1.28}$$

Note the discrepancy with the theoretical estimate of $(7.1 \pm 1.2) \times 10^4$ s^{-1}. The experimental error was dominated by the relatively poor statistics and the signal/noise of about 1.5 : 1 in the time spectrum.

While the Bardin *et al.* experiment represents the only available direct measurement of λ_{op}, the same collaboration inferred a value from their earlier decay-electron lifetime measurement of OMC [26, 35]; this gave the result $(7.7 \pm 2.7) \times 10^4$ s^{-1} which is consistent with their direct measurement (albeit with larger errors), but was not published [35].

[5]These events can mimic the shape of a neutron event and pass the neutron conditions of the PSD.

[6]The slightly different value $\lambda_{op} = (4.61 \pm 1.35) \times 10^4$ s^{-1} is given in G. Bardin's PhD thesis [27] which is dated well after the publication [15], and so is presumably the best value.

There are two principal differences between the measurement by Bardin *et al.* and the experiment which will be described in the following chapter. The first involves the use of a continuous wave (CW, or high duty-factor) μ^- beam as opposed to the pulsed, low duty-factor beam at Saclay. The second difference is the use of modern multi-hit time encoding electronics.

1.6 Summary

The pseudoscalar coupling, g_p, is an important and poorly known aspect of proton structure. The experimental situation for g_p on a free proton is clouded by muonic molecular physics—in particular, by the poor knowledge of the ortho to para transition rate λ_{op}. The only previous experimental measurement of λ_{op} has large uncertainties and does not agree well with the theoretical calculation. This provides the motivation for the work presented in this thesis.

CHAPTER 2

Description of Experiment

The experiment was performed on the M9B beam channel at the Tri-University Meson Facility (TRIUMF), in Vancouver, Canada. The data were obtained in two production running periods during June-July 1999 and November 1999. A preliminary engineering run took place in November 1996. The technique used in this experiment was to measure the time spectra of neutrons resulting from muon capture. To this purpose, three main components are required: a clean, relatively intense μ^- beam, a high-purity liquid hydrogen target, and neutron detection with good ability to distinguish neutrons from gammas.

2.1 Muon Beam

The TRIUMF accelerator is a sector-focused, azimuthally-varying field cyclotron. Negatively-charged hydrogen ions are accelerated towards a thin carbon foil which strips off the two electrons leaving a proton traveling in an oppositely curved path along a beamline out of the cyclotron. Depending on the location of the carbon foil, the accelerator produces proton beam energies between 183 and 520 MeV with currents up to 140 μA. In normal operating conditions the proton beam is delivered in 3 nsec pulses every 43 nsec with a 99 % macroscopic duty-factor.

Currently, there are four beamlines extracted from the cyclotron and used for experiments. Beamline BL4(p) is utilized for proton-induced reaction studies. BL2C(p) is used for low-current, medical proton therapy in treating eye cancer. The newly commissioned BL2A(p) feeds into the Isotope Separator and ACcelerator Facility, ISAC. Finally, BL1(p) is used for pi meson production. The resulting

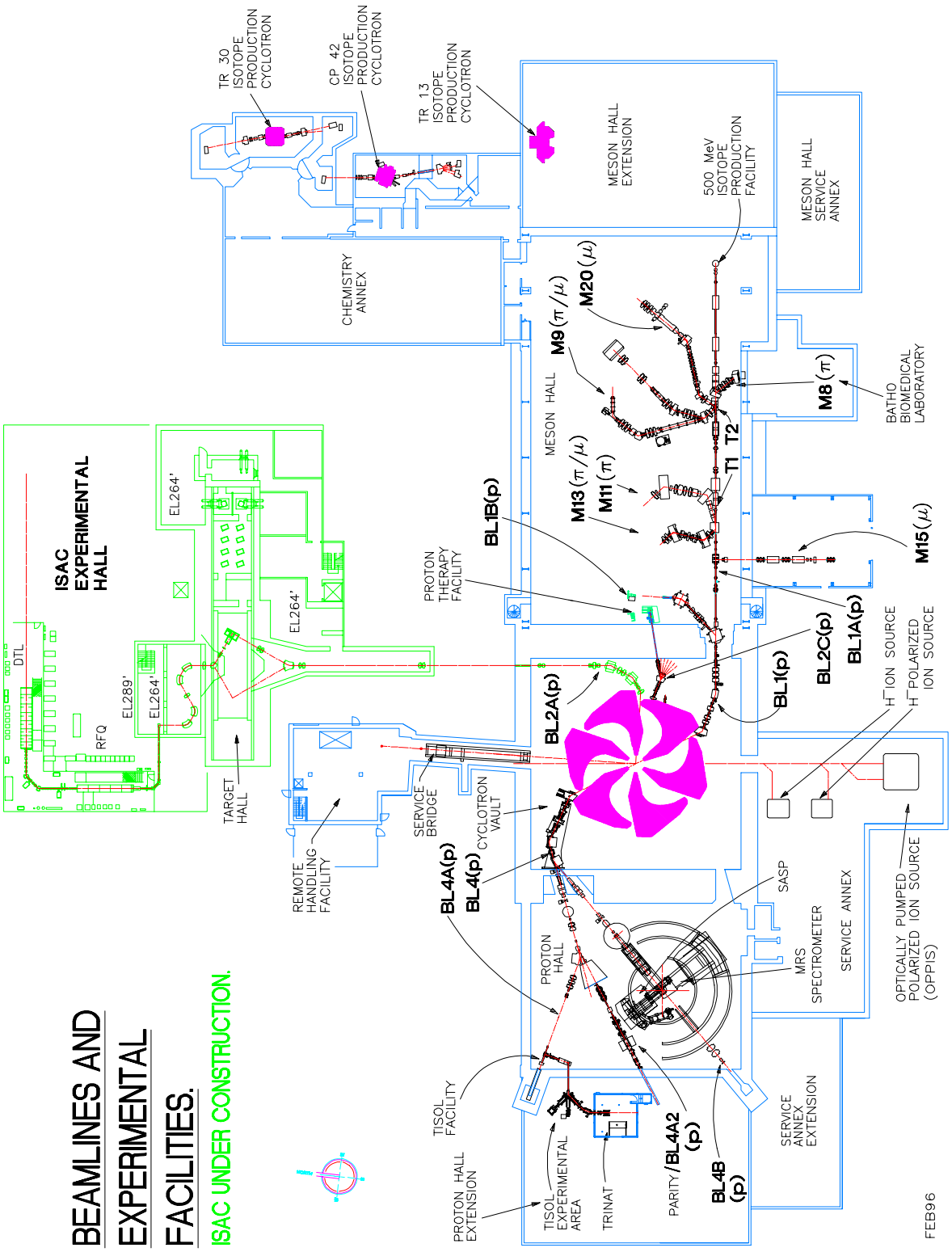

Figure 2.1: TRIUMF cyclotron and beamlines[36].

pion beam can be used directly or, if the pions are allowed to decay, a secondary muon beam can be utilized. Figure 2.1 shows the layout of the cyclotron and its beamlines.

The M9B channel (shown in Figure 2.2 with its "sister" leg, M9A) can provide either pion or muon beams. The pion beam is produced when the primary proton beam, BL1A, strikes the meson production target IAT2, typically a water-cooled piece of beryllium[1]. The resulting pion beam is steered down the M9B channel where a series of magnets can be tuned to direct either pions or muons[2] into the experimental area. In this experiment a muon beam was used mainly; the pion beam was only used in brief calibration runs. The muon beam has a pion contamination of less than 0.2 % and consists of approximately 5 % electrons. A beam momentum of $\sim$65 MeV/c was used for the production runs in this experiment.

2.1.1 Beam Telescope Counters

The beam telescope consisted of two scintillation counters, S1 and S2. Their dimensions are listed in Table 2.1. After the beam exits the channel (and vacuum) through a thin, mylar window the muons passed through S1. Before entering the target, the muons then passed through the smaller, "beam-defining" S2. A coincidence of S1 and S2 defines a muon stop. The timing of the muon stop is defined by the thicker S1.

Beam Counter	Dimensions (cm)	High Voltage (V)
S1	$33.02 \times 33.02 \times 0.32$	-2000
S2	$10.16 \times 10.16 \times 0.16$	-1820

Table 2.1: Beam counter dimensions.

[1] 100 mm thick along the beam axis, with cross-sectional area 5 mm $\times$ 15 mm.

[2] A superconducting solenoid is used to collect low-momentum muons from the in-flight decay of the beam pions.

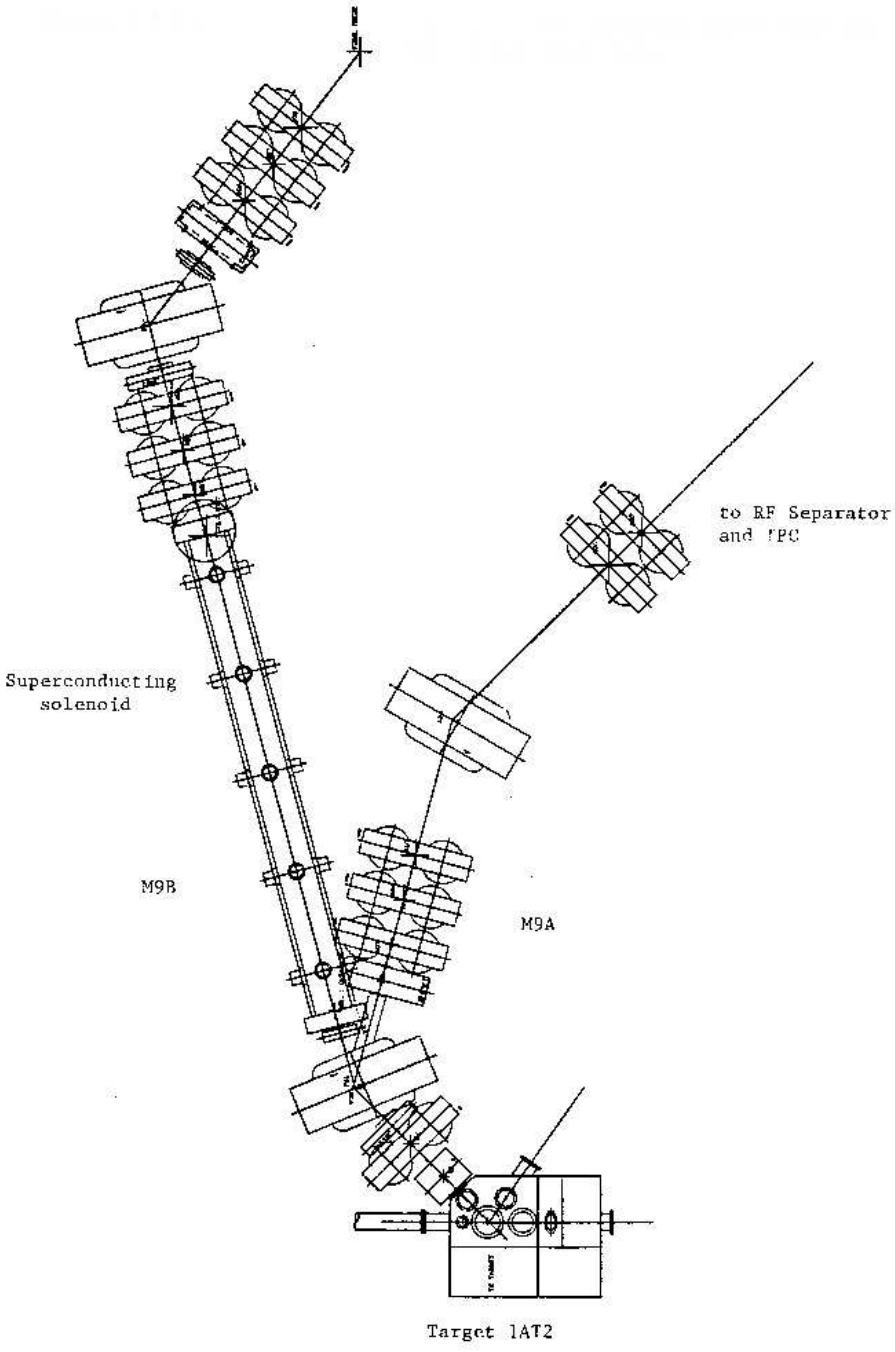

Figure 2.2: The M9 channel [36].

2.2 Target

The experiment utilized the large-volume, liquid H_2 target originally designed for and used in the RMC measurement [28, 29, 37]. The cylindrical target holds ~ 2.7 liters and measures 16 cm in diameter and 15 cm in length. The cylindrical flask wall and dome-shaped front face are made of gold measuring 0.25 mm in thickness. The flask is surrounded by two silver heat shields each 0.51 mm thick and a silver vacuum jacket 1.02 mm thick. The window of the vacuum jacket is a 0.25 mm thick film of aluminized mylar. Immediately downstream of the window is a 22.5 μm thick aluminized mylar film followed by another 2.5 μm thick. Within the vacuum and immediately upstream of the target flask is the cylindrical, internal beam collimator with silver walls 0.76 mm thick. Figure 2.3 shows a schematic of the target.

Since muon capture scales with $\sim Z^4$, the potential for large backgrounds from target impurities dictates the usage of both isotopically and elementally pure hydrogen. Impurities from higher-Z elements are kept at a level below 1 ppb by passing the protium through a palladium filter while the target is filled [38]. The isotopic purity of the deuterium-depleted hydrogen (referred to as "protium") was measured periodically throughout the experiment. As shown in Table 2.2, subsequent analysis of the gas samples [39] shows the deuterium concentration to be on the ppm level.

Date gas sample taken	Deuterium content in ppm (atomic)
30-11-99	4 ± 2
7-7-99	sample lost
11-11-99	4 ± 2
16-11-99	4 ± 2

Table 2.2: Deuterium content in gas samples taken directly from target during the two production runs.

The potential background from muons stopping in the target flask or walls

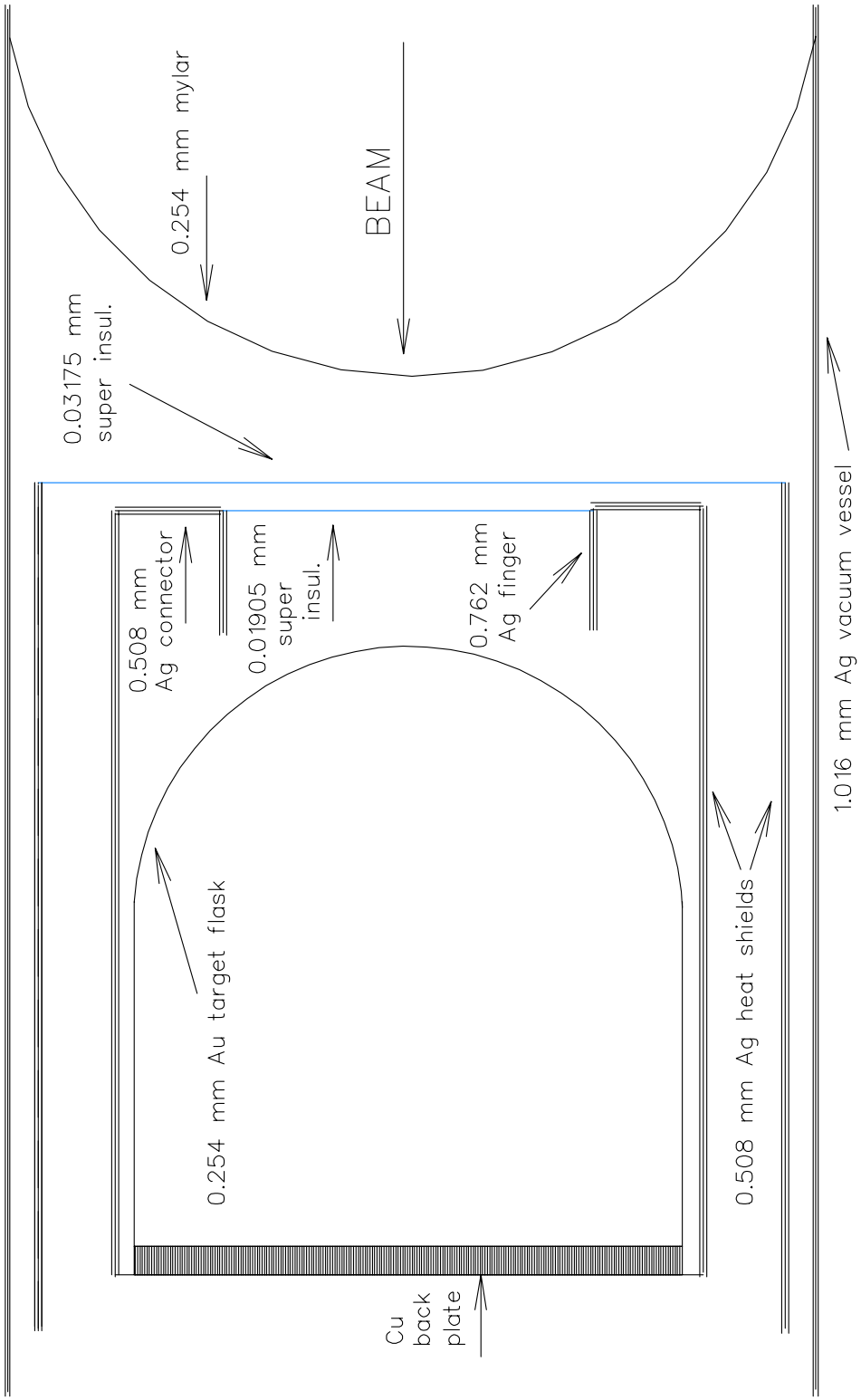

Figure 2.3: Protium Target. Schematic of protium target flask and surrounding components. The target holds 2.7 liters and is 16 cm in diameter and 15 cm in length.

prompted the usage of gold and silver in the make-up of the target. Muons stopping in the gold flask walls have a disappearance mean lifetime of 73.5 ns [40], as opposed to a 2.2 μs lifetime in protium. Likewise, the muons stopping in the silver components around the target have a disappearance lifetime of 88.1 ns. Muon stops in the gold and silver can be excluded from the analysis because of their fast disappearance time compared to the protium signal[3].

2.3 Neutron Detection

Five similar (but not identical) liquid scintillation neutron detectors were used to detect the neutrons from muon capture. They were located roughly symmetrically in azimuth around the target, as shown in Figure 2.5. The photograph in Figure 2.4 shows the target with the five neutron detectors, the charged particle vetoes, and S2. Table 2.3 lists the characteristics and dimensions of each detector.

Detector	Dim. (cm)	Material	Dist. to Target (cm)	HV (V)	Time Res. (ns)
N1	$12.7\phi \times 5.08$	NE224	2.7	-2344	1.2
N2	$12.7\phi \times 12.7$	BC501A	2.6	-2385	1.4
N3	$12.7\phi \times 12.7$	BC501A	1.8	-1150	1.4
N4	$12.7\phi \times 12.7$	NE213	2.2	-1475	1.2
N5	$12.7\phi \times 12.7$	BC501A	1.8	-1180	1.5

Table 2.3: Dimensions and characteristics of neutron detectors. BC501A and NE213 are chemically equivalent. Distance to target measured from the front-face of detector to the outer vacuum jacket of target. Timing resolutions based on peaks in the E1-E5 short-range TDC (time-digital converter) time spectra.

The primary principle of operation of these detectors is based on neutron-proton elastic scattering in the liquid; the recoiling proton ionizes the material generating scintillation light, detected by a single PMT located at the far end. The neutron transfers all or part of its energy to the proton resulting in a "box" spectrum ex-

[3]During the November 1996 engineering run it was discovered that muonic x-rays from stops in the gold and silver were also useful in the energy calibration of the neutron detectors.

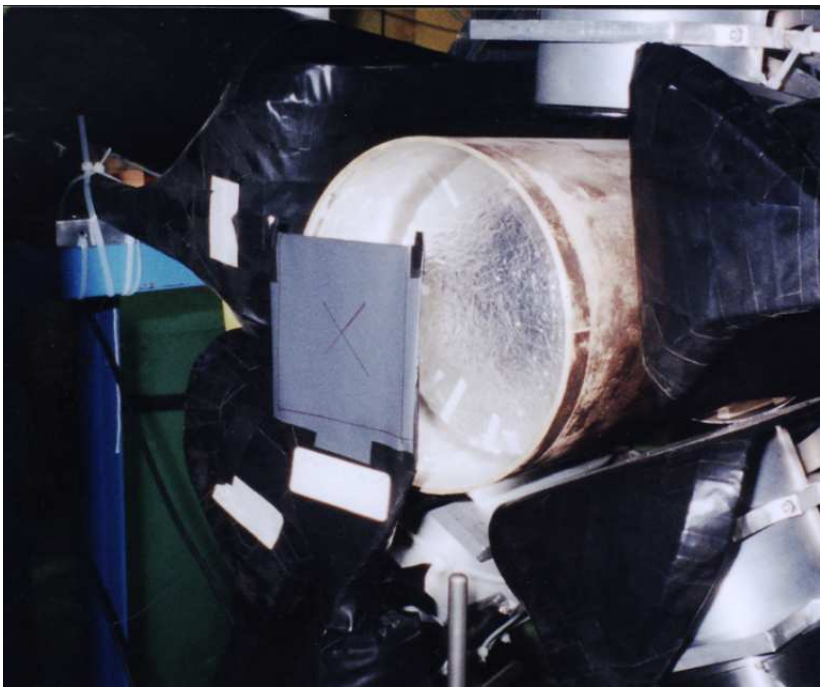

Figure 2.4: Photograph of target and detector setup. The beam-defining S2 can be seen in front of the target window. The wrapped light guides for E1, E2, E3, and E5 obscure the view of the their respective neutron detectors. Beam arrives from the left.

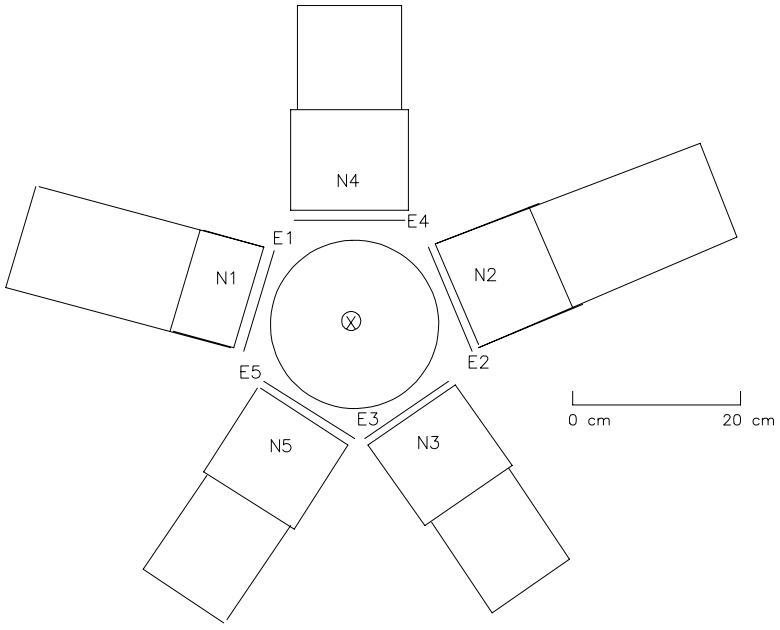

Figure 2.5: Sketch of relative locations and orientations of target, charged particle vetos, and neutron detectors. Only the active region of the charged particle vetos is shown (between the target and neutron counters). Beam direction is into the page.

tending from a maximum of the neutron's incident energy down to zero. The "box" is smeared out by a variety of effects—ionization statistics, electron multiplication statistics, and light collection variation—as seen in Figure 2.6. Photons interact in the liquid through the photoelectric, Compton, and pair production processes producing electrons which then emit scintillation light. The electrons and other charged particles produce scintillation light when interacting in the detector.

The overall decay-time—and thereby, pulse shape—of the emitted light varies, depending on the energy loss per path length (dE/dx) of the exciting radiation. Therefore, the light output (related to pulse area) from an incident neutron is not equal to that of a photon or electron of the same incident energy. This is important in the calibration of the detectors. One of the keys to this experiment is exploiting these pulse shape differences between recoil protons and electrons.

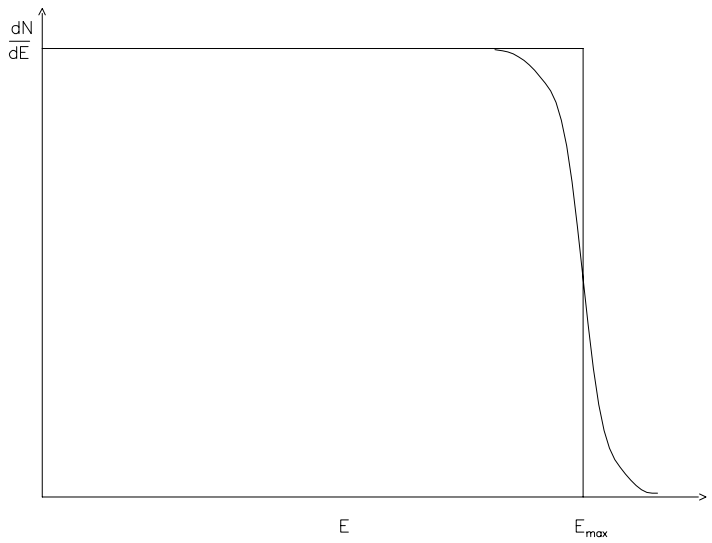

Figure 2.6: "Box" spectrum from neutron interactions in liquid scintillator. The smeared shape results from ionization statistics, electron multiplication statistics, and light collection variation. [41]

2.3.1 Neutron Detector Energy Calibration

The neutron detectors are calibrated for energy using three main methods: π^- capture neutrons, radioactive sources, and μ^- x-rays. Tuning the channel for a π^- beam produces the reaction $\pi^- + p \rightarrow \gamma + n$ which yields a prompt, monoenergetic 8.8 MeV neutron. Radioactive sources ^{60}Co and ^{241}Am/Be each produce observable Compton edges in the detectors. When muons stop in the gold and silver target walls, muonic x-rays are produced. These x-rays appear in the prompt (in coincidence with a μ^- stop) spectra of the neutron detectors. The 511 KeV positron peak and the 2.2 MeV γ-ray from thermal neutron capture on hydrogen can also be used as checks of the calibration. Details of the calibration procedures are found in Section 3.2.

2.3.2 Charged Particle Veto Counters

To enable the rejection of incident charged particles (primarily electrons from muon decay) a thin plastic scintillator was placed in front of the entrance-face of

each liquid detector. A preliminary charged particle veto was set in hardware and was then reapplied more precisely in software. Table 2.4 lists the dimensions of each veto counter.

Veto Counter	Dimensions (cm)	High Voltage (V)
E1	$20.3 \times 20.3 \times 0.32$	-1906
E2	$20.3 \times 20.3 \times 0.32$	-1730
E3	$20.3 \times 20.3 \times 0.32$	-1865
E4	$12.7\phi \times 0.16$	-2275
E5	$20.3 \times 20.3 \times 0.32$	-2450

Table 2.4: Veto counter dimensions.

2.4 Electronics

The electronics logic digitized the times, pulse heights, and output rates from the scintillators and detectors and selected events of interest—the trigger. The muon beam rate was on the order of 100 KHz, but the data acquisition system (DAQ) could only handle an event rate of about 1 KHz, at these data word lengths. Therefore, the electronics logic selected only candidate neutron events and a small, prescaled sample of gamma and electron events for calibration and other diagnostics. The following sections include schematics of the electronics used in the experiment. Figure 2.7 provides the key to the symbols and notations used in Figures 2.8, 2.10, 2.12, and 2.13.

2.4.1 Pulse Shape Discrimination

Neutrons and gammas were differentiated in the electronics with pulse shape discrimination (PSD). The principle of PSD is that scattered protons from incident neutrons in the liquid detectors have longer pulse tails than the electrons from photon interactions [42]. The primary PSD (PSD1) was accomplished using custom NIM modules from the University of Alberta [43]. The module was supplied with an

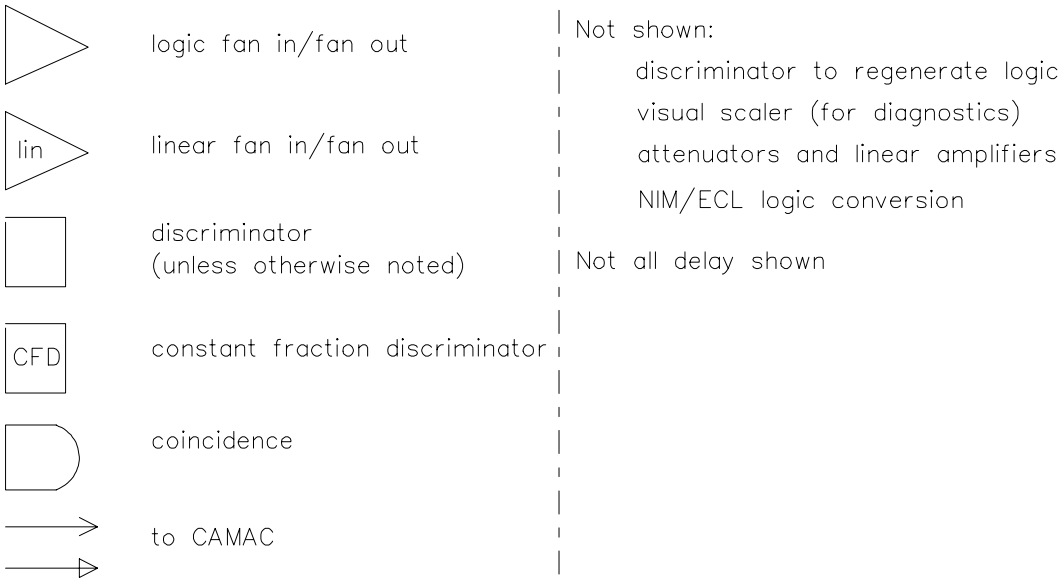

Figure 2.7: Key to logic schematics.

input trigger and the analog signal from the detector. The pulse was integrated over a short (52 ns) and long (420 ns) period. The difference between these integrations is the PSD signal output. The result of the long gate integration is proportional to the energy that the particle deposited in the detector and is the energy signal output. A two-dimensional histogram of the energy and PSD outputs was then used in software to discriminate between photons and neutrons. The PSD unit also produced two logic pulses indicating "neutron" or "gamma" based on levels which have been selected in the setup of the modules using radioactive sources. In order to avoid rejecting, in hardware, potential neutron events, the "neutron" selection criteria were made deliberately loose. Further PSD was then applied in software.

Since the discrimination of gammas and neutrons is crucial to the success of the experiment, a second method of PSD (PSD2) was developed and used for refining the PSD cuts in software and for added redundancy. This additional PSD used a ratio of the energy output from the Alberta PSD module to the output of an integration of only the "tail" of the neutron detector signal—again relying on the

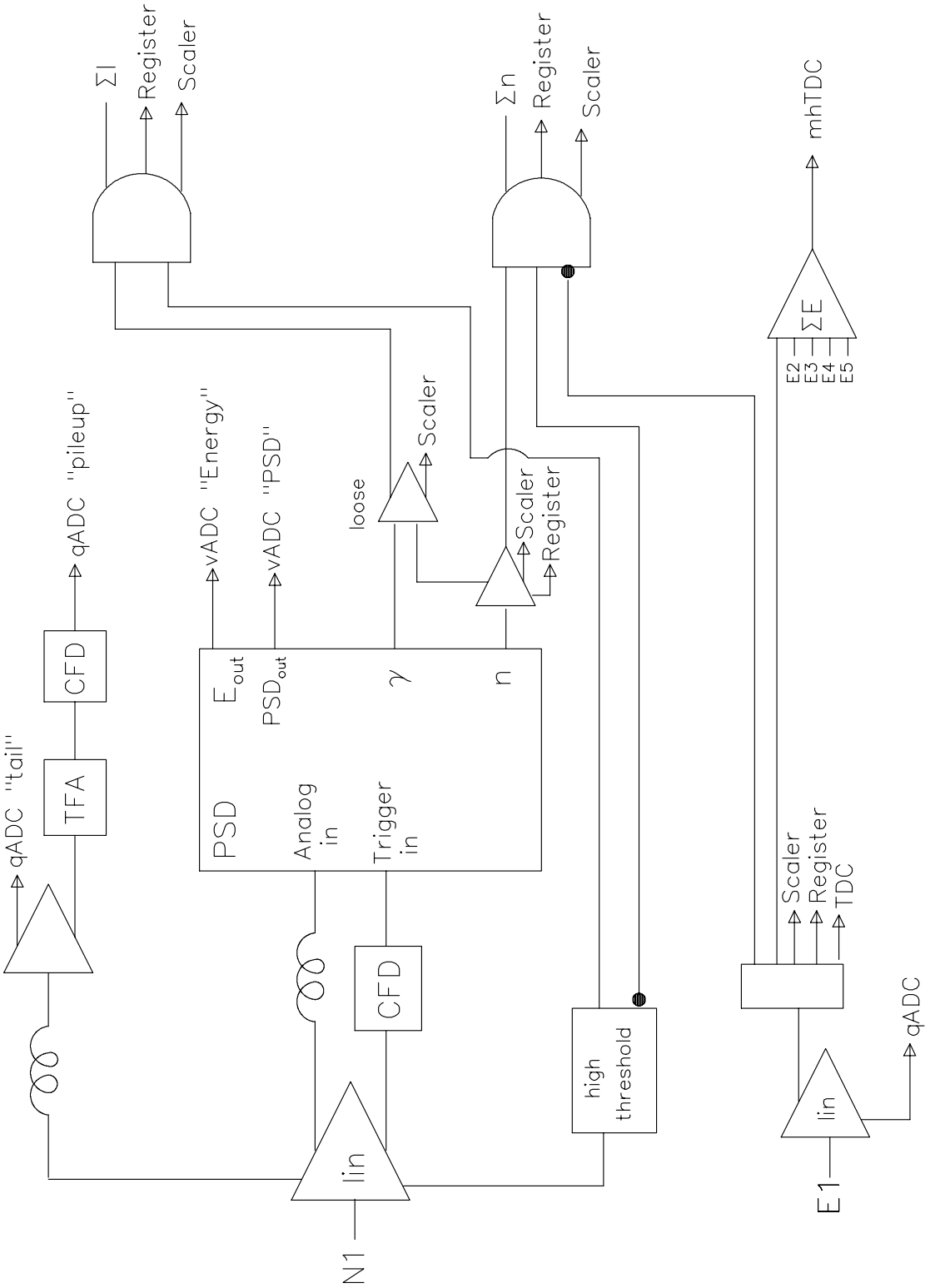

Figure 2.8: Schematic of neutron logic circuit.

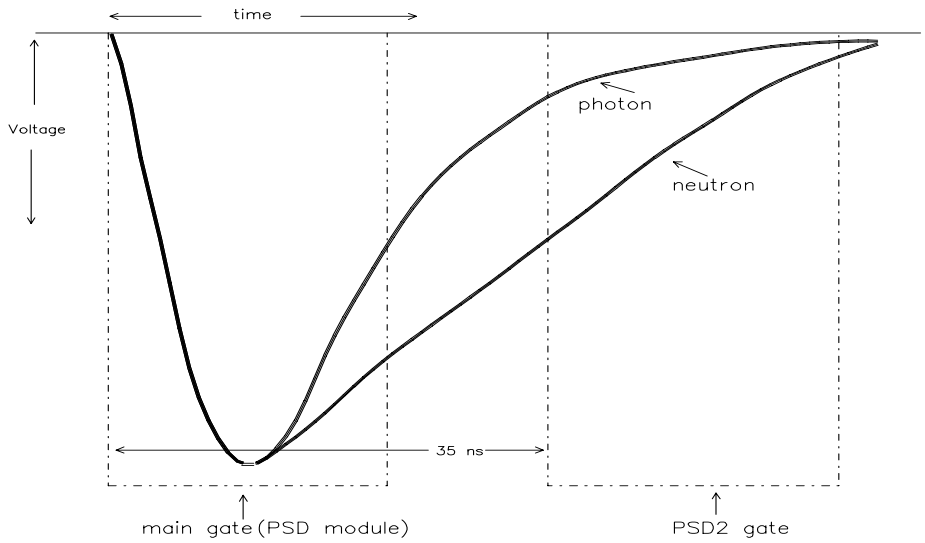

Figure 2.9: Sketch of PSD2 principle. The pulse shape differences between the photon- and neutron-induced events are evident. The later PSD2 gate samples the tail of the pulse. The main gate is supplied by the U. Alberta modules.

inherent pulse shape difference of an incident gamma or neutron in the detector. The "tail" signal was obtained using an ADC (analog-to-digital converter) module with its gate delayed by 35 ns, so that it only sampled the tail of the analog pulse. Figure 2.9 shows a sketch of a sample neutron- and photon-induced pulse along with the two gates used in the PSD2 technique. The logic diagram for N1, including the components for each PSD technique and charged particle veto, is shown in Figure 2.8. The logic for N2, N4, and N5 is identical. N3 could not be operated at the optimum high voltage, due to sparking. Therefore, a lower voltage was applied and the signal was then amplified and then attenuated in order to compensate for this lower operating voltage.

2.4.2 Trigger

For each detector, the neutron trigger requirement consisted of a "neutron" logic pulse from the PSD module which was in anti-coincidence with a signal from the charged particle veto counter. An overload veto condition also rejected signals

that resulted from an overly large hit in the detector, since these events were not of interest. The resulting neutron signals for each detector were timed together and "or"ed to produce the Σn trigger. Figure 2.10 shows the trigger logic diagram.

Since the "gamma" logic signal from the PSD module is of interest for calibration and other diagnostic purposes, this signal was used to create a second trigger. The "gamma" logic signal from the PSD module was "or"ed with the "neutron" logic pulse and the result was checked for anti-coincidence with the overload rejection. Therefore, the resulting signal is a sample of all events that satisfy either, the "gamma," "neutron," or even "electron" condition (since there was no rejection of events in the charged particle veto counter)—but do not appear as an overload in the detector. This signal is referred to as the "loose" trigger, and the result from each detector was "or"ed together to produce the Σl trigger. In this experiment there were many more of these events than neutron events, so to balance the effect on computer dead-time and the statistics needed for diagnostic purposes, only a sampling of events—prescaled typically by a factor of 2^7—was recorded.

The Σn and prescaled Σl signals were "or"ed and then checked for anti-coincidence with the computer inhibit to create the "event" logic signal. The computer inhibit signal was produced to stop any events from being sent to the computer while it was already busy with an event. After an event was received, a NIM driver module produced this inhibit signal. However, there was a delay in this response, so the event itself triggered a gate-generated pulse to fill the time before the driver reacted.

2.4.3 Multi-hit TDC and Beam Electronics

In a high duty-factor beam, the pileup of muons in the target will cause distortions in the time spectra. At an incident beam rate of 100kHz, the average time interval between muons is much shorter than both the decay lifetime of the muon and the lifetime of captured muons. For this experiment there were three potential

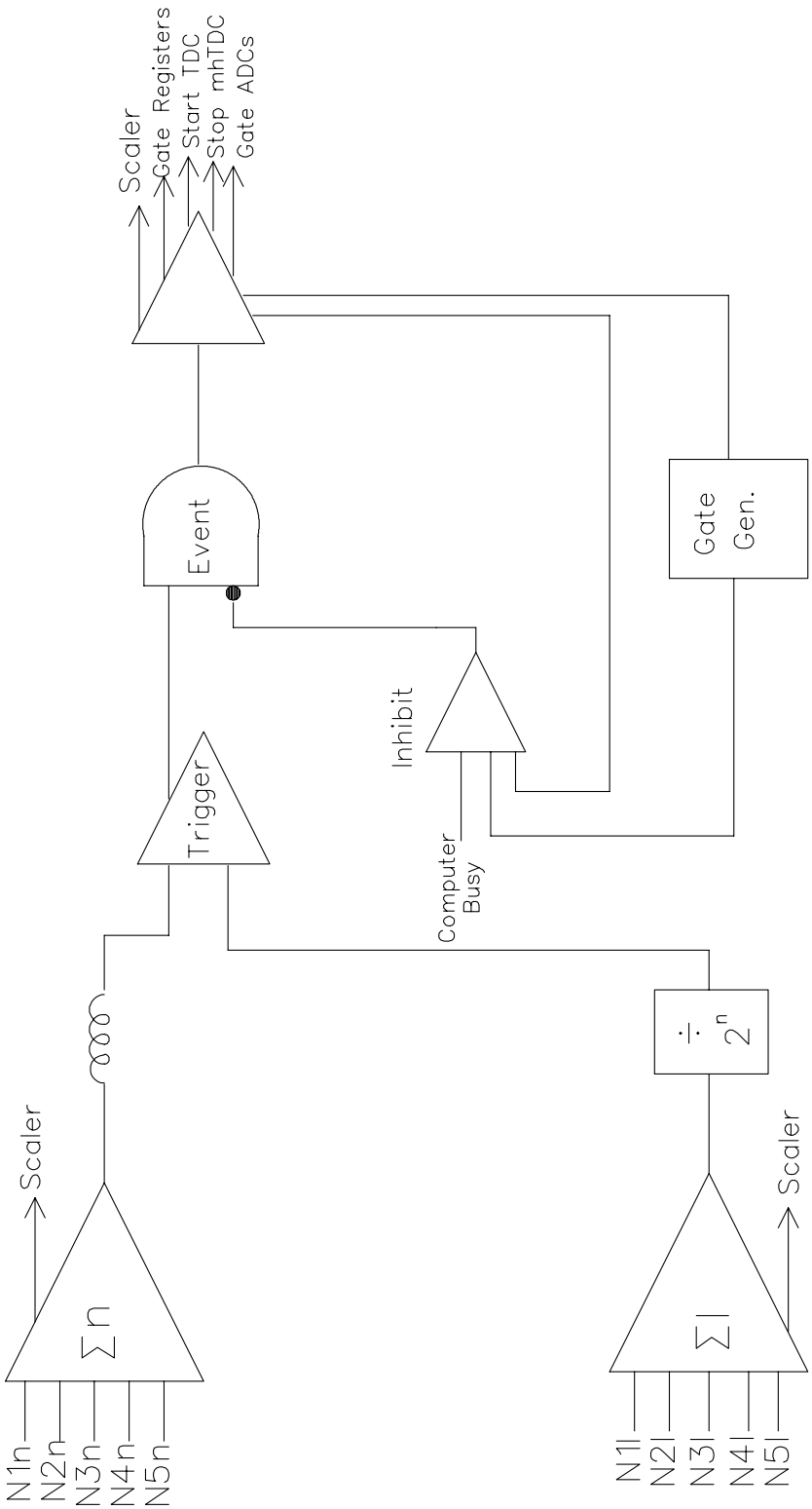

Figure 2.10: Schematic of trigger logic circuit.

ways of dealing with muon pileup:

1. The TRIUMF cyclotron can deliver a pulsed beam, as was used in the Saclay measurement. The instantaneous beam rate is high, but the time between beam bursts is long compared to capture times. However, the background events can then have a time dependency which cause distortions in the time spectra. Also, the other experiments running simultaneously would be displeased by the usage of a pulsed beam.

2. The incident beam rate can be turned down to deliver only one muon in a $10\tau_\mu$ time period. While this alleviates muon pileup, there is a crippling loss in statistics. With this low signal rate, the cosmic ray background becomes non-negligible. Also, since the primary beam is still operating at full current, the cyclotron-related background is still the same as with high rate beam.

3. The usage of multi-hit TDC (time-to-digital converter) electronics allows the usage of a high rate, full duty-factor beam. For a given trigger, the time histogram is updated several times, *i.e.* for each previous μ^- (as far back as, say, $10\tau_\mu$). The result is a time spectrum from the "correct" muon superimposed on a flat, uncorrelated background due to the other muons which have a random arrival time.

The third option was chosen for this experiment. Multi-hit electronics were not available at the time of the Saclay measurement, making this a novel feature of this experiment. The LeCroy 3377 multi-hit TDC (mhTDC) operates using a pipeline principle[4]. As seen in Figure 2.11, the mhTDC stored the time of each "start" event (*e.g.* a muon). When a "stop" occurred (*e.g.* a neutron trigger), the mhTDC

[4] A useful analogy is that of the official clock for a marathon. The clock starts at the beginning of the race but does not just stop when the first runner finishes—it continues to record finishers' times up to a certain cut-off time.

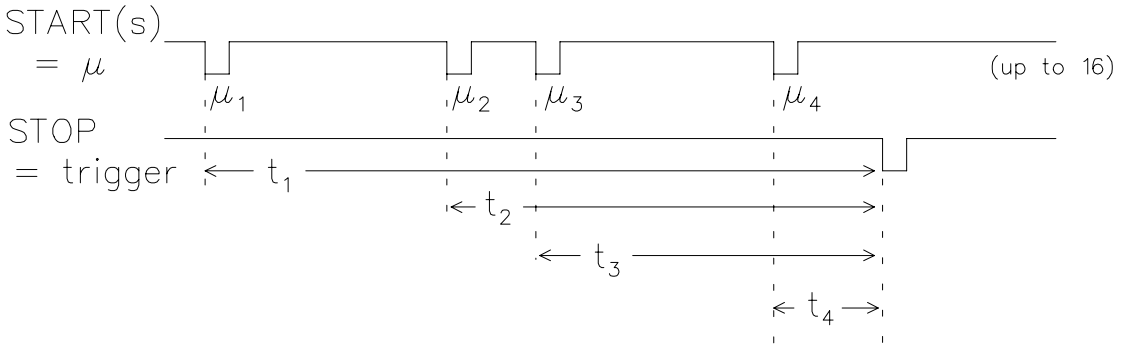

Figure 2.11: Multihit TDC principle. In this example, four STARTs (muons) are recorded. When the STOP (trigger) occurs, the module digitizes the time difference between each START and the Common STOP. The module will only record up to 16 hits in each channel.

digitized the time difference between the stop and each start—within the following limits: each input channel (there are 16 channels on the module) can accept up to 16 different hits with a range of 32 μs and with a time resolution[5] of 0.5 ns [44]. At the beam rates used in the present experiment, 16 hits rarely occur. Note that 32 μs corresponds to many muon lifetimes, so that all the physics of interest is within the range of the module.

An added advantage to using the mhTDC was the ability to reject muon pileup, if desired. Multiple muon rejection was applied in software, to select those neutrons where only one muon arrived during the $12\tau_\mu$ time window. Here the flat background is removed, at the cost of reduced statistics for the signal. No special low-rate beam data had to be taken.

For this experiment, 4 of the 16 input channels were used. A valid trigger event created a common stop for the module. The first channel recorded a coincidence between beam counters S1 and S2 (S1·S2), which constitute the muon stop condition. The second channel recorded events with a hit in S1 but not S2 (S1·$\overline{\text{S2}}$). This signal was used in the analysis for background studies of muons that entered the

[5]The differential non-linearity of the time bins is poor, but with coarse rebinning the effect becomes negligible.

experimental area and likely missed the target, presumably, interacting with some material other than $l\mathrm{H}_2$. The third channel recorded events from an "or" of the time signals from each charged particle veto counter (ΣE). This signal was used for diagnostics of the muon decay electronics. Finally, a duty-factor monitor signal (explained in Section 2.4.4) was recorded.

For prompt event studies, short-range, high-resolution single-hit TDCs were also used to separately digitize the S1·S2, S1·$\overline{\mathrm{S2}}$, and individual E signals. Figure 2.12 shows the beam logic. The $\mathrm{S1_e}$ signal was the result of sending the S1 signal into a discriminator with a low threshold voltage. Both muons and electrons incident on this scintillator will "fire" this discriminator. The $\mathrm{S1}_\mu$ and $\mathrm{S2}_\mu$ signals resulted from the S1 and S2 signals, respectively, being sent through discriminators with high thresholds. Only the higher-energy muons will fire these discriminators. The $\mathrm{S2_{hi}}$ signal looked for events where the muon stopped and captured in the scintillator, thereby resulting in a large pulse. These events were dangerous because they fire S2, thus indicating a muon stop in the target, but actually produced neutrons from muon capture in carbon, a dangerous background.

2.4.4 Miscellaneous electronics

Capacitive Probe

The TRIUMF cyclotron produces short beam pulses with 99 % duty-factor. The small microstructure was monitored via the induced signal from a capacitive probe placed in the primary proton beam. This signal gave the timing of the trigger event with respect to the beam pulses which arrived every 43 ns. For this experiment, the signal was prescaled by a factor of eight. The resulting signal was used to check that the so-called prompt events were truly prompt with respect to the beam. Any time-dependencies in the cyclotron-related background was also monitored. Figure 2.13 shows the logic diagram for this signal.

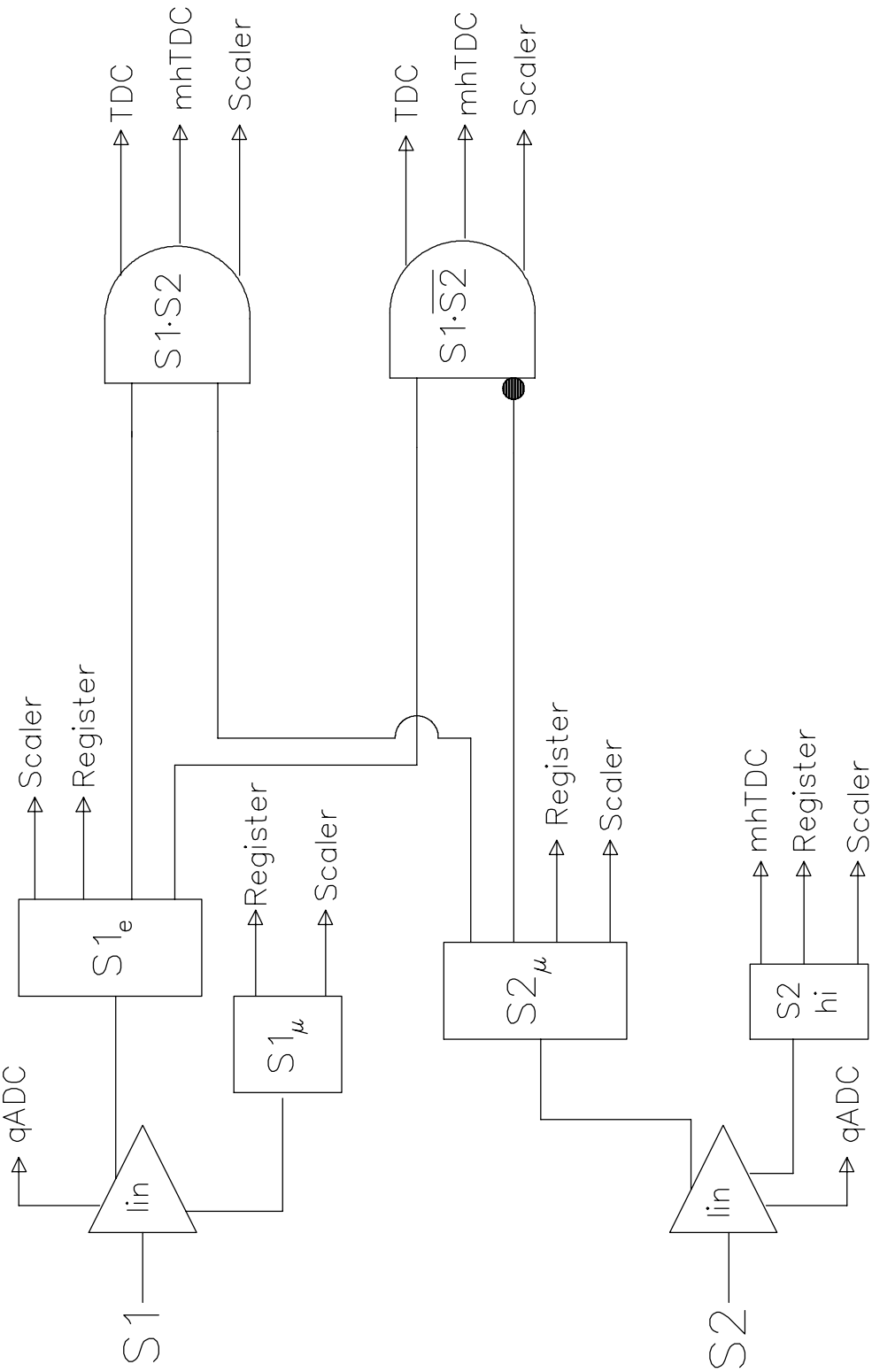

Figure 2.12: Schematic of beam logic circuit.

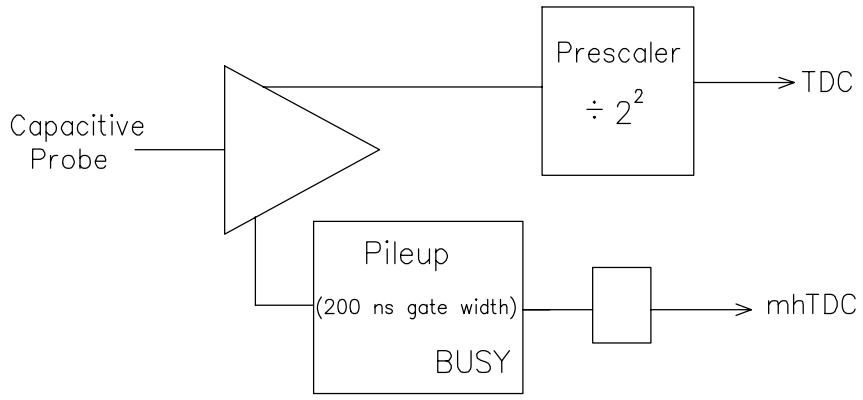

Figure 2.13: Logic circuit schematic for capacitive probe signal and duty factor check.

Duty-Factor

The TRIUMF beam is not truly CW, but has a typical duty-factor of 97%; the beam is off for 30 μs out of each millisecond. This can lead to distortions in the mhTDC time spectra. Consider a neutron that is detected just *after* the beam comes back after one of the 30 μs quiet periods. This neutron will not have a normal flat distribution of muons in its pre-history. The effect becomes much more apparent at low duty-factor. Therefore, a circuit was added to the electronics to "flag" events within 32 μs of a "beam off" period. The capacitive probe signal was sent into a Pileup Gate which generates a "busy" gate as long as the beam pulses occur within 200 ns (time lapse set on module) of each other[6]. During a beam-off period, the busy gate would end. When the beam returned, the busy gate returned. This signal was sent into the mhTDC. If the busy gate had just started, the mhTDC detected a leading edge and registered a hit in that channel—meaning that there was recently a "hole" in the beam. If a trigger had occured within 32 μs of this beam off period, the event could be rejected in software. Figure 2.13 shows the logic diagram for this circuit.

[6]Presumably, the pulses occur every 43 ns, so this gate will be on continuously during the beam-on period

Photon Pileup

If two gamma pulses fired a liquid scintillator at approximately the same time, the PSD could have mistakenly identified the resulting broad "pileup" pulse of the two as being the pulse shape characteristic of a single neutron. To prevent these fake neutron events from distorting the time spectra, a pileup rejection circuit was devised [45]. The analog pulse from the neutron detector was sent to a Timing Filter Amplifier (TFA), which differentiated the signal. The output of the TFA was sent to a discriminator and then into an ADC (gate=600 ns). If the signal from the detector was just a single pulse, then the ADC recorded only the area of a single discriminator logic output. Any events with two (or more) photon pileups would trigger the discriminator twice (or more) and the ADC would have recorded the area of two (or more) pulses. These events could then be rejected in software. The pileup circuit electronics are shown in Figure 2.8.

Clock

A 10 kHz clock was created using a pulser and provided a reference for the scaler rates of the beam and triggers.

2.5 Data Acquisition- MIDAS

The data acquisition system consisted of a HYTEC 1331 PC-CAMAC interface and a PC Linux box running Maximum Integrated Data Acquisition System (MIDAS) [46]. MIDAS is a C-based system utilizing a central database and a network of modular components grouped in a single C library. It has been developed primarily by Stefan Ritt at the Paul Scherrer Institute (Switzerland) and Pierre-Andre Amaudruz at TRIUMF (Canada) between 1993 and 2001 .

The actual data acquisition from the hardware was moderated by the "front-end" code which controls the PC-CAMAC interface. The data were logged in buffers

Beam	*Rate* (s^{-1})	*comments*	
$S1_e$	145 K	all beam particles through S1	
$S1_\mu$	136 K	muons through S1; 94 % muons in beam	
S1·S2	121 K	89 % beam hits S2	
Signal		*(per $S1_\mu$)*	
ΣE	68 K	56 %	
Σl	28 K	23 %	anything that fires CFD for n-counters
Σl·$\overline{\text{OVL}}$	15 K	12%	loose; doesn't fire overload
Σn	16 K	13 %	based on PSD only
Σn·$\overline{\text{E}}$ · $\overline{\text{OVL}}$	680	0.6 %	neutron PSD; not charged; not overload
Σl·$\overline{\text{OVL}}$·prescale	115	prescale= 2^7	
Triggers	789		
Events	567	livetime= 72 %	

Table 2.5: Rates for typical high-rate run from November data. Livetime for this run is 72 %. Neutron candidates account for 85 % of all "Events," while the remaining 15 % result from "loose" trigger events.

controlled by the online database. The buffers could then be accessed by several clients, remotely or locally, via the MIDAS server. The data logging client received events from the buffer manager and wrote them onto 8mm magnetic tapes for later analysis. Typical livetimes during the experiment were $\sim$ 70 %. Table 2.5 shows the rates for a typical high-rate run from the November run.

2.5.1 Online Analysis

The MIDAS analyzer client received events from the buffer manager for online analysis. The experiment-specific C-based analyzer used HBOOK routines for histogramming and PAW(++) [47] for histogram display. A sample of the data was analyzed immediately from PAW without stopping the run.

2.5.2 "Off"-line Analysis

The same analyzer was then used to read events from a file for off-line analysis. Again, PAW(++) was used, with additional analysis from Physica [48].

2.6 Engineering Run

An "engineering" test run took place during November and December 1996. The main objectives of the test run included:

- tests of the pulse-shape discrimination electronics, trigger logic, multi-hit TDC, and pileup rejection electronics.
- tests of in-beam calibration procedures for the liquid scintillation detectors.
- optimization of target-detector geometry, beam counter geometry, and studies of collimation of the muon beam and beam-tuning.
- investigation of various backgrounds.

The detector setup for the engineering run consisted of three liquid scintillation counters, three beam counters, and plastic collimators of varying diameters. The TRIUMF standard data acquisition VDACS [49] system was used along with DISPLAY for online analysis. Further analysis was performed with the NOVA [50] data analysis software package.

The findings from the engineering run resulted in the choice to eliminate beam collimation and the use of the duty-factor electronics described in Section 2.4.4. It was also determined that the differential non-linearity of the multi-hit TDC did not affect the data at the coarse binning factors used in the analysis. The engineering run also confirmed the high levels of backgrounds present in the experiment. However, analysis of these data was able to produce evidence of the 5.2 MeV neutrons and their resulting time spectrum.

2.7 Summary

The ortho-para transition was measured at TRIUMF using the beam, target, detectors, and electronics described in this chapter. The following chapter describes

the analysis of the data taken during two production runs in 1999.

CHAPTER 3

Analysis

3.1 Overview

The data analysis is presented in this chapter. Over 80 gigabytes of data were analyzed, including μ^- production data runs along with μ^+, π^-, radioactive source, empty target, cosmic ray, and cyclotron background runs. A total of 265.7×10^8 muons were stopped in hydrogen, over the course of 24 days. 405,700 neutrons within the OMC energy window were detected.

3.2 Energy Calibration

3.2.1 Radioactive Sources

Radioactive sources were used during select runs for the purposes of setting up the electronic PSD modules and providing initial, online energy calibrations for the neutron detectors. During the installation of the detectors and electronics, sources which emit photons and/or neutrons of known energies—in the range of interest for this particular measurement—were placed on or near the liquid scintillators. Table 3.1 lists the sources used and the energies of their primary emitted photons and neutrons. Using these sources, the settings for the hardware PSD thresholds, used for identifying either "neutron" or "gamma" events, were fixed. The data from these source runs were determined to be inadequate in the offline energy calibrations of the detectors since the data were not taken during the optimal, production running, however they were useful for online data analysis during the experiment.

Source	TRIUMF Tag No.	E_γ (MeV)	E_n (MeV)
^{60}Co	R#124	1.333, 1.173	—
^{241}Am/Be	R#133	4.43	4–8

Table 3.1: Radioactive source characteristics.

3.2.2 Gammas

Each of the following photon calibration points were measured during λ_{op} production runs in order to continually monitor the energy stability of each detector: muonic x-rays, positron annihilation photons, and thermal $n + p \rightarrow d + \gamma$.

Muonic X-rays

A copious source of photons, in prompt coincidence with an arriving muon, are the muonic x-rays from μ^- stops in the Au and Ag target walls. These were clearly identified in the ADC energy spectra after applying the following cuts:

- "prompt"—short-range, single hit TDC; event in coincidence with beam particle (S1·S2).
- "neutral"—ADC; no signal in charged particle veto counters.
- "not charged"—TDC; no signal in charged particle veto counters.
- "gamma"—ADC; based on cuts in the 2-D Energy vs. PSD spectra (PSD1).

Figure 3.1 shows the typical resulting x-ray spectrum from each detector. Even with the γ events pre-scaled in the trigger by a typical factor of 2^6 or 2^7, there were adequate statistics in the γ-ray spectra from a one hour run to fit the Compton edges and determine the energy calibration to within a few percent.

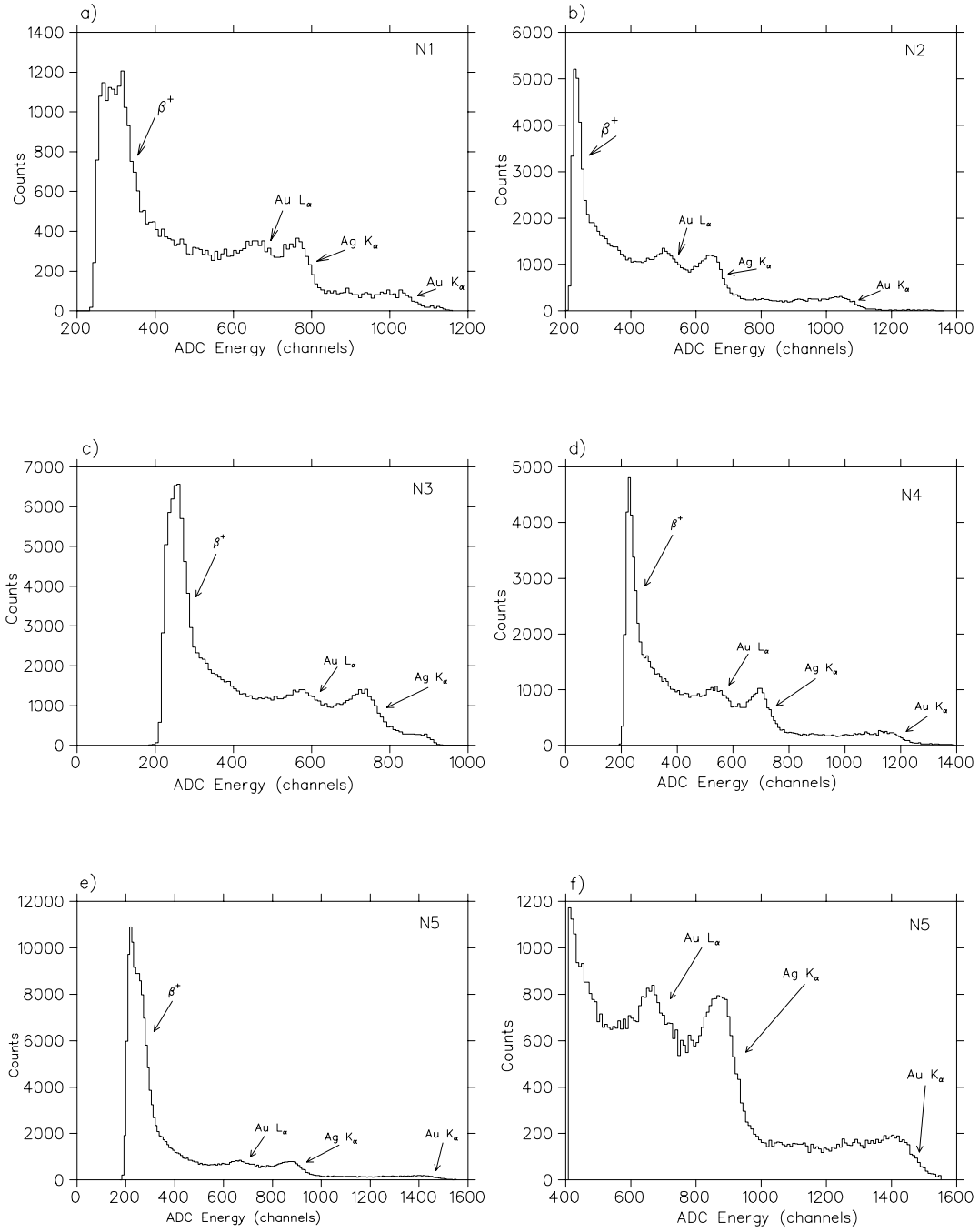

Figure 3.1: Muonic x-rays in neutron detectors from a typical run. The positron and γ-ray peaks are clearly seen in each detector. Spectrum f) shows an expansion of the γ-ray edges in N5.

Positron Peak

A 511 KeV peak from $e^+ + e^- \rightarrow \gamma + \gamma$ annihilation events is clearly seen in the γ-ray spectra for each detector. No additional special cuts are needed, and this peak shows up clearly in the spectra in Figure 3.1.

$n + p \rightarrow d + \gamma$

A delayed photon event can occur when a thermal neutron interacts with a proton in the target and forms a deuteron and a 2.2 MeV photon. This peak was identified after applying the same conditions as for x-rays except instead with a "non-prompt" requirement (event *not* in coincidence with beam particle (S1·S2)). Figure 3.2 shows the delayed gamma spectrum for each detector; the deuteron capture γ-ray Compton edge is visible in each case.

3.2.3 Calibration Curves

The ADC channel value of the Compton edge for each photon peak in the above spectra was determined for each detector. The energy calibration was then determined for each detector by plotting the five[1] photon energy points (in channels) versus their Compton energies (in MeV), and performing a least-squares fit to a straight line. Acceptable fits were obtained (see Figure 3.3) for each detector. Table 3.2 lists the calibration values.

Detector	slope (channels/MeV)	intercept (channels)
N1	167 ± 9	302 ± 20
N2	162 ± 3	195 ± 10
N3	175 ± 6	231 ± 15
N4	182 ± 5	187 ± 14
N5	226 ± 1	222 ± 4

Table 3.2: Photon energy calibrations for each neutron detector, based on Compton edges.

[1] only four in N3.

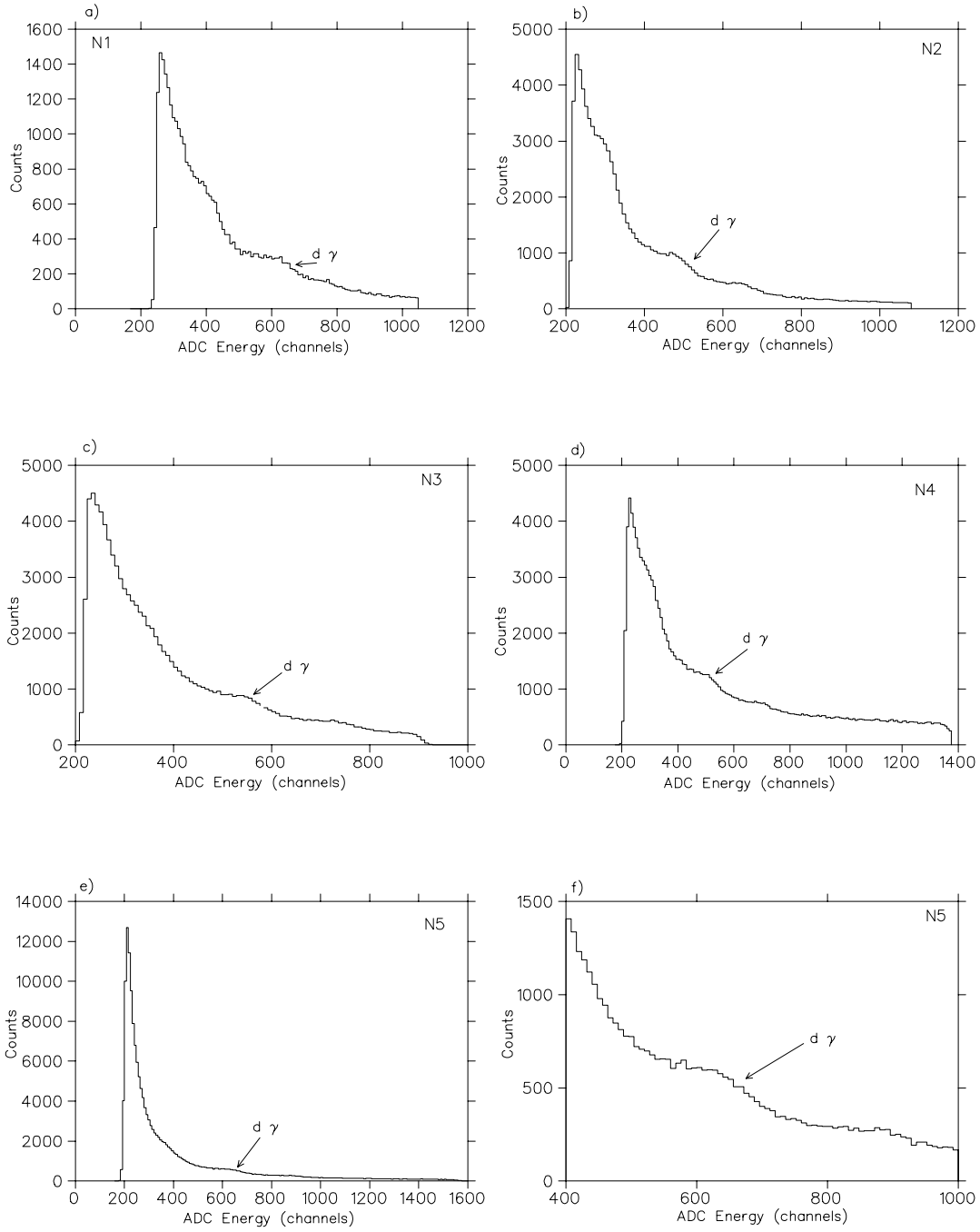

Figure 3.2: Delayed photon events in neutron detectors. The 2.2 MeV $n + p \rightarrow d + \gamma$ thermal neutron gamma-ray is seen in each detector. Spectrum f) shows an expansion of the spectrum from N5.

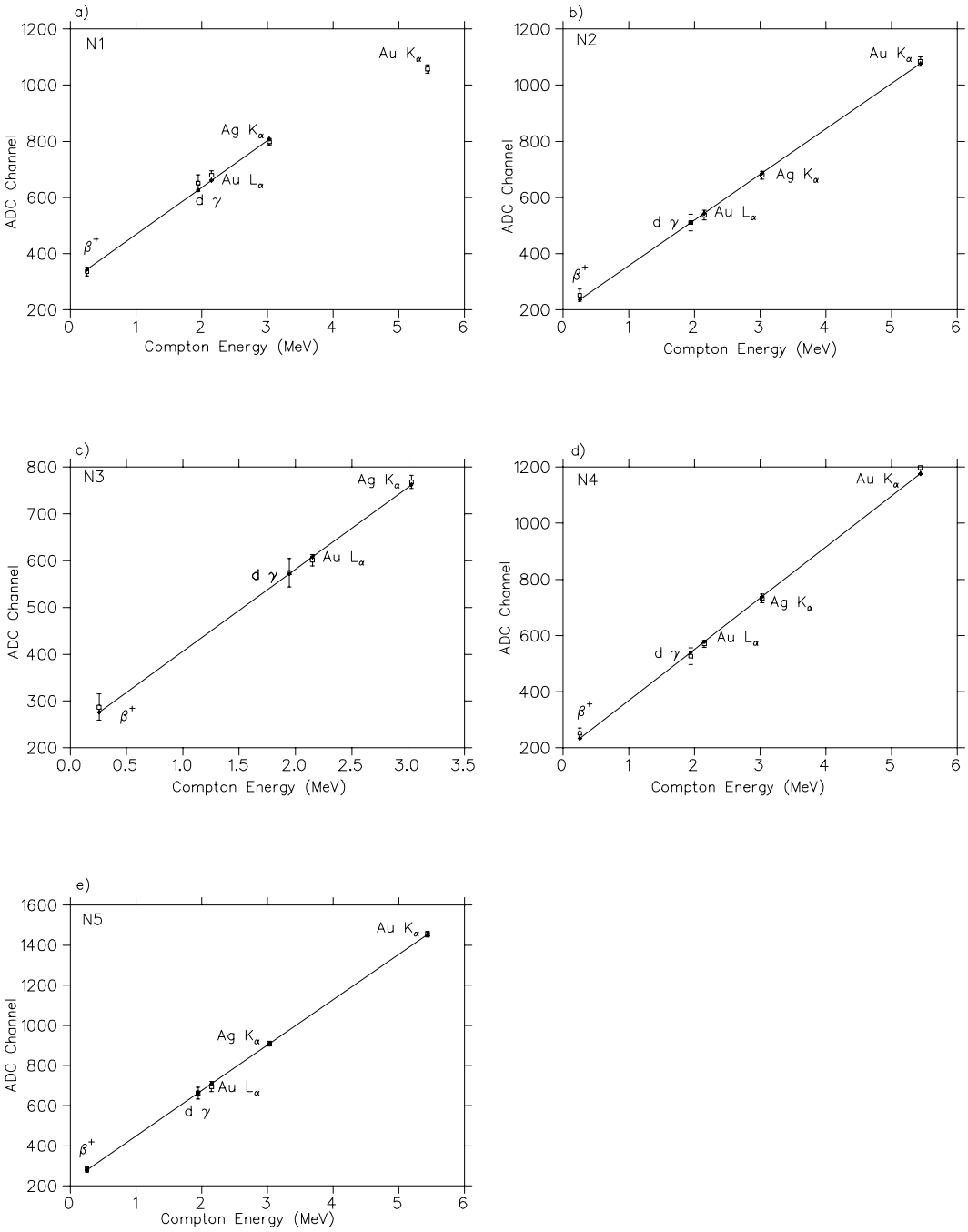

Figure 3.3: Energy calibration curves for γ-rays for each neutron detector.

3.2.4 Pion-induced Neutrons

Pion beam[2] data were taken in the early data-taking runs. The intention was to use the mono-energetic 8.8 MeV neutrons from the $\pi^- + p \rightarrow \gamma + n$ reaction as an energy calibration point for the neutron detectors. However, because of the time-dependent drift in the calibrations, these data were taken too early in the data taking process (several days before μ^- 'production' running) to prove useful in the analysis of the muon capture signal data. Instead, they were used to test the conversion between γ-ray calibration and neutron energy in the liquid scintillators.

Since the pion beam was higher in momentum than the muon beam, a degrader[3] was placed after the first beam counter in order to ensure that the pions stopped in the target's center. In order to produce a clean sample of neutrons, the following cuts were made on the data:

- Hardware trigger indicated a neutron event in detectors (from bit register).
- Good neutron PSD, based on the E *vs.* PSD spectra. (see Section 3.3.1 for details on the neutron PSD).
- Charged particles vetoed according to the following conditions:
  1. no signal in the individual veto counters (using the high-resolution single-hit TDC) at the time of the trigger.
  2. no signal in the Σ E multi-hit TDC channel at the time of the trigger.
  3. no significant ADC value from any E counter.
- A "prompt" cut which required the S1 and S2 single-hit TDCs to fire in an early window of the prompt beam peak—this is therefore a time-of-flight cut

[2]Beam composition: 40 % π^-, 40 % μ^-, 20 % e^-.

[3]During the two pion-runs analyzed, plywood degraders of varying thicknesses were placed between S1 and S2 to ensure that the pions stopped in the hydrogen. The thicknesses were 1.0 cm, 1.6 cm, and 2.9 cm.

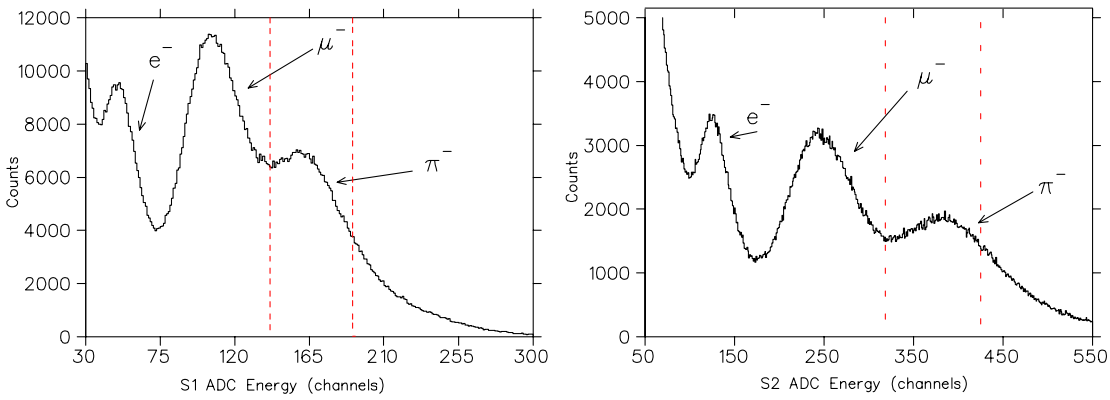

Figure 3.4: Beam counter ADC spectra obtained during a pion run; the cuts used to select π^--induced events are indicated by the dashed lines.

which rejected slower, low-energy neutrons.

- S1 and S2 ADC values within narrow windows around the pion pulse height in the S1 and S2 ADC spectra—this rejected muon and electron-induced events. Figure 3.4 shows the ADC spectra for both S1 and S2 during a pion run, with the cut windows indicated.

None of these cuts should affect the location of the 8.8 MeV neutrons in the ADC spectra, only the signal/background ratio. Figure 3.5 shows the resulting neutron spectra for each detector after these cuts are applied. Also shown for comparison are the neutron energy spectra for non-prompt events (normalized at the high-energy end). The "edge" of the box spectrum of the 8.8 MeV neutron is clearly visible around channels 800-1000 in the spectra for all five detectors. Note that the neutron spectral shapes are not the "box" expected from ideal (n,p) elastic scattering. The shapes are consistent with realistic monoenergetic neutron spectra taking into account finite detector resolution and the non-linearity of light output *vs.* recoil proton energy [41].

Since the energy calibrations were observed to drift over long periods of time, a high-statistics muon run from just before the pion runs was analyzed to obtain the appropriate γ-ray calibration data. In order to test the γ-ray calibration technique

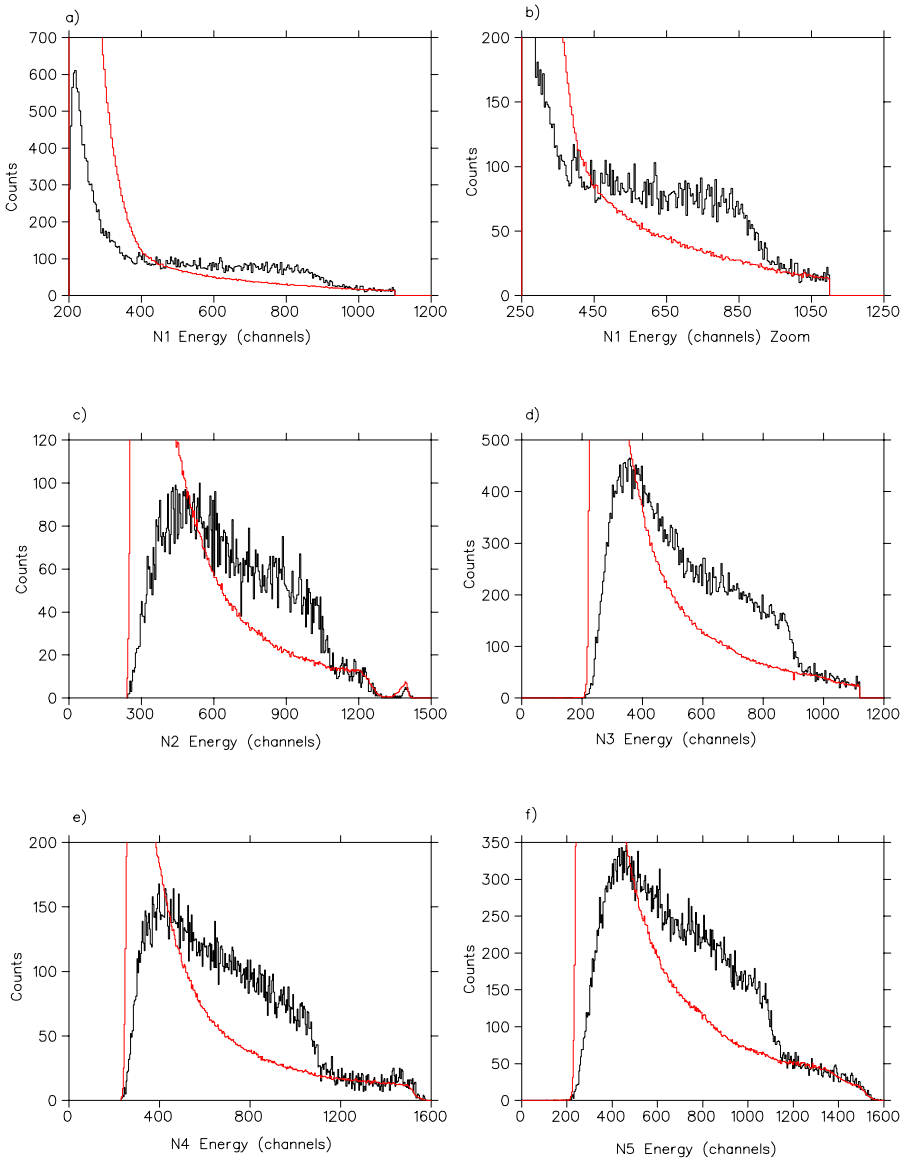

Figure 3.5: Neutron spectrum from $\pi^- + p \rightarrow \gamma + n$ for each detector. The 8.8 MeV neutron produces the box-like spectrum shown in the heavy curve. The smoother, red curves are the neutron energy spectra for non-prompt events (normalized at the high-energy end). Spectrum b) shows an expansion of the N1 spectrum, to suppress the low-energy peak.

with this 8.8 MeV neutron, the different light output in the scintillators for an electron (from a Compton-scattering photon) and for a heavily ionizing proton (from (n,p) scattering) was taken into account. The following light response function relates the energy of the scattered electron, E_e, to the energy of the scattered proton, E_p, for equal light output:

$$E_e = a_1 E_p - a_2(1 - \exp(-a_3 E_p^{a_4})) \ [51], \tag{3.1}$$

where a_i are empirical coefficients which depend on the scintillating material. Table 3.3 lists these coefficients for both NE213 and NE224 for this relation, where E_p and E_e are both given in MeV. For an 8.8 MeV proton, the equivalent light output is that from a 4.76 MeV electron in N1 (NE224) and a 4.91 MeV electron in detectors N2-N5 (NE213). A 5.2 MeV proton corresponds to a 2.35 MeV electron in N1 and a 2.38 MeV electron in N2-N5. The results from the comparison of the edges in Figure 3.5 to the photon energy calibration data are listed in Table 3.4.

	NE213	NE224
a_1	0.83	1.0
a_2 (MeV)	2.82	8.2
a_3 $(\text{MeV})^{-1}$	0.25	0.1
a_4	0.93	0.88

Table 3.3: Light response function coefficients for NE213 and NE224 [51].

This analysis shows that the energy calibrations obtained with the γ-rays are reasonable and can be used to predict the detector's response to neutrons. N3's values could be suspicious since 8.8 MeV appears close to the region where the E *vs.* PSD curves over and the gammas/electrons/neutrons become difficult to distinguish (see Figure 3.10. The ratio between the data and the predicted value averages to 0.98 ± 0.05. Thus, the calibrations predict the location of the 8.8 MeV neutron "edge" in the data to within about 5%. Even though these data cannot be directly

detector	8.8 MeV from pion data (channels)	8.8 MeV prediction using γ-ray data (channels)	$\frac{\text{data}}{\text{prediction}}$
N1	895 ± 10	871	1.03
N2	1050 ± 10	1018	1.03
N3	895 ± 10	985	0.91
N4	1082 ± 10	1128	0.96
N5	1103 ± 10	1142	0.97

Table 3.4: Position of upper edge (in ADC channels) of 8.8 MeV neutron "box" for each detector, as measured in $\pi^- p$ run, compared to predicted channel number based on photon calibration data (see text), and their ratio.

compared to later muon runs and the 5.2 MeV neutrons, the technique of using γ-rays for cross-calibration was proven effective, and this should provide confidence in the identification of the 5.2 MeV μ^- capture neutron (see Section 3.3.3).

3.3 Neutron Identification

A major challenge in this experiment was to identify and suppress the various backgrounds that can produce either real neutrons not from muon capture on the proton or fake neutrons in the detectors, and thereby distort the measured neutron time distribution. In this section, the elimination of fake neutrons in the data is discussed. However, the cuts described below will not be sufficient to eliminate all the fake neutrons in the data. Section 3.3.4 will discuss the use of ancillary measurements (*e.g.* the use of a μ^+ beam) and time spectrum analysis to determine the residual fake neutron background and also to determine the background of real neutrons not arising from muon capture on the proton.

3.3.1 Pulse Shape Discrimination

The difference in the characteristic pulse-shape between recoil protons and electrons in the BC501A scintillator allows efficient n/γ discrimination. The efficiency

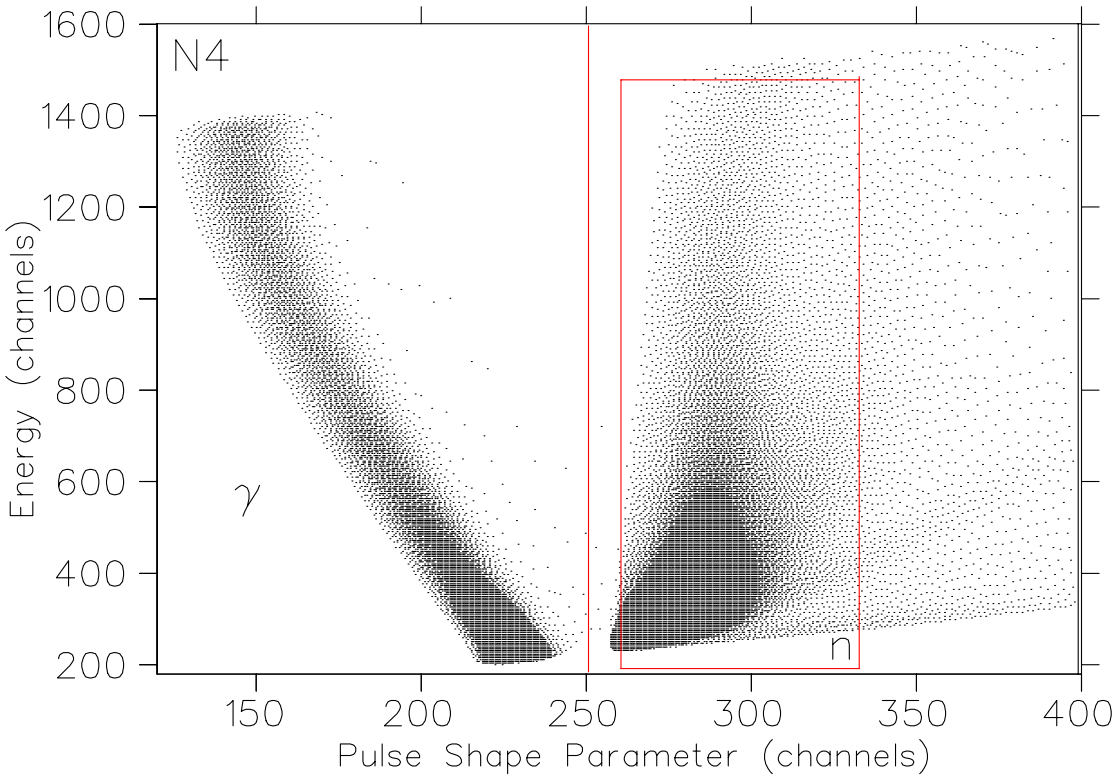

Figure 3.6: This 2-D spectrum shows the primary PSD (PSD1) for N4. Photons populate the band on the left-hand side, while neutrons appear on the right. The box indicates the cut used to select good neutron events. The cut for photon events is shown by the line at PSD channel 250.

of this discrimination is energy-dependent, improving as the proton energy increases. The neutron energy from OMC on hydrogen is 5.2 MeV, so the recoil proton energy spectrum is a "box" shape extending from 0 to 5.2 MeV.

As discussed in Section 2.4.1, there are two methods of pulse shape discrimination (PSD). The primary software PSD (PSD1) utilizes the "Energy" and "PSD" analog outputs of the University of Alberta modules. A two-dimensional Energy *vs.* PSD spectrum results in a "V"-like shape with photon and neutron events occupying separate sides of the "V." A sample E *vs.* PSD spectrum for N4 is shown in Figure 3.6. Photon events populate the band on the left-hand side, while neutrons are on the right. A box shows the cut used to select "good" neutron events. Photons are identified as events with a PSD value less than 250.

The secondary PSD (PSD2) uses a 2-D scatter-plot of the Alberta PSD "Energy" output *vs.* the integration of the "tail" of the neutron detector signal. A sample spectrum for N5 is shown in Figure 3.7. The photons are seen in the top band, while the neutrons occupy the lower. The lines indicate the cut used to select a "clean" sample of neutron events. This spectrum has been corrected for "60 Hz noise" in the "tail" electronics by subtracting the ADC value of a detector that did not produce the trigger.

Figure 3.8 shows the effect of utilizing both PSD methods. The solid curve indicates a projection, on an axis perpendicular to the PSD2 bands' slopes, of "good" neutron events selected by PSD1. For reference, photon PSD1 events are indicated by the dashed curve. The lines show the PSD2 neutron cut. The PSD2 cut essentially insures a "cleaner" sample of neutron events by eliminating events that pass the PSD1 neutron cut but lie within the region of photon events.

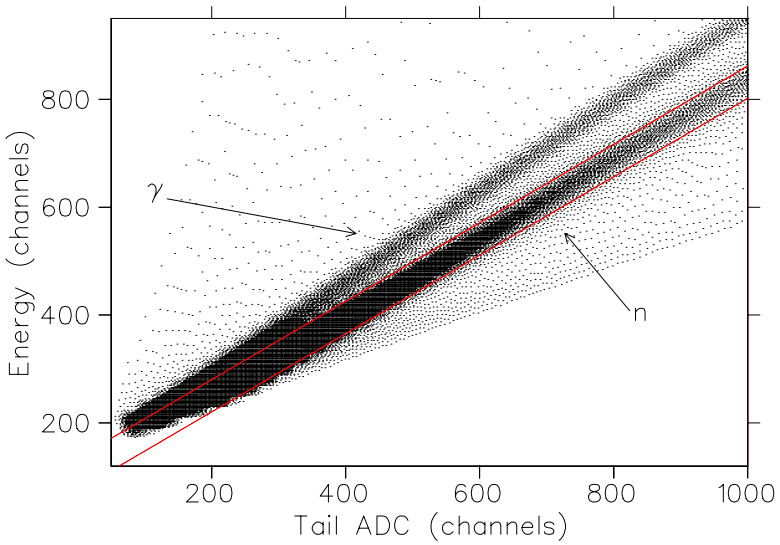

Figure 3.7: This 2-D spectrum shows the secondary PSD (PSD2) for N5. The top band consists of photons, while neutrons occupy the lower band. The lines indicate the cut used to select a "clean" sample of neutron events.

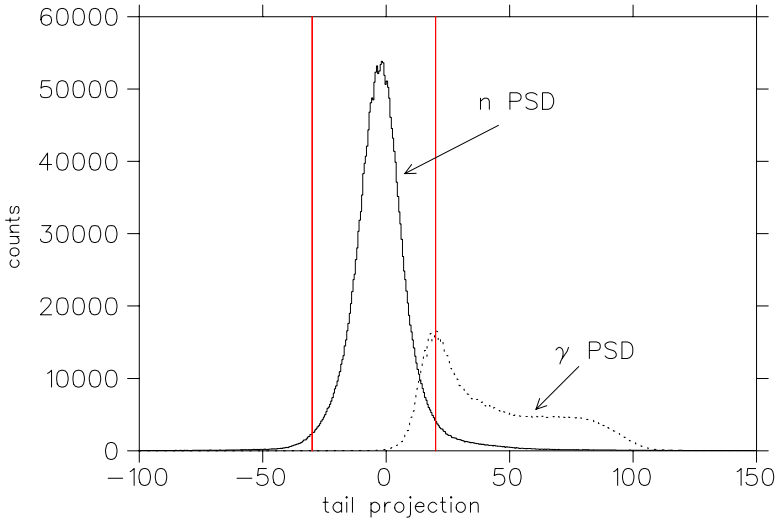

Figure 3.8: Spectrum of projection of "good" neutron events selected by PSD1 (solid curve) and photon PSD1 events (dashed curve). The lines indicate the limits of the neutron PSD2 cut. This figure signifies the importance of using both PSD methods to obtain a clean sample of neutron events.

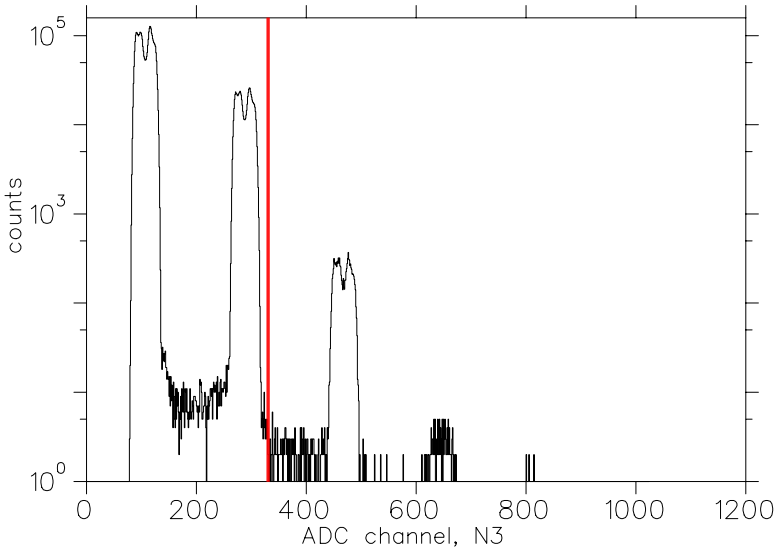

Figure 3.9: ADC spectrum from pileup circuit for N3. Only events where the ADC value is less than 330 (noted by the red line) are accepted by the pileup cut. In this spectrum, there are peaks indicating two, three, and even four pileup pulses (although the three and four pileup events are increasingly rare).

3.3.2 Misidentified Neutron Triggers

The first step in identifying neutrons resulting from muon capture on the proton is to make cuts to eliminate the neutron triggers resulting from fake neutrons.

Photons

Misidentified neutron triggers can arise due to a pileup of two photons that fire a detector in near coincidence and are identified by the hardware PSD as a neutron. Section 2.4.4 describes a circuit designed to identify such events. Figure 3.9 shows a typical pileup spectrum for N3. "Neutron" events with more than one peak (after the pedestal) are rejected. These events are also cut by the additional use of PSD2. Section 3.3.4 will discuss the use of μ^+ beam data to characterize the effect of pileup events on the neutron time spectrum.

Charged Particles

Protons from muon capture on the target walls, (n,p) reactions, electrons from muon decay, positrons from photon conversion, or even scattered beam muons or electrons are all charged particles that could hit the neutron detectors. The liquid scintillators respond to any ionizing particle, but most charged particles are rejected in hardware by the trigger requirement that there be no signal in the charged particle veto counters at the time of the event. However, as a safeguard, additional software cuts are made on the E counter ADC and TDC spectra. In the case of charged particles entering the detectors from the side, strict software pulse shape discrimination largely eliminates these events.

3.3.3 Energy Spectra of OMC Neutrons

After rejecting these fake neutron events, the energy spectra for all candidate neutron events were analyzed for evidence of the 5.2 MeV OMC neutrons. After applying the cuts described below, the energy window for the final time spectrum of the OMC neutrons is selected based on the resulting spectra, in addition to the x-ray/γ-ray calibrations.

A charged veto cut was applied, based on the Σ E signal from the MHTDC, eliminating any events where there was a signal in any E counter. There are two cuts that eliminate any prompt events (which are likely to be x-ray induced). The first cut rejects events with a signal in the $S1 \cdot S2$ short-range TDCs. The second prompt cut rejects events where there was any significant pulse height (*i.e.* even an electron pulse height) in the beam counter ADCs at the event time. A pileup cut is also applied to select events where no gamma-gamma pileup occurred in the detector, as shown in Figure 3.9.

A clean sample of neutron events is needed in order to make a clear selection of the OMC neutron energy window. To produce this clean sample, tight cuts (as

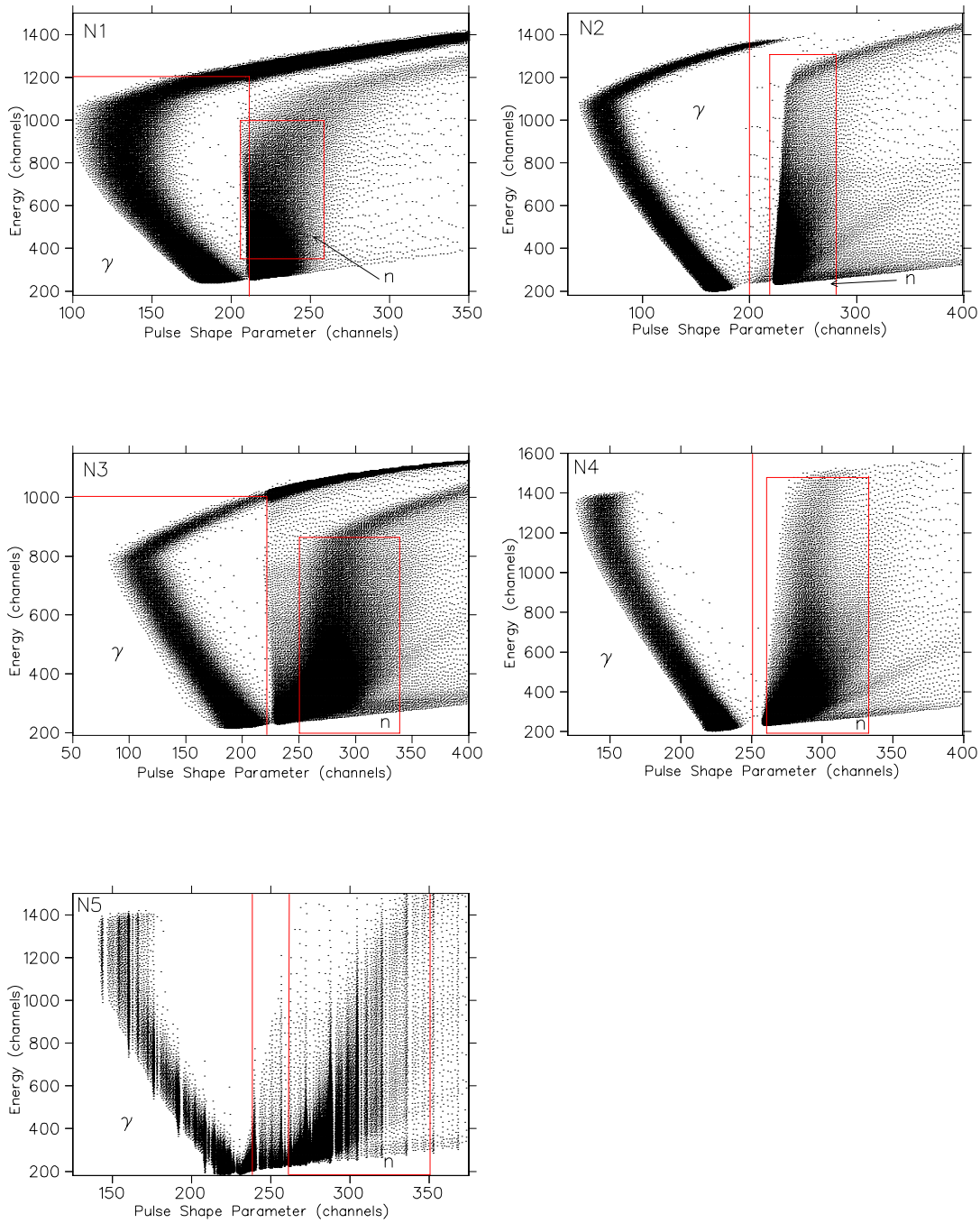

Figure 3.10: PSD1 2-D spectra for each detector. Neutron and photon cuts are indicated on each spectra. The linear fan-ins for N1, N2, and N3 saturate at high energies. The majority of these saturation events are rejected in the cuts. The spectrum for N5 appears "streaked" because a bit within the ADC was "stuck." This does not affect the data after coarse rebinning. (These spectra are shown here with fine bins to clearly illustrate the PSD technique.)

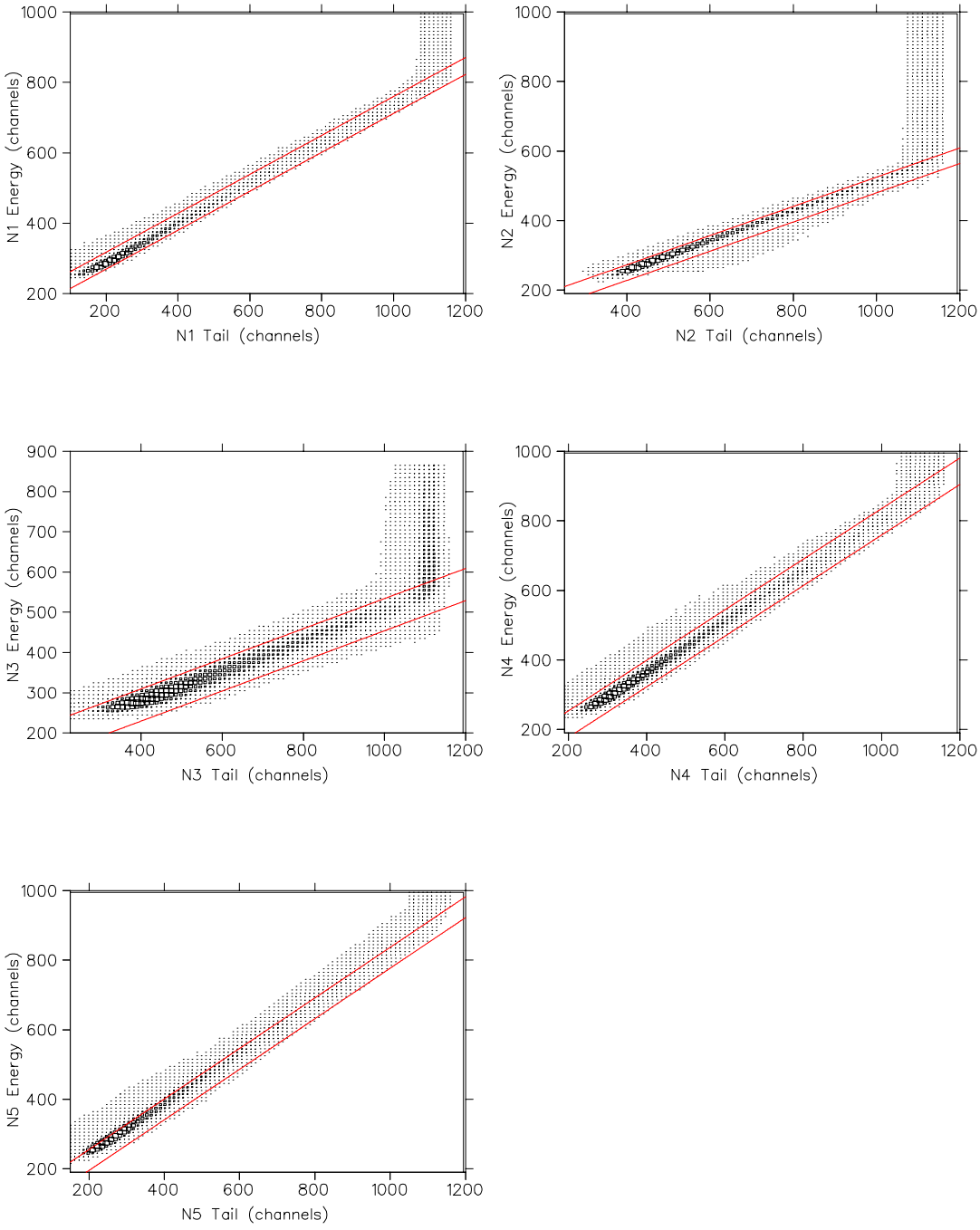

Figure 3.11: PSD2 2-D spectra of events that pass the PSD1 neutron cut for each detector. The neutron band is further "cleaned up" by the PSD2 neutron cuts indicated by the lines. Events where the Tail ADC has saturated (*i.e.* in the "bend" above Tail channel 1100) are also accepted.

described in Section 3.3.1) are applied to both 2-D spectra for each detector (see Figures 3.10 and 3.11). Events where the Tail ADC has saturated (*i.e.* in the "bend" above Tail channel 1100) are also accepted, since they are outside the OMC energy window.

In order to eliminate neutron events from stops in the Au and Ag target walls, a 'blank' timing cut is applied. This cut rejects events within 400 ns of the prompt time in either the S1·S2 or S1·$\overline{\text{S2}}$ spectra. Further details and effects of this cut are discussed in Section 3.3.4. While the blank cut results in a reduction in signal events, eliminating the large number of neutrons from Au/Ag capture reduces the error from a large flat background in the time spectrum, and also allows us to see the 5.2 MeV neutrons in the energy spectra.

After applying these cuts, the OMC neutron energy window is determined by comparing energy spectra during two beam timing conditions. The first condition looks at events with at least one S1·S2 muon within 1.5 hydrogen lifetimes (from 400 ns to 3.3 μs) of the prompt time. The second condition only looks at events for which there were no S1·S2 muons in the first 3.3 μs. The first condition produces an energy spectrum with both signal and background events. The second produces a spectrum with primarily background events. Since the backgrounds are largely time *independent*, and therefore the same in each time window, the two spectra can be subtracted (after normalizing at high energy) to produce a spectrum containing mainly signal events. The neutron energy windows for each detector were determined from these spectra. Figure 3.12 shows this process and the results for each detector. The 5.2 MeV neutrons are clearly seen in these spectra. Figure 3.13 shows this process for N5 with data from the μ^+ beam. There are no capture neutrons in these spectra since μ^+s do not capture.

Figure 3.14 shows the projection of PSD1 events in the chosen OMC energy window along the PSD axis for each detector. The separation between neutron and

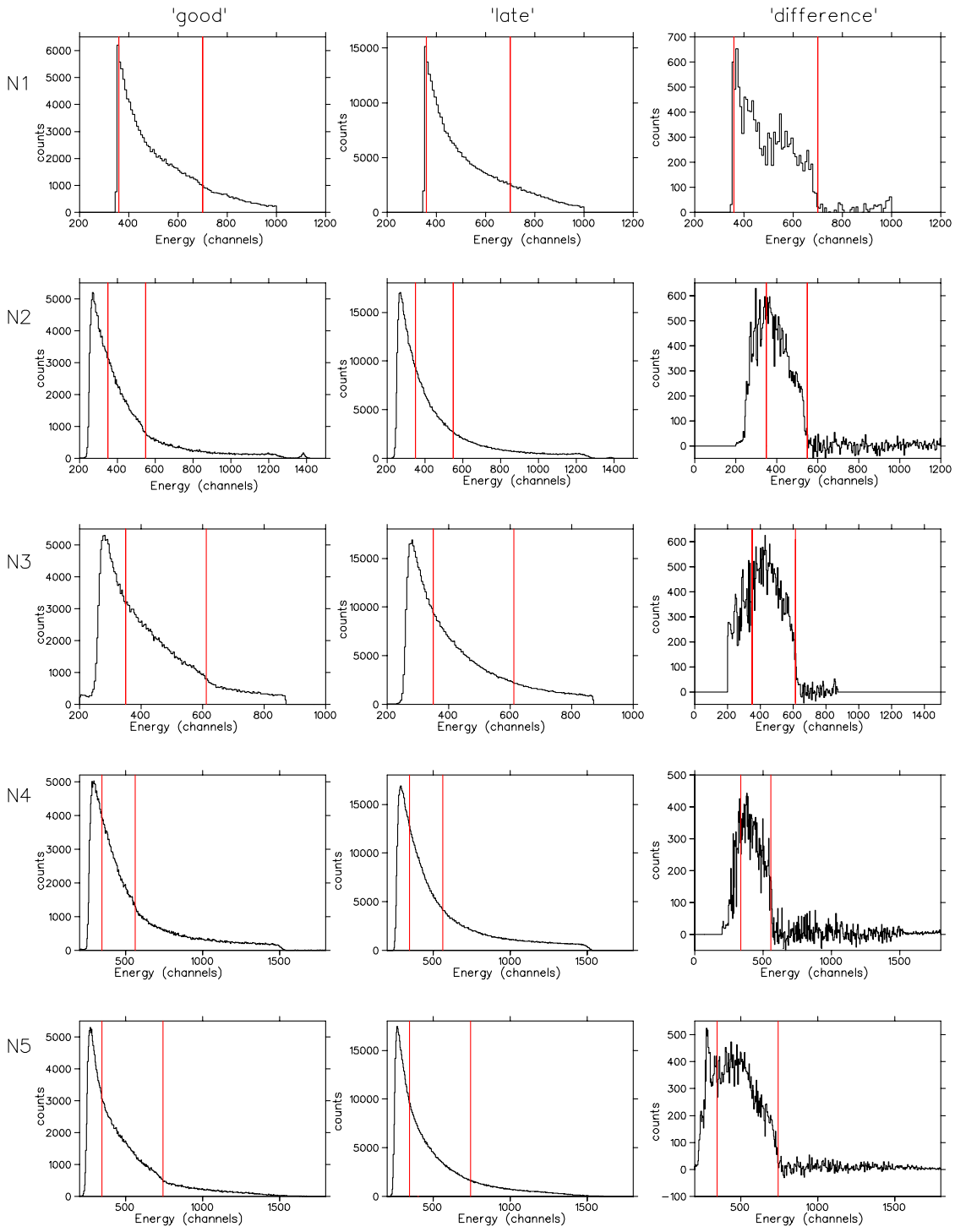

Figure 3.12: OMC energy window selection process for each detector. The first column shows the neutron energy spectra for events with at least one S1·S2 muon within 1.5 hydrogen lifetimes (3.3 μs) of the prompt time. The middle column shows the energy spectrum for neutron events where there were no S1·S2 muons in the first 3.3 μs. The difference between these two spectra (OMC neutrons) is shown in the third column. The energy window (indicated by the lines) for each detector is determined from these difference spectra.

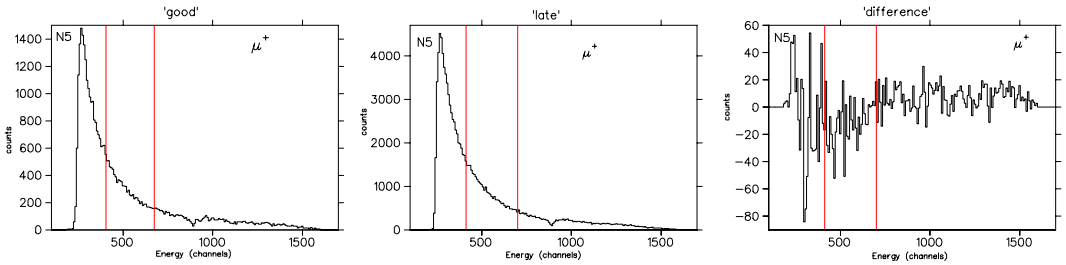

Figure 3.13: N5 neutron energy spectra for μ^+ data showing the same process used to determine the OMC energy window with μ^- data. As expected since there is no μ^+ capture, no OMC neutrons appear. This process gives similar results for all five detectors.

photon events is clearly seen, showing that the n/γ discrimination at these energies is adequate. Thus, it was determined that the 5.2 MeV neutrons are visible in the data in each detector. The time distribution of the events in these energy windows will be used to determine λ_{op}. However, the backgrounds within these energy cuts are still large and are discussed below.

3.3.4 "Real" Neutron Backgrounds

The remaining events have satisfied the criteria identifying them as neutrons, but not all of these neutrons result from muon capture on hydrogen. As seen in the previous section, selecting the energy window for the OMC neutrons does not result in a background-free spectrum. Therefore, the sources of these neutron backgrounds need to be understood, along with their effect on the neutron time spectrum. Also, these backgrounds need to be either reduced via cuts on the time spectrum or included as terms in the functional fit to the time spectrum. These sources of background neutrons include cosmic rays, cyclotron-related neutrons, remaining $\gamma\gamma$ pileup, photo neutrons[4], μ^- stops in Au and Ag target walls, μ^- stops in carbon, and μ^- stops in deuterium and high-Z contamination in target. A number of these backgrounds and their effects are determined by analyzing the time spectrum of the

[4] Photo-neutrons result from (γ, n) reactions where a photon with sufficient energy is absorbed by a nucleus, allowing the emission of a free neutron [41].

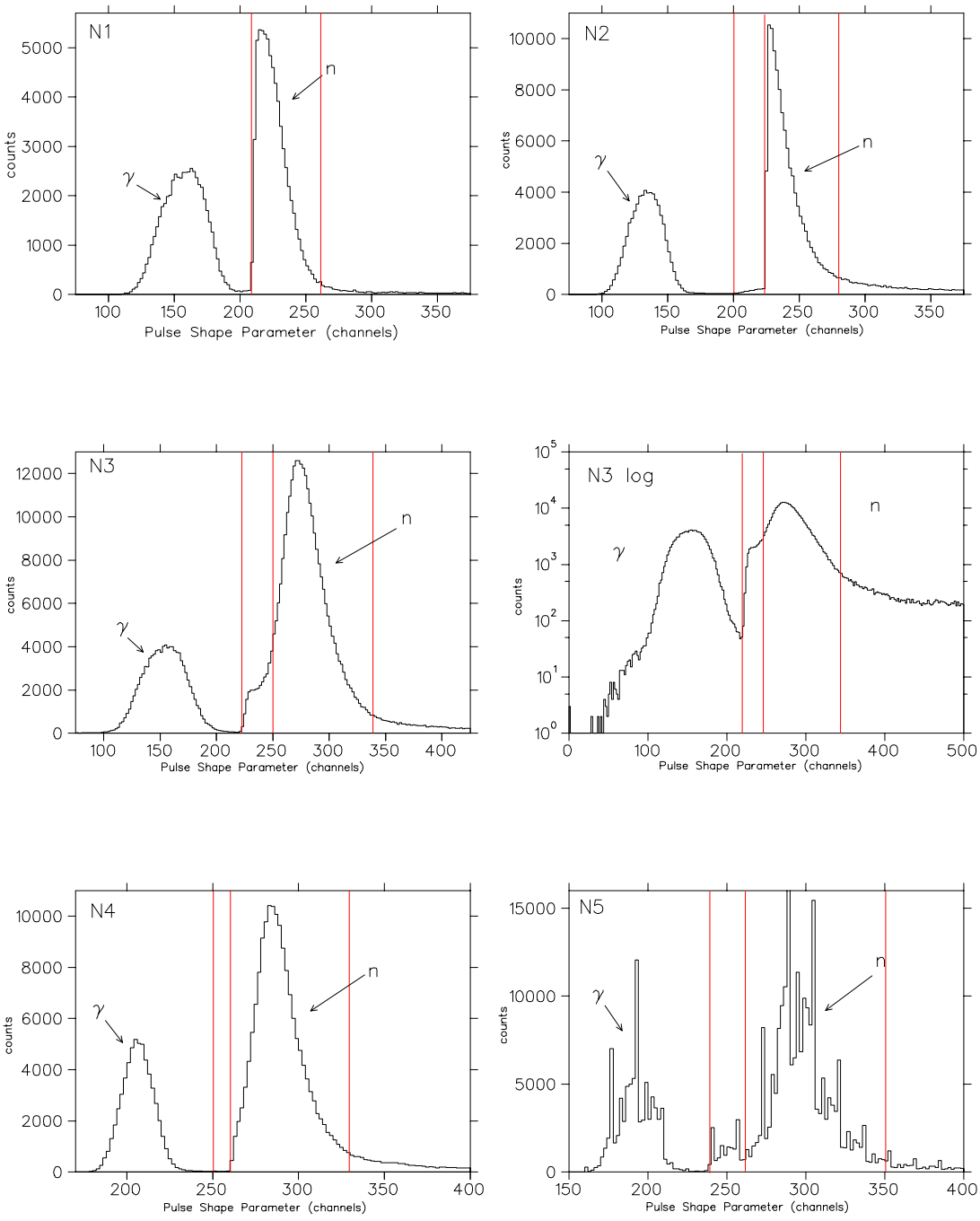

Figure 3.14: Projection of PSD1 events in the chosen OMC energy window along the pulse shape axis for each detector. Neutron and photon cuts are indicated by the lines. The separation between neutron and photon events is clearly seen. (The odd shape in N5 is due to a stuck ADC bit.)

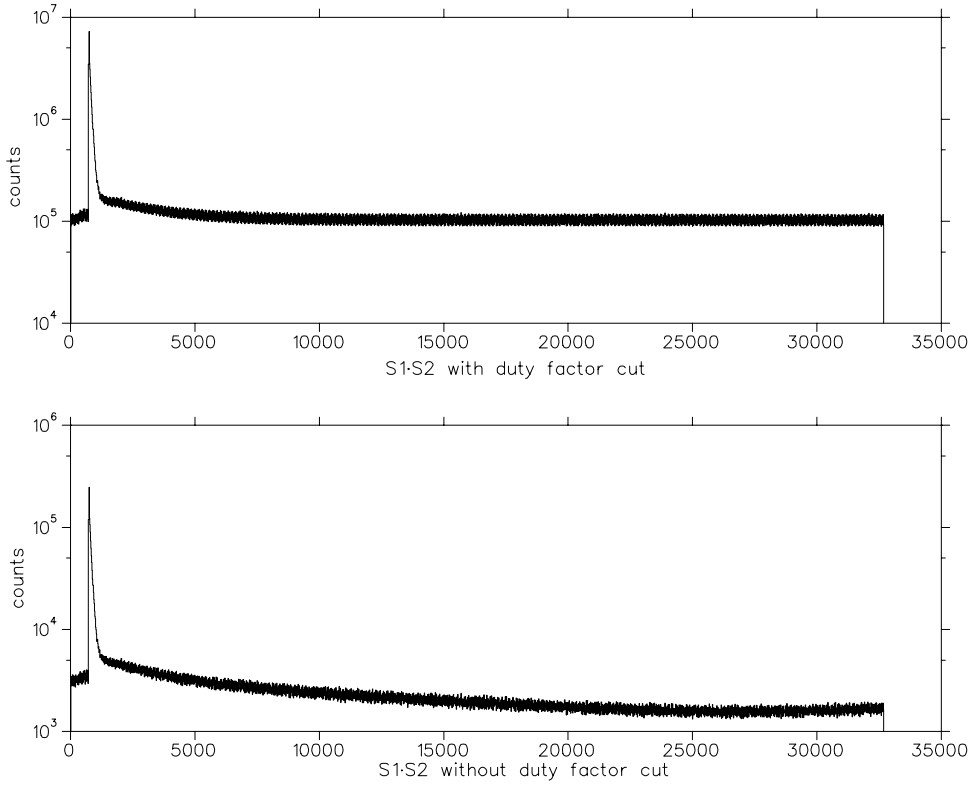

Figure 3.15: S1·S2 time spectrum (top) for all data satisfying the full duty-factor cut. S1·S2 time spectrum (bottom) for events which fail the duty-factor cut. The result is a distorted flat background at long times.

neutron events. Unless otherwise noted, the fitting expression used in the analysis of these backgrounds is

$$y = Ae^{-t/\tau} + c \tag{3.2}$$

where A is the amplitude of the exponential, τ is the lifetime of the component, and c is a constant. Each of the time spectra shown include cuts to eliminate distortions due to reductions in the beam duty-factor and muon multiplicity higher than the mhTDC can accept. The mhTDC can only digitize 16 hits per channel for each trigger. If more muons arrive within this time window, then the extra hits are lost, and the time spectrum is distorted. However, this problem can be solved by rejecting events with > 15 hits, thereby ensuring that all hits are recorded. Only $\sim 0.1\,\%$ of the statistics are lost due to this requirement.

As for the distortion resulting from reductions in the beam duty-factor, Section 2.4.4 describes a circuit used to "flag" events within $32\,\mu s$ of a beam-off period. Figure 3.15 shows a time spectrum for events with full duty-factor (top) and a time spectrum for flagged events which fail the duty factor cut (bottom). The distortion at long times is clearly seen. This cut results in a $2.2\,\%$ loss in statistics, consistent with the $\sim 98\%$ duty-factor seen at TRIUMF.

Cosmic Rays

The background due to cosmic rays and the inherent "room background"[5] is independent of the beam and was measured during periods when the cyclotron was off. The "cosmics" background measured during beam-off periods was manageably small (0.32 Hz total rate for all energies and 0.14 Hz in the energy window). When compared to a typical data run, this background accounts for 0.20 % of neutrons of all energies and only 0.16 % of neutrons in the energy window. Figure 3.16 shows a typical neutron energy spectrum. This background will be included in the constant,

[5]natural radioactivity, long-lived activation of air and shielding materials, etc.

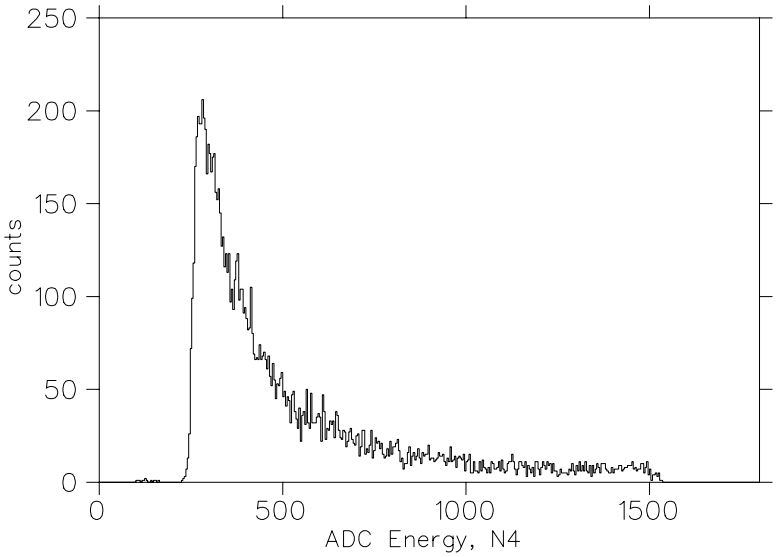

Figure 3.16: Neutron energy spectrum from detector N4, taken during a 46 hour beam/cyclotron-off period. This featureless spectrum shows the neutrons due to cosmic ray background. "Cosmic" neutrons account for 0.16 % of all neutron events in the relevant energy window.

time-independent term in the fit to the time spectrum.

Cyclotron-related

As with cosmic rays, the cyclotron-related neutrons only produce a flat background in the neutron time spectrum and thus can only degrade the statistical precision of the measurement. With the CW beam of the TRIUMF cyclotron, this background is constant and will not distort the time spectrum (note: this is *not* the case for a pulsed-beam experiment such as the Saclay measurement; they observed a complicated time dependence for beam-induced background, partly related to thermalization of neutrons generated in the beam burst).

The cyclotron-related background was measured when the primary proton beam was on but the M9B beam blocker was in (preventing muons from entering the area). These are presumably due to direct neutrons from the meson production target and/or the beam dump. In Figure 3.17, the histogram on the left shows

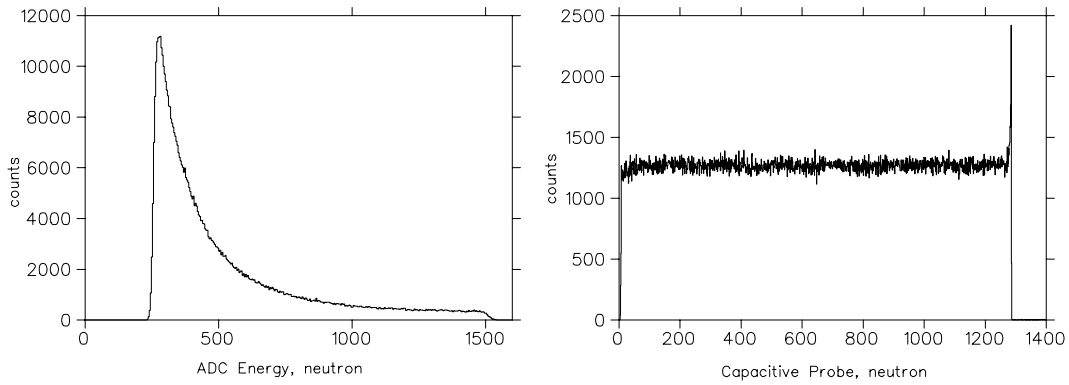

Figure 3.17: Neutron energy spectrum (left) from detector N4 with the cyclotron on but the MpB beam blocker in. This featureless spectrum shows the neutrons due to the cyclotron-related background. These neutrons account for 19 % of all neutron events in the relevant energy window. The capacitive probe spectrum (right) shows that these events are not time-correlated with the primary proton beam.

a typical, featureless neutron energy spectrum from these background runs. The histogram on the right is the capacitive probe signal (see Section 2.4.4) for neutrons which shows that these events are uncorrelated in time with the primary proton beam. This implies that the cyclotron-related background is comprised of mainly low-energy neutrons from a variety of locations and cannot be cut from the data with simple timing cuts based on the capacitive probe signal, nor with directional shielding.

Table 3.5 compares the neutron event rates from the cyclotron background running period to the rates from a production data run. The variations in rates from detector to detector are due to different target-detector distances and orientations with respect to shielding blocks, main beamline, beam dump, and T2 target[6]. The cyclotron-related background[7] accounts for 24 % of all neutrons and 19 % of neutrons within the energy window. When the muon beam rate is higher for a fixed proton beam current, the signal:noise ratio is also higher. This background will be included in a constant, time-independent term in the fit to the time spectrum.

[6]N1 is also different because of its different size and scintillating material.

[7]These rates also include neutrons due to cosmic events.

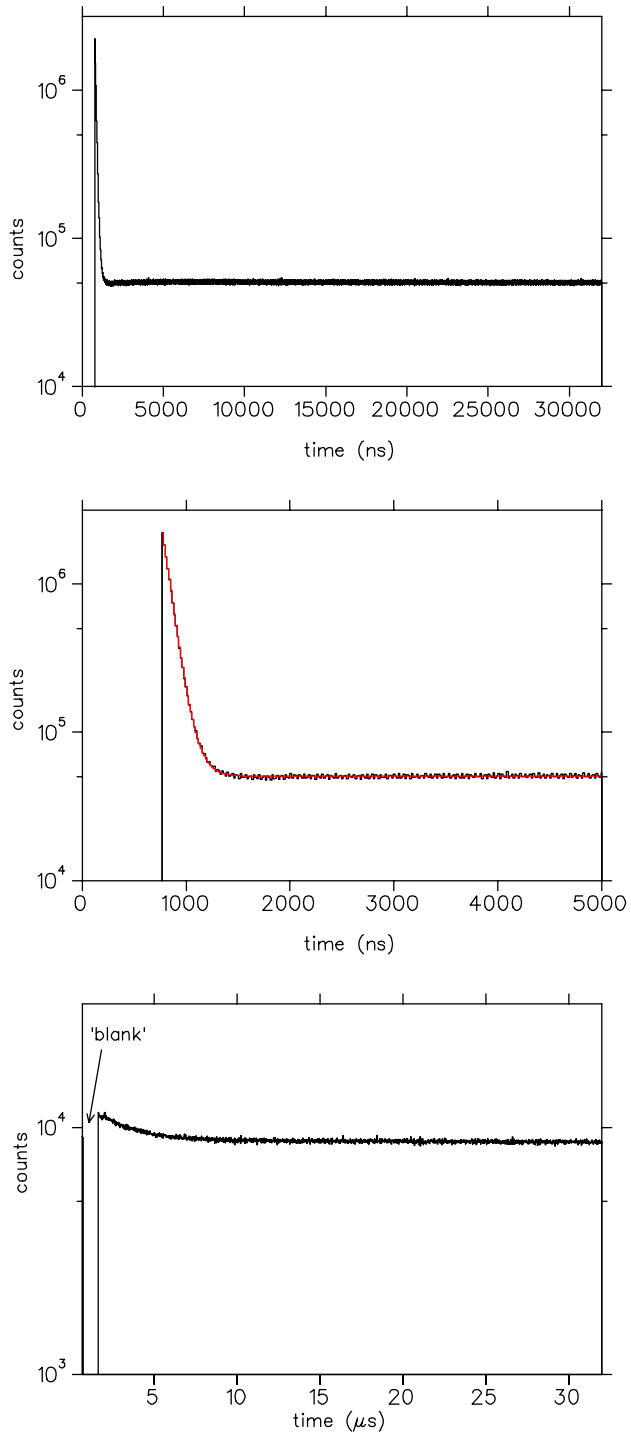

Figure 3.18: Full neutron time spectrum from μ^- production runs (top) clearly shows large peak in the early time. A close-up of the first $5\,\mu s$ (middle) shows the Au/Ag peak along with a fit to this spectrum which gives 84ns as the combined Au/Ag lifetime (histogram is the data, curve is the fit. The bottom spectrum shows the same data with a 900 ns blank cut applied. A clear hydrogen component can now be seen and the flat background has been reduced.

	Cyclotron Background Run		*Production Data Run*	
	all energies (Hz)	energy window (Hz)	all energies (Hz)	energy window (Hz)
N1	4.9	2.2	11.7	5.1
N2	6.2	3.9	21.7	12.0
N3	6.4	3.9	43.4	26.1
N4	13.2	4.5	40.8	23.9
N5	9.0	2.0	44.3	21.2
sum	39.7	16.5	162	88.3

Table 3.5: Neutron rates for all neutron energies and those within the OMC energy window during cyclotron background runs and a data production run. The cyclotron background runs ran over a period of 12.4 hours, and the production data were taken with a S1·S2 rate of 78 KHz. The cyclotron background accounts for 24 % of all neutrons and 19 % of neutrons within the energy window. These rates also include neutrons due to cosmic events.

Muon stops in target walls

Any μ^- that passes through the beam counters but stops in the walls of the target can produce neutrons from muon capture. Since the rate of OMC scales roughly as Z^4, even a small fraction of stops elsewhere than in the hydrogen will cause a potentially serious background. However, the target walls were constructed of gold and silver because the characteristic lifetime of a μ^- in a high-Z material is substantially shorter than in hydrogen, thanks to this higher capture rate. The μ^- lifetime in Au is $\tau_{\mu^-}^{\mathrm{Au}} = 73$ ns and in Ag is $\tau_{\mu^-}^{\mathrm{Ag}} = 89$ ns [40]. Thus, backgrounds from stops in the target walls are easily separated out via their time distribution. Since the Au and Ag lifetimes are so similar, it is difficult to distinguish the two components in the time spectrum fit, and they are considered here as a single term.

The neutron time spectrum in Figure 3.18 clearly shows the short-lifetime component from capture on Au and Ag (top spectrum). A fit to this spectrum results in a combined Au/Ag lifetime of 84 ns (middle spectrum). These Au/Ag neutron events, if left in the spectrum, produce a large flat background due to μ^- pileup which degrades the statistics on the signal from hydrogen. Therefore, a "blank" cut

is used to eliminate events in the first 400 ns of a prompt muon. The blank time was selected as a compromise between the error from the flat background due to Au/Ag pileup events and the OMC signal loss in the early part of the hydrogen time spectrum. Figure 3.18 (bottom spectrum) shows the resulting neutron time spectrum after the blank cut. In this figure, a 900 ns blank time is shown for illustrative purposes. For a 400 ns blank time, the signal loss is $\sim 20\,\%$. The small component of remaining Au/Ag events will be included in the final fit to the time spectrum.

Photo-neutrons and Photon Pileup

About 99.9% of the μ^-s stopping in the hydrogen target will simply decay. The abundant flux of low-energy photons generated by bremsstrahlung of the decay electrons will produce neutrons via (γ, n) reactions and "fake" neutrons from photon pileup. Both of these effects induce a background with a well-known time dependence given by $e^{-t/\tau_{\mu^-}}$. The amplitude of this background was determined using μ^+ beam data. The μ^+ beam provides the best way to characterize backgrounds associated with *muons* but not with *muon capture*.

The small number of photon pileup events that survive the PSD cuts described in Section 3.3.2 can be eliminated by a cut on the spectrum from the pileup circuit (shown in Figure 3.9). The effect of this cut is clearly seen when applied to the μ^+ data. Figure 3.19 shows a μ^+ time spectrum for all neutrons (and all detectors) which pass both PSD cuts (top), the same time spectrum after the pileup cut is applied (middle), and the events rejected by the pileup cut (bottom). The rejected events show a clear 2.2 μs time dependence (shown in the fit); therefore, the majority of these pileup events are "fake" neutrons from the pileup of two photons resulting from muon decay. This pileup cut reduces the statistics on production data by less than 1 %.

The neutron time spectrum with both the pileup cut and blank cut applied is

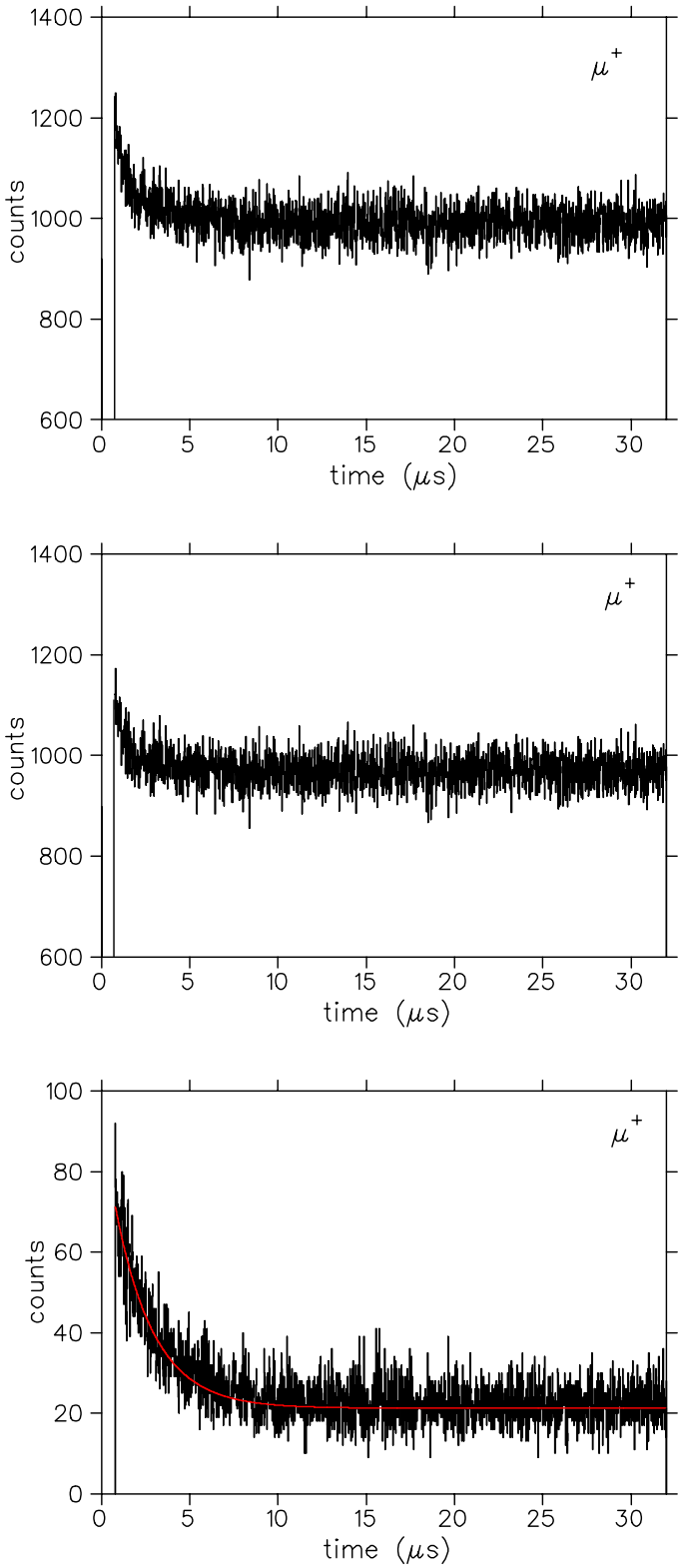

Figure 3.19: Time spectrum of μ^+ data for all neutrons (and all detectors) that pass both PSD cuts (top). The middle figure shows this spectrum after the pileup cut is applied. The time spectrum of the rejected pileup events (bottom) is then fit to the muon decay time. These data clearly show the 2.2 μs component.

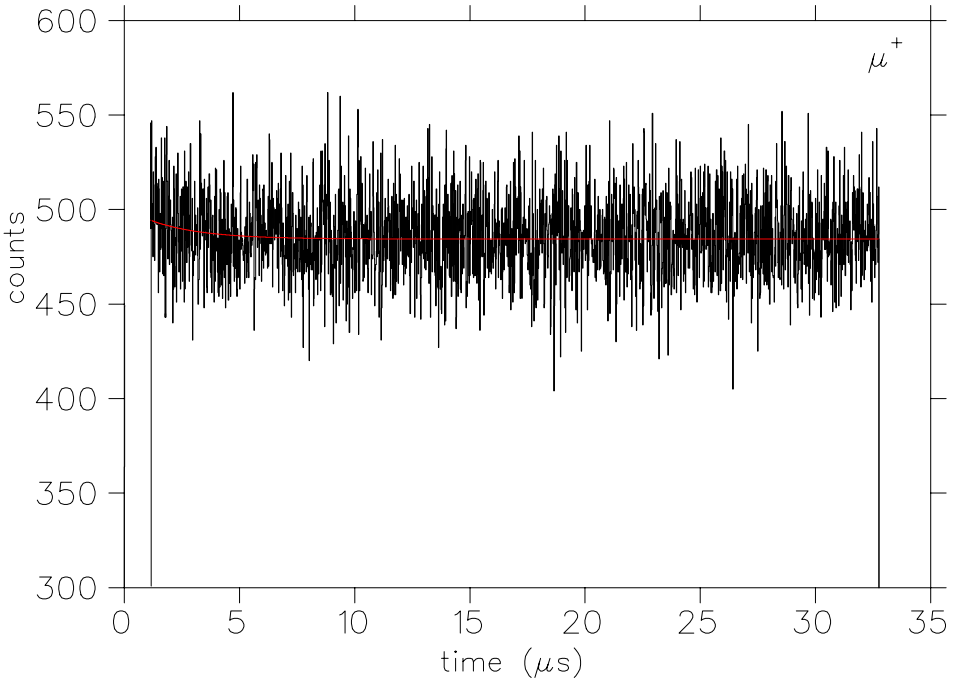

Figure 3.20: Neutron time spectrum of μ^+ data for all detectors with both the pileup and blank cuts applied. A fit to a component with a 2.2 μs lifetime is shown.

shown in Figure 3.20. These events are, presumably, due to (γ, n) reactions and have a 2.2 μs time dependence. They have been determined to account for $(2.9 \pm 0.9)\%$ of the events in the (μ^- beam) neutron time spectrum by taking the ratio of the amplitude of these events (determined from the fit) to the total number of μ^+-stops (corrected for livetime) and normalizing it to the similar ratio of the number of neutron events in the OMC window to the total number of μ^--stops (corrected for livetime).

Carbon

A final concern is muons stopping in the last beam scintillator. These produce neutrons with the lifetime of muons in carbon. Muons that stop in the first beam counter are not an issue because they would not have fired S2 and are therefore not counted as μ^--stop events. Other than Au, Ag, and H, the dominant material in

the target region is carbon (light guides and scintillators). The difference between the lifetime in carbon (2.0 μs) and hydrogen (2.2 μs) is of the order of $1/\lambda_{op}$ and so a significant carbon background could seriously affect the measurement.

The carbon component in the data was searched for in two ways. First, μ^- data were taken with an empty target. Without the hydrogen, the Au/Ag component will remain, but anything with a ≈ 2 μs lifetime is from the carbon. Secondly, a lead shield[8] was hung after S2, physically blocking the muons from entering the target. Again, there should be no hydrogen component; therefore, the remaining 2 μs events are carbon-related.

In analyzing the events from the Pb-shield data, it was determined that this method failed to accurately measure the background from carbon stops. The data showed a large component in the carbon and hydrogen lifetime region. This is potentially due to three factors. First, the lead was probably not thick enough to fully stop the muons. They may have retained enough momentum to continue to the target and stop in the hydrogen. Second, the shield may not have fully blocked the target allowing the muons to still reach the target. And finally, muons could have been scattered by the shield and stopped in the nearby charged-particle counter light guides, resulting in more carbon stops.

Fortunately, the empty target data were effective in determining the carbon background. The μ^- beam entering the empty target was stopped by the thick copper plate ($\tau_\mu^{Cu} = 164\,\text{ns}$ [40]) at the back of the target. The neutron time spectrum of these data clearly shows the Cu lifetime (see Figure 3.21). A fit to a single exponential (plus constant) gives a lifetime of $163 \pm 0.5\,\text{ns}$. When a carbon component is forced in the fit, the amplitude is zero (within error bars). Taking the ratio of the upper limits of the C amplitude to the number of μ^--stops in the empty

[8] The Pb shield was octagonal in shape with a diameter of 22 cm and with an irregular thickness between three and four millimeters.

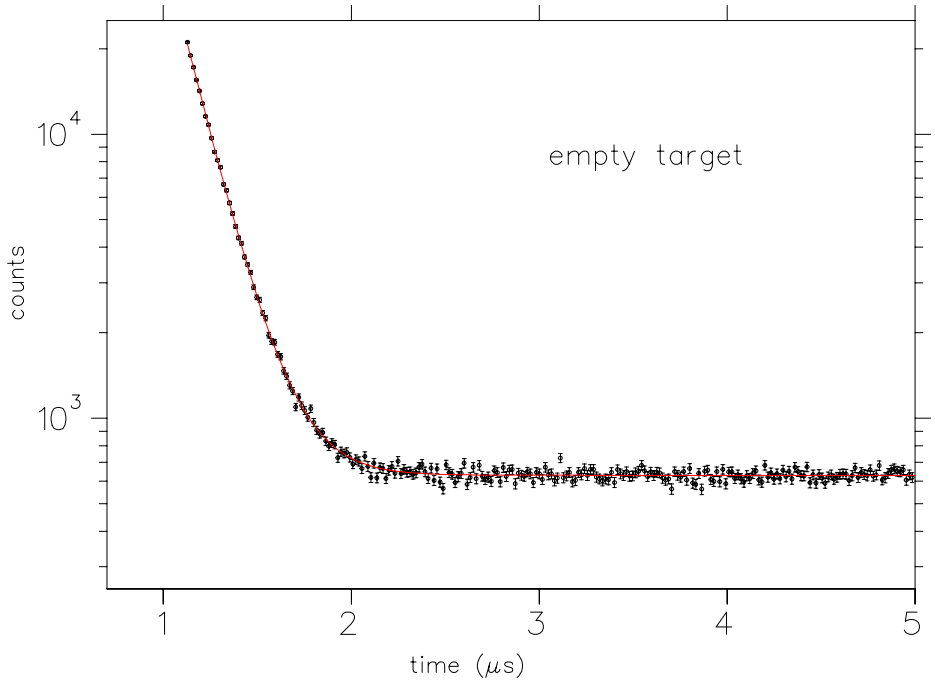

Figure 3.21: Neutron time spectrum (all detectors) for the empty target data. A fit to a single exponential (plus constant) gives the copper lifetime, showing that there is essentially no carbon component in the data.

target data and normalizing it to the similar ratio of the number of neutron events in the OMC window to the total number of μ^--stops in the production data [9], gives an upper limit (1σ) to the carbon background of 2.7 %.

Deuterium Contamination

The protium target's deuterium contamination given in Table 2.2 was higher than achieved in the RMC experiment. The effect of this contamination was determined by Monte Carlo simulations, with the deuterium contamination varying between (4 ± 2)ppm. The relevant processes in this background are

$$\begin{aligned} \mu p + d &\rightarrow \mu d + p \\ \mu d + p &\rightarrow p\mu d \\ p\mu d &\rightarrow {}^3\mathrm{He} + \mu \\ \rightarrow \mu^3\mathrm{He} \quad \text{or} \quad &\rightarrow {}^3\mathrm{He} + \mu \ . \end{aligned} \tag{3.3}$$

The muon can (and does) capture on deuteron and ^{3}He in the various states, thereby producing a neutron background. The muon also can be recycled at the end of the process. The Monte Carlo simulation uses the same neutron statistics, flat background, and conditions as the data from the experiment and varies the deuterium component (see Appendix A). From this study, it was determined that the deuterium contamination led to a large background (see Section 3.5).

3.4 Time Spectrum Analysis

This section further examines the effect of the backgrounds and cuts on the neutron time spectrum. The time spectrum analyzed is a sum of all the "good" μ^- data taken in the June-July 1999 and November 1999 production runs. Unless otherwise noted the following cuts are applied to the final neutron time spectrum:

[9] normalized and corrected for livetime

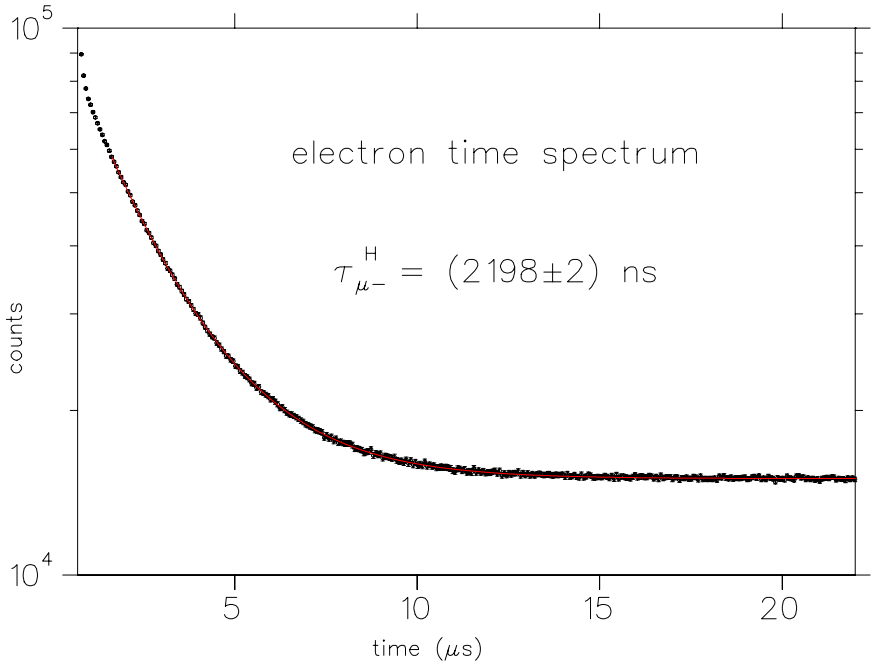

Figure 3.22: Time spectrum of electron events (all detectors). The fit to a single exponential (plus constant) gives $\tau_{\mu^-} = 2198 \pm 2$ ns.

pass PSD1 and PSD2, within the OMC energy window, blank time, no photon pileup, good duty factor, no events with > 15 hits, and no events within 4.5 μs of an S1·$\overline{\text{S2}}$. All these cuts have been described previously except for the S1·$\overline{\text{S2}}$ cut. This cut safeguards against events that occur close in time to a muon which hit S1 but did not go through S2. These events could result in muon capture on materials surrounding the target and increase the flat background.

3.4.1 Time Spectrum Calibration Checks

This measurement depends on the analysis of the time spectra generated by the multi-hit TDC. Thus, it is important to show that these time spectra can give accurate results. The fit to the empty target data resulted in $\tau_{\mu^-}^{Cu} = 163 \pm 0.5$ ns [40], which is within 1 ns of the known value. Also, the lifetime for the Au/Ag component (84 ns) was a reasonable mixture of the two separate lifetimes (73 and

89 ns, respectively [40]. These two examples show that the mhTDC is well calibrated. A final check on the accuracy of these time spectra is given by examining the decay electron time spectrum. A prescaled number of these triggers were taken during each run. Their time spectrum is shown in Figure 3.22. The fit to these data yields a muon lifetime in hydrogen of 2198 ± 2 ns, in good agreement with the accepted value of 2195 ns [40]. Therefore, there is nothing pathological about the time spectra in the production data.

3.4.2 Fitting Parameters and Ranges

In the next chapter a more complicated fitting function will be used. For simplicity, however, in this section the final μ^- production time spectra are fit to a single exponential,

$$y = Ae^{-t/\tau^n_{eff}} + C \quad , \tag{3.4}$$

where τ^n_{eff} is the effective lifetime of the muon for neutron events, A is the amplitude, and C is the flat background. Also, the fits begin at 2000 ns, or 1.26 μs after the prompt time[10] and extend to 30 μs. These values were chosen as a compromise between fitting error and the effect of the remaining Au/Ag component in the time spectrum (described in detail in the following section). Tables 3.6 and 3.7 show the effect of varying the start and stop time of the fit on τ^n_{eff}.

Remaining Au/Ag Component

The blank time cut extends 400 ns, starting at the prompt time. This cut allows some of the Au/Ag neutrons to remain in the spectrum. The effect of these remaining events on τ^n_{eff} was studied in two ways. The first was to fit the Au/Ag component in the "pre-blank" spectrum to determine the amplitude and then use this value (corrected for a 4 % random veto loss due to the blank) in a fixed Au/Ag

[10] prompt=740 ns.

Start time (ns)	τ_{eff}^{n} (ns)
1700	1866 ± 20
1900	1912 ± 25
2000	1912 ± 25
2100	1908 ± 25
2200	1916 ± 26
2300	1927 ± 29
2400	1946 ± 34
2500	1976 ± 38
2600	1976 ± 38

Table 3.6: Effect of the start time of the fit on the value of τ_{eff}^{n}. The end time is held fixed at 30000 ns and the Au/Ag component is ignored in the fit. From this study, a start time of 2000 ns was chosen. Note that t=0 (the prompt time) is at 740 ns.

component in the fit to the time spectrum with the blank cut applied. Using this extra term does not produce any deviation from the value for τ_{eff}^{n} obtained by starting the fit at 2000 ns or any later time. The second study involved fitting the entire time range of the "after blank" spectrum with an added Au/Ag term (not fixed). This extra term did not effect the value of τ_{eff}^{n}. It was, therefore, decided that the simplest option was to ignore the Au/Ag component by beginning the fit at 2000 ns, where the Au/Ag has long since died away. Figure 3.23 shows the neutron time spectrum (64 ns bins) with the fit for τ_{eff}^{n} and the fit extrapolated before 2000 ns to show the Au/Ag neutrons.

3.4.3 Consistency of τ_{eff}^{n}

Table 3.8 shows the results of the neutron time spectrum fits to Equation 3.4 for five data sets. The "Summer" data set contains all production data taken during the June-July 1999 run. The "Nov. (early)" data were taken as the cyclotron was run at low current and/or low duty-factor conditions. The "Nov. (middle)" data represent the bulk of the November 1999 production data. Towards the end of the November run the DC offset of one of the linear fan in/outs changed. The data from

End Time (ns)	τ^n_{eff} (ns)
30000	1912 ± 25
25000	1908 ± 28
20000	1916 ± 29
15000	1912 ± 32
10000	1873 ± 41
8000	1802 ± 57
6000	1757 ± 71
5000	1832 ± 140

Table 3.7: Effect of the end time of the fit on the value of τ^n_{eff}. The start time was held fixed at 2000 ns and the Au/Ag component is ignored in the fit. From this study, an end time of 30000 ns was chosen.

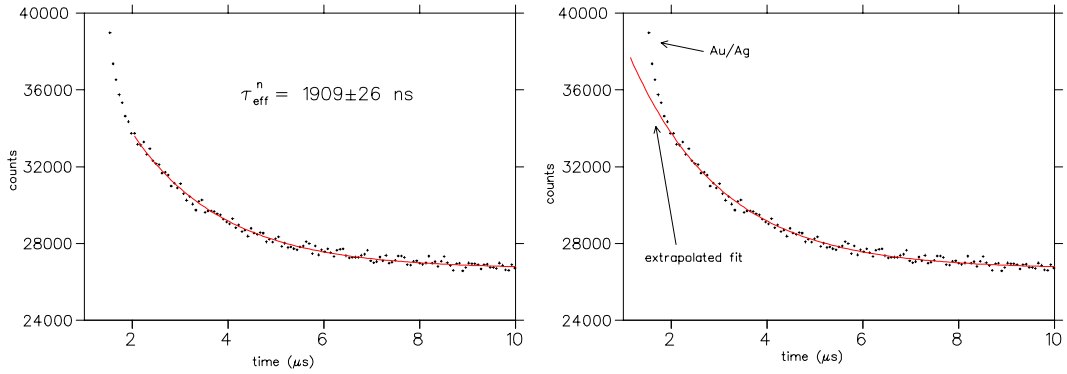

Figure 3.23: Final neutron time spectrum (64 ns bins) with fit (left) giving $\tau^n_{eff} = 1912 \pm 25$ ns. The spectrum on the right shows the same fit extrapolated before 2000 ns to show the Au/Ag neutrons.

these later runs are represented in the "Nov. (late)" data set. The "Grand Sum" is the sum of these four data sets. The Grand Sum results should and do agree (within error) with the individual data sets. The τ^n_{eff} and signal rate ("5.2 MeV n/μ^- stop") are also consistent throughout the runs. The average value for τ^n_{eff} is 1911 ± 26 ns. Therefore, τ^n_{eff} from the the Grand Sum, 1909 ± 26 ns, is an accurate representation of all the data.

Table 3.9 shows the value for τ^n_{eff} when the time spectrum from each detector is fitted separately. While there are unexplained non-statistical differences between

Data Set	*n's* ($\times 10^3$)	τ^n_{eff} *(ns)*	χ^2/dof	μ^- ($\times 10^8$)	*n's*/ μ^- ($\times 10^{-5}$)
Summer	155.0	1865 ± 40	1.058	105.8	1.47 ± 0.05
Nov. (early)	37.8	2137 ± 78	0.999	22.75	1.66 ± 0.09
Nov. (middle)	162.8	1891 ± 41	1.066	102.78	1.58 ± 0.06
Nov. (late)	47.2	1950 ± 91	0.999	33.94	1.39 ± 0.10
Grand Sum	405.7	1909 ± 26	1.182	265.16	1.53 ± 0.03
average		1911 ± 26			1.52 ± 0.03

Table 3.8: Results of the neutron time spectrum fits (range: 2000 ns→30 μs) to Equation 3.4 for five data sets. The "Grand Sum" is the sum of all good production data. The total number of neutrons in the spectra is 405700. There were approximately 1.5×10^{-5} OMC neutrons produced for every muon stopped in the target.

detectors and run periods, the average value here is also consistent with τ^n_{eff} from the Grand Sum and all detectors. In these results, the values of τ^n_{eff} measured by N1 are in poor agreement with the other detectors. However, the overall contribution of N1 to the statistics is very small, and the average value for τ^n_{eff} is changed very little with or without N1.

χ^2/dof

The χ^2 per degree of freedom (χ^2/dof) values of the fits are sensitive to the differential non-linearity of the mhTDC. The "size" of the individual time bins can vary by 10 % [44]. This can be seen in these data by fitting the neutron time spectrum at long times (*i.e.* 15→30 μs) to a constant (the flat background). In this fit $\chi^2/\text{dof} = 1.16$. However, if the data are rebinned into 64 ns bins, then χ^2/dof for this fit is 1.013. Therefore, the χ^2/dof is sensitive to the differential non-linearity of the mhTDC, but at adequate binnings, it does not affect the results.

3.4.4 Effect of Cuts on τ^n_{eff}

The pileup and S1·$\overline{\text{S2}}$ cuts are important to producing a clean data spectrum. Thus, their effect on the ability to measure τ^n_{eff} was studied. When the pileup cut

τ^n_{eff} (ns)	N1	N2	N3	N4	N5
Summer	1852 ± 237	2037 ± 108	1821 ± 53	1686 ± 122	1919 ± 74
Nov. (early)	2949 ± 435	2193 ± 192	1887 ± 93	2198 ± 256	2227 ± 149
Nov. (middle)	1450 ± 820	2092 ± 101	1742 ± 55	1848 ± 140	1890 ± 82
Nov. (late)	2273 ± 310	2041 ± 208	1866 ± 118	2326 ± 649	1672 ± 154
Grand Sum	2155 ± 125	2075 ± 69	1802 ± 32	1835 ± 91	1908 ± 47
average (ns)	1894 ± 22				

Table 3.9: Results for τ^n_{eff} when the time spectrum from each detector is fitted separately. The average value here is also consistent with τ^n_{eff} from the Grand Sum and all detectors.

	A	C	τ^n_{eff} (ns)	$\Sigma(\times 10^7)$	A:C
pileup cut					
with			1909 ± 26	1.400	
without			1921 ± 25	1.411	
S1·$\overline{\text{S2}}$ cut					
with	5049	6670	1909 ± 26	1.400	0.757
without	4930	7725	1973 ± 28	1.616	0.638

Table 3.10: Effect of pileup and S1·$\overline{\text{S2}}$ cuts on τ^n_{eff}. A and C refer to the amplitude and constant in the fits, respectively. The Σ column shows the total neutron events in each spectra. The ratio A:C characterizes the resulting signal to noise ratio.

is removed from the final neutron time spectrum, there is a 1 % increase in events in the histogram. This extra 1 %, however, consists mainly of $\gamma\gamma$ pileup events, which can affect the ability to fit τ^n_{eff}. The S1·$\overline{\text{S2}}$ provides protection against uncorrelated neutron events resulting from a stop in carbon or material other than protium in the target area. With this cut, the signal-to-noise ratio increases by 18 % without any loss in signal. These two studies are summarized in Table 3.10.

3.4.5 Multiple Muon Rejection

A final check on this analysis is to verify that the result for τ^n_{eff} is not somehow effected by the use of multiple muon arrivals (recorded with the mhTDC). A cut is placed on the data to reject events with more than one muon arrival within 12 μs of

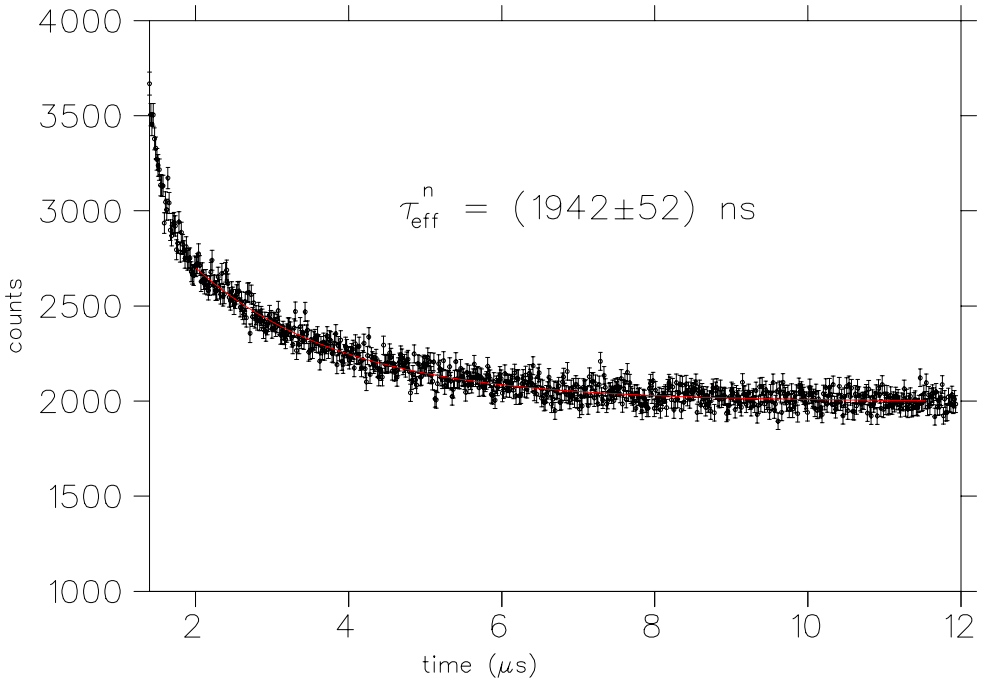

Figure 3.24: Neutron time spectrum with multiple muon rejection. The data (points) are fit to Eq. 3.4 (curve). τ^n_{eff} is consistent with the result using multiple muons.

the prompt time. The resulting spectrum is shown in Figure 3.24. The fit results in $\tau^n_{eff} = 1942 \pm 52$ ns, which agrees with τ^n_{eff} obtained using multiple muon arrivals, but has a larger error because of the poorer statistics.

3.5 Summary

The analysis presented in this chapter produced $\tau^n_{eff} = (1909 \pm 26)$ ns. Figure 3.25 shows the full neutron time spectrum (after cuts) and the fit for τ^n_{eff}. There are three corrections to this result that are required. Each correction is obtained by increasing the number of neutron events in Eq. 3.4 by the amount of background events and observing what this effect does to τ^n_{eff} in the fit and then varying the increased number of events by the error on each measurement to find the uncertainties. The resulting correction due to the remaining (γ,n) and pileup events, measured using μ^+ beam data, is $-(7 \pm 2)$ ns. The carbon component in

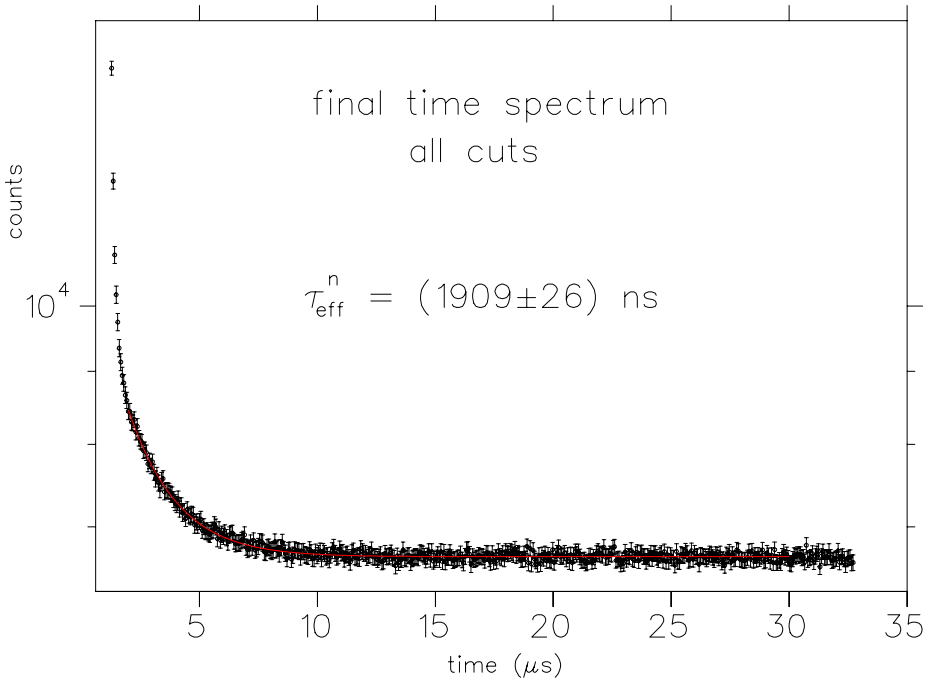

Figure 3.25: Final neutron time spectrum (16 ns bins) with all cuts applied. The fit (starting at 2000 ns) yields $\tau^n_{eff} = 1909 \pm 26)$ ns.

the time spectrum results in a $-(1.6 \pm 1.6)$ ns shift in τ^n_{eff}. The largest correction, due to deuterium contamination, is $-(32 \pm 15)$ ns. Combining these corrections and adding the systematic and statistical errors in quadrature, yields a final effective lifetime of

$$\tau^n_{eff} = (1868 \pm 30)\,\text{ns} \quad . \tag{3.5}$$

The following chapter will present the extraction of λ_{op} from this τ^n_{eff} and discuss the implications of this result.

CHAPTER 4

Results and Conclusions

4.1 Functional Form

In the previous chapter the neutron time spectrum was fit to a single exponential function. However, the full function (without approximations) that describes the neutron time spectrum in this molecular system is

$$\frac{dn}{dt} = Ae^{-t/\tau_{\mu^-}} \left\{ \lambda_{om} e^{-(\lambda_{om}+\lambda_{op})t} + \frac{\lambda_{pm}\lambda_{op}}{(\lambda_{om}-\lambda_{pm}+\lambda_{op})} \left[e^{-\lambda_{pm}t} - e^{-(\lambda_{om}+\lambda_{op})t} \right] \right\} \quad (4.1)$$

where λ_{om} and λ_{pm} are the capture rates from the ortho- and para-molecular states, respectively. This relationship arises from solving the coupled system of ordinary differential equations represented by Figure 1.1 (the $\lambda_{p\mu p}$ formation is neglected here). When the approximations,

$$\begin{aligned} \tau_{\mu^-} &\simeq \frac{1}{(1/\tau_{\mu^-})+\lambda_{om}} \\ \frac{\lambda_{om}}{\lambda_{pm}} &\approx 1 \\ \lambda_{op} &\gg \lambda_{om}-\lambda_{pm} \quad , \end{aligned} \quad (4.2)$$

are applied, this function reduces to

$$\frac{dn}{dt} = Ae^{-t/\tau_{\mu^-}} \left[e^{-\lambda_{op}t}(\lambda_{om}-\lambda_{pm}) + e^{-\lambda_{pm}t}\lambda_{pm} \right] \quad . \quad (4.3)$$

It was verified numerically that Equations 4.1 and 4.3 agree to very high accuracy for physically reasonable values of the constants.

The extraction of λ_{op} from fitting the data to Eq. 4.3 depends, clearly, on the values chosen for the other parameters, λ_{om}, λ_{pm}, and τ_{μ^-}. The muon lifetime is

very precisely known, so its contribution to the uncertainty is negligible. However, there are errors associated with the known values of both λ_{om} and λ_{pm}. The values quoted in Reference [19] are

$$\lambda_{om} = (530 \pm 20)\,\mathrm{s}^{-1} \qquad (4.4)$$
$$\lambda_{pm} = (200 \pm 10)\,\mathrm{s}^{-1} \quad .$$

The effect of these errors was studied by varying each, within their error range, in data generated using Eq. 4.1 with the same neutron statistics and flat background as the data from the experiment. These data were then fit with a single exponential (Eq. 3.4). The error in λ_{om} results in a 5 ns fluctuation in τ^n_{eff}, while λ_{pm} results in an 8 ns variation. Adding in quadrature these errors to the experimental error gives a total uncertainty on τ^n_{eff} of ± 31 ns.

4.2 Extraction of λ_{op}

The relationship between τ^n_{eff} and λ_{op} was found empirically by, again, generating data using Eq. 4.3 with the same background and statistics as the measurement, $\tau_{\mu^-} = 2195$ ns, and λ_{om} and λ_{pm} given above. These data were fit to Eq. 3.4. The function relating τ^n_{eff} and λ_{op} is then determined from this data fit[1] (see Figure 4.1). Using this function, then

$$\tau^n_{eff} = (1868 \pm 31)\ \mathrm{ns} \qquad (4.5)$$

corresponds to

$$\lambda_{op} = (13.8 \pm 1.6) \times 10^4\,\mathrm{s}^{-1} \qquad (4.6)$$

which varies significantly from the Bardin *et al.* result ($\tau^{\mu^-}_n = (2084 \pm 30)$ ns and $\lambda_{op} = (4.1 \pm 1.4) \times 10^4\ \mathrm{s}^{-1}$) [15, 27].

[1] As a consistency check, it was verified that using this empirical function the τ^n_{eff} obtained by Bardin *et al.* [15, 27] yields the same λ_{op} as reported in their publications.

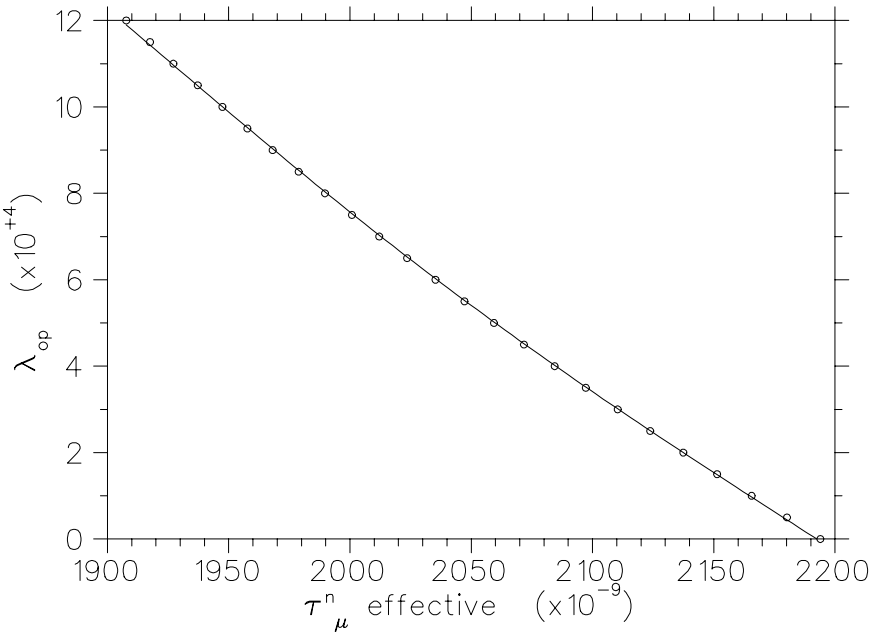

Figure 4.1: λ_{op} (s^{-1}) *vs.* τ^n_{eff} (ns) as determined using data generated with Eq. 4.3 and fit to Eq. 3.4.

4.3 Implications of λ_{op}

This value of λ_{op} is approximately three times higher than the value measured by Bardin *et al*, $(4.1 \pm 1.4) \times 10^4\,s^{-1}$. In fact, using the combined error from both experiments, this new value of λ_{op} is 5σ away from the Bardin *et al* value. This λ_{op} is also approximately twice the theoretical calculation by Bakalov *et al.* The difference between τ^n_{eff} and the hydrogen lifetime with $\lambda_{op} = 0$ (2195 ns) is 327 ns $\pm$ 30ns. This 10σ effect cannot be due to a statistical fluctuation. Figure 4.2 shows the data in coarse bins (512 ns) with both the τ^n_{eff} fit (solid curve) and a fit with τ^n_{eff} fixed to 2195 ns (dashed curve). Although the difference between the two fits is subtle, there is a clear agreement between the measured τ^n_{eff} and the data.

This new value for λ_{op} cannot be reconciled with the previous experiment by assuming that either the deuterium, carbon, or photon-neutron backgrounds are higher than measured in this experiment. A larger value for the deuterium compo-

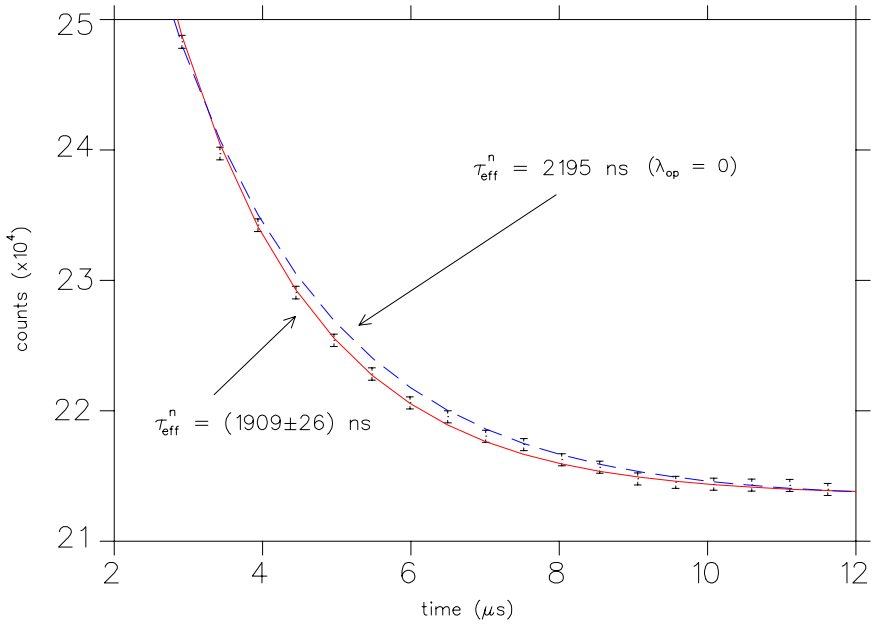

Figure 4.2: Final neutron time spectrum (512 ns bins) fit to Eq. 3.4 with τ^n_{eff} =1909 ns (solid curve) and fit with τ^n_{eff} fixed to the muon lifetime, *i.e.* λ_{op} =0 (dashed curve).

nent, by far the dominant background, can only increase the value of λ_{op} further. The same is true for the carbon and (γ, n) components. If these three backgrounds are smaller than the values obtained through the analysis, the resulting lower λ_{op} is still very high, compared to both the previous theory and experiment. The only factor which could significantly reduce λ_{op} is a large component due to a material with a much faster lifetime than the measured τ^n_{eff}. If this lifetime is too fast though, it will be eliminated by the blank time cut. However, the effect of such a material should have been seen in the empty target data. Since these data showed no indication of any such material, it must be assumed that there is no such offending component.

This new λ_{op}, taken at face value, has vast implications for the experimental situation for both g_p and λ_{op}. Figure 4.3 is essentially Figure 1.3 with the new λ_{op} indicated. Based upon this result, the two most precise measurements of g_p, RMC

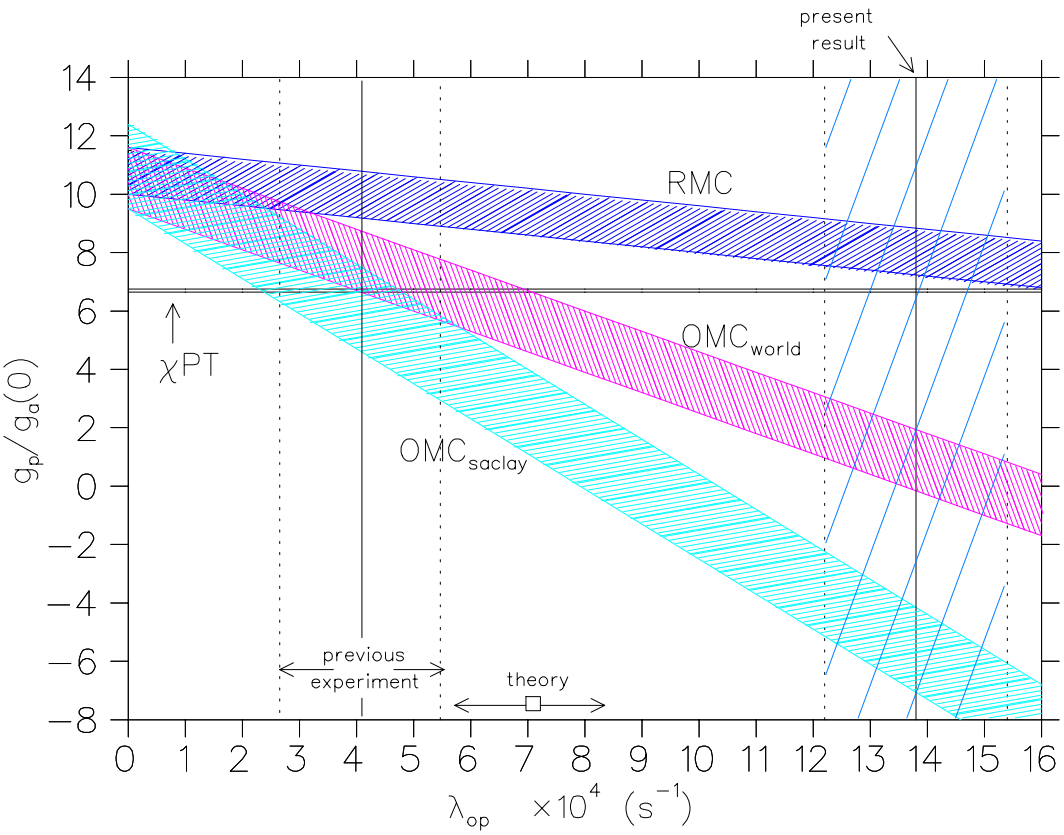

Figure 4.3: $g_p/g_a(0)$ *vs.* λ_{op}. Indicated are the values of λ_{op} for the present result, the previous measurement, and the theoretical result. The χPT value for $g_p/g_a(0)$ is noted. The dependence of each g_p measurement on λ_{op} is shown.

and OMC$_{saclay}$ seem to be in severe disagreement[2]. The RMC result is now within 1σ of the χPT value. When the previous two values for λ_{op} (one experimental, one theoretical) are assumed the OMC measurements are in agreement with χPT. However, this new λ_{op} calls into doubt the OMC$_{saclay}$ results.

4.4 Outlook

Assuming this new value of λ_{op} is taken at face value and in light of the implications of this result, three suggestions for future action are presented here.

[2]OMC$_{world}$ is a weighted average of all g_p^{OMC} measurements, dominated by OMC$_{saclay}$.

4.4.1 Theoretical Calculation

The only previous calculation of λ_{op} lies in stark contrast with this new result. An updated look at the theory would be of interest, to see if the larger value of λ_{op} measured here can be reconciled with a more detailed understanding of the $p\mu p$ system.

4.4.2 New OMC Measurement

A novel measurement of g_p^{OMC} is underway at Paul Scherrer Institute (PSI). The μ^- Cap experiment proposes to measure the singlet capture rate to 1 % [52]. The experiment uses ultra-clean, deuterium-depleted H_2 gas at 10 bar, surrounded by a time projection chamber (TPC) to provide an active target. The low density (compared to liquid H_2) used thereby eliminates the uncertainties due to $p\mu p$ formation and λ_{op} and ensures that capture takes place from the singlet hyperfine state. The singlet capture rate will be determined from the difference between the effective lifetime of the μ^- in the target and the μ^+ lifetime in the target, *i.e.* $\lambda_s = \lambda_{\mu^-} - \lambda_{\mu^+}$. The value of g_p will then be deduced from this capture rate, with an anticipated 7 % precision. Production data-taking will begin in late 2002.

4.4.3 RMC

The TRIUMF RMC measurement represents the only body of work on this intriguing facet of the g_p puzzle. Since the announcement of the RMC result there has been much theoretical activity to understand its seemingly anomalous value of g_p [53, 54, 55, 56, 57, 58, 59, 60]. The review article by Gorringe and Fearing [30] includes discussion about these new developments. The present new value for λ_{op} certainly makes the RMC result more plausible. It would, therefore, be of considerable interest to perform a new measurement of the RMC process. Although, the method for achieving this is unclear at this time, a measurement with gaseous hy-

drogen would be of particular interest, although certainly a challenging experiment.

4.5 Suggestions for Further Work on λ_{op}

Although this experiment succeeded in its goal to measure λ_{op}, several ideas surfaced in the course of analyzing these data that could be used to perform an improved experiment. These include:

1. The experiment was designed with a highly pure protium target in mind. However, the true level of deuterium contamination was much higher than anticipated. This contamination proved to be a hindering background. It was unknown at the time of the experiment that this level of contamination was present. Indeed, all the earlier gas contamination measurements made during the RMC data runs indicated a contamination level < 1 ppm. Had the level been known before the data runs, measures could have been taken, such as replacing the contaminated protium.

2. The liquid scintillation detectors are a key component in this experiment. However, only three of the five detectors were functioning optimally[3]. The final statistics would have been improved with the use of at least six fully functioning, identical neutron detectors.

3. The dominant source of error in the result is from statistics. Crucial beam time was lost due to a few factors. First, towards the middle of the June-July 1999 run, there was a problem with the cyclotron facility that prevented the cyclotron from delivering beam to the experimental halls. When the beam did return (in November 1999), the cyclotron could not be operated at full current and duty-factor in the first portion of that run. Second, there were a few

[3]The original N1 was damaged and therefore replaced by a detector with different scintillation properties. N3 had problems with sparking and had to be operated at a lower high voltage.

smaller malfunctions in beamline equipment which caused a loss in beam time, *e.g.* a power bump took down the M9B superconducting solenoid for over 12 hours. While both of these problems were uncontrollable, the final concern was not. The setup and troubleshooting of the electronics took far longer than anticipated. The experiment was well into its allotted beam time by the time that all elements were functioning optimally. However, several of these components cannot be properly setup without the beam. Therefore, a reasonable amount of time for the setup of electronics should be requested in the original beam time proposal.

4. The mhTDC was not used to its full potential. In analyzing the data, it was realized that the "time history" of signals other than just the beam would have been useful. For instance, it would have been beneficial to see the pulses in the neutron detectors before a trigger event. Also, vetoing abilities would been improved by putting the signal from each charged particle veto counter instead of just the sum of the E counters. This way, one would know which counter caused the veto.

5. The pulse shape discrimination is crucial to the experiment. Ideally, one would like to see the entire pulse shape, which would allow precise PSD in software. One could conceive of using transient digitizers for this purpose. Transient digitizers act like digital oscilloscopes, essentially taking a snapshot of each input pulse. Using this, the experimenter would be able to literally see the pulse shape of each signal in the neutron detectors, for instance. An event display program could be used to categorize each pulse according to pulse shape (but could be verified visually by the experimenter).

4.6 Summary and Conclusions

This experiment measured the ortho-para transition rate in muonic molecular hydrogen as

$$\lambda_{op} = (13.8 \pm 1.6) \times 10^4\,\mathrm{s}^{-1} \quad . \tag{4.7}$$

The dominant background is the deuterium contamination in the liquid hydrogen target. Only small backgrounds arise from muon capture on carbon and (γ,n) interactions from decay electrons. The error on the measurement is dominated by statistics and the uncertainty in the deuterium component.

This λ_{op} is three times higher than the value obtained in the only previous measurement and twice the value of the only theoretical calculation. These discrepancies cannot be explained through any unknown background effects or statistical fluctuations.

If taken at face value, this result has vast implications for the previous measurements of both λ_{op} and g_p, the induced pseudoscalar coupling of the proton. One of the original intentions of this experiment was to provide a clearer picture for the experimental situation for g_p. Regrettably, this is not the case. However, a large λ_{op} adds an intriguing new facet to this puzzle. It is my hope that this result will stimulate intense consideration and study in this exciting field.

APPENDIX A

Deuterium Contamination

The deuterium contamination present in the target ((4 ± 2) ppm) produced a relatively large neutron background from muon capture in the following processes:

$$\mu p + d \rightarrow \mu d + p \tag{A.1}$$

$$\mu d + p \rightarrow p\mu d$$

$$p\mu d \rightarrow {}^3\mathrm{He} + \mu$$

$$\rightarrow \mu{}^3\mathrm{He} \quad \text{or} \quad \rightarrow {}^3\mathrm{He} + \mu \ .$$

Figure A.1 shows these processes along with the relevant formation rates of the μd atomic and molecular states.

The muon is more tightly bound (by $\sim$135 eV) in the μd atom than in the μp atom, due to the increased mass of the μd system [61]. Therefore, the muon has a high "attraction" to the deuterium, and the μd formation rate ($10^{10}\,\mathrm{s}^{-1}$) is consequently higher than any other in the system.

Once the $p\mu d$ state forms, muon-catalyzed fusion can occur. The muon either fuses the pd and is then ejected or fuses the pd and becomes bound to the resulting ^{3}He atom. The muon in the bound $\mu{}^3$He state can then be captured, producing the following three final states:

$$\mu + {}^3\mathrm{He} \rightarrow {}^3\mathrm{H} + \nu \tag{A.2}$$

$$\mu + {}^3\mathrm{He} \rightarrow {}^2\mathrm{H} + n + \nu$$

$$\mu + {}^3\mathrm{He} \rightarrow p + n + n + \nu \ .$$

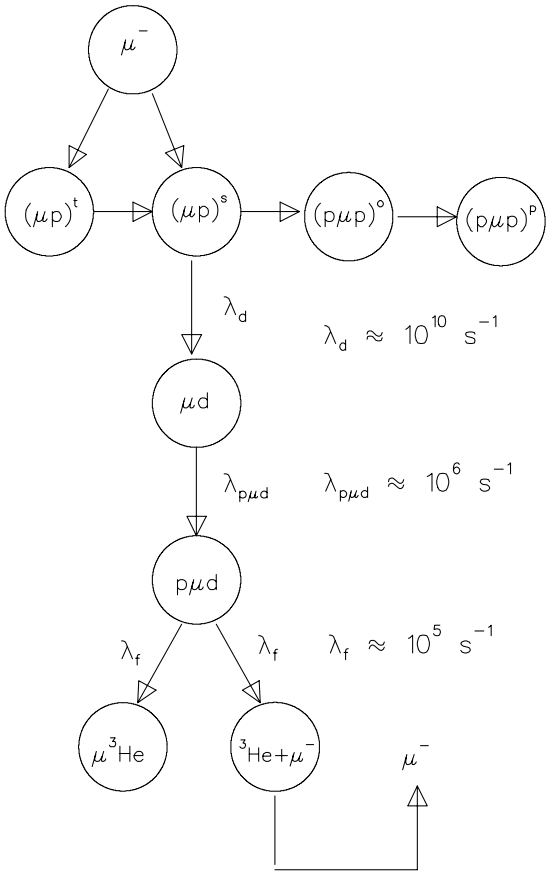

Figure A.1: Kinetics of deuterium contamination in the target. λ_d is the formation rate of the μd atom. $\lambda_{p\mu d}$ is the formation rate of the $p\mu d$ molecule. λ_f is the formation rate of the two distinct fusion states.

The relevant muon capture rates are given below [61], where $\lambda_{\mu d}$, $\lambda^c_{p\mu d}$, and $\lambda_{\mu^3\mathrm{He}}$ are the capture rates from the μd atom, $p\mu d$ molecule, and μ^3He states, respectively.

- $\lambda_s \approx 600\,\mathrm{s}^{-1}$
- $\lambda_{om} \approx 530\,\mathrm{s}^{-1}$
- $\lambda_{pm} \approx 200\,\mathrm{s}^{-1}$
- $\lambda_{\mu d} \approx 150\,\mathrm{s}^{-1}$
- $\lambda^c_{p\mu d} \approx 280\,\mathrm{s}^{-1}$
- $\lambda_{\mu^3\mathrm{He}} \approx 2150\,\mathrm{s}^{-1}$

Figure A.2 shows the result of Monte Carlo simulations of the neutron contributions from the atomic and molecular states for a deuterium contamination of 4 ppm and $\lambda_{op} = 13.8 \times 10^4\,\mathrm{s}^{-1}$. The system must be simulated using Monte Carlo approximations because of the complexity of the recycled muon. The figure clearly demonstrates that the effect of the large μ^3He component will increase the τ^n_{eff} obtained from the OMC neutron time spectrum. The resulting correction to τ^n_{eff} is determined empirically by varying the contamination between $2 - 6$ ppm.

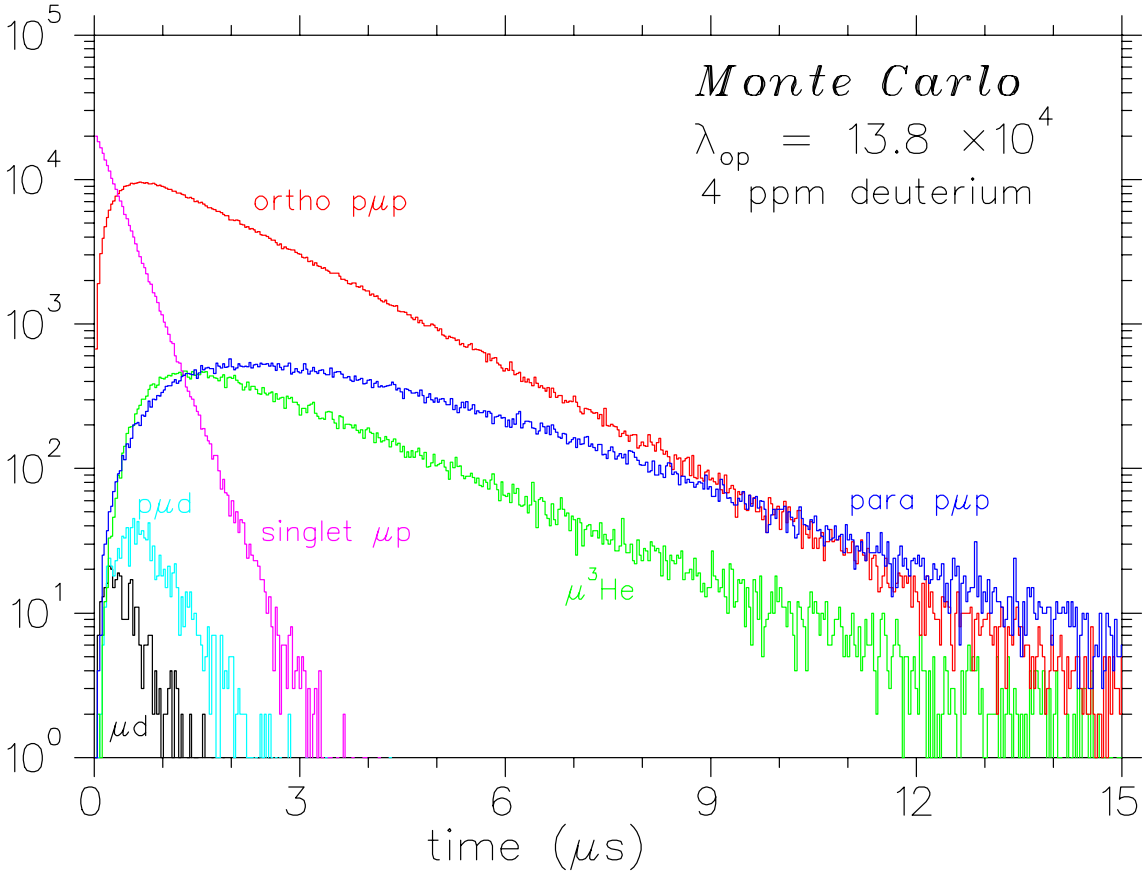

Figure A.2: Time evolution of capture neutrons in deuterium contamination. This spectrum is produced using Monte Carlo simulations with a deuterium contamination of 4 ppm and $\lambda_{op} = 13.8 \times 10^4\,\mathrm{s}^{-1}$.

BIBLIOGRAPHY

[1] K. Hagiwara *et al.* (Particle Data Group), Physical Review D **66**, 010001 (2002).

[2] S. Glashow, Nucl. Phys. **22**, 579 (1961).

[3] S. Weinberg, Phys. Rev. Lett. **19**, 1264 (1967).

[4] A. Salam, *Elementary Particle Physics (Nobel Symp. No. 8)* (Almqvist and Wilsell, Stockholm, 1968), p. 367.

[5] L. Grenacs, Ann. Rev. Nucl. Part. Sci. **35**, 455 (1985).

[6] R.P. Feynman and M. Gell-Mann, Phys. Rev. **109**, 193 (1953).

[7] John Dirk Walecka, *Electron scattering for nuclear and nucleon structure* (Cambridge University Press, New York, 2001).

[8] M. Gell-Mann and M. Levy, Nuovo Cimento **16**, 705 (1960).

[9] Y. Nambu, Phys. Rev. Lett. **4**, 380 (1960).

[10] M.L. Goldberger and S.B. Treiman, Phys. Rev. **110**, 1178 (1958).

[11] P. Bopp *et al.*, Phys. Rev. Lett. **56**, 919 (1986).

[12] T.P. Cheng and L.F. Li, *Gauge Theory of Elementary Particle Physics* (Oxford University Press, New York, 1984), pp. 153–154.

[13] V. Bernard, N. Kaiser, and Ulf-G. Meissner, Phys. Rev. D **50**, 6899 (1994).

[14] J.D. Walecka, *Theoretical Nuclear and Subnuclear Physics* (Oxford University Press, New York, 1995).

[15] G. Bardin *et al.*, Phys. Lett. **104B**, 320 (1981).

[16] E. Zavattini, in *Muon Physics*, edited by V.W. Hughes and C.S. Wu (Academic Press, New York, 1975), Vol. II.

[17] D.D. Bakalov *et al.*, Nucl. Phys. **A384**, 302 (1982).

[18] L. Ponomarev, in *Muonic Atoms and Molecules*, edited by L. A. Schaller and C. Petitjean (Birkhauser Verlag, Basel, 1993).

[19] D.F. Measday, Physics Reports **354(4-5)**, 243 (2001).

[20] E. Bertolini *et al.*, in *Proc. Intern. Conf. on High-Energy Physics*, edited by J. Prentki (CERN, Geneva, 1962), p. 421.

[21] R. Hildebrand, Phys. Rev. Lett. **8**, 34 (1962).

[22] E.J. Bleser *et al.*, Phys. Rev. Lett. **8**, 288 (1962).

[23] J.E. Rothenberg *et al.*, Phys. Rev. **132**, 2664 (1963).

[24] A. Alberigi Quaranta *et al.*, Phys. Rev. **177**, 2118 (1969).

[25] V.N. Bystritskii *et al.*, Sov. Phys. JETP **39**, 19 (1974).

[26] G. Bardin *et al.*, Nucl. Phys. **A352**, 365 (1981).

[27] G. Bardin, Ph.D. thesis, U. de Paris-Sud (Orsay), 1982.

[28] G. Jonkmans *et al.*, Phys. Rev. Lett. **77**, 4512 (1996).

[29] D.H. Wright, Phys. Rev. C **57**, 373 (1998).

[30] T.P. Gorringe and H.W. Fearing, Induced pseudoscalar coupling of the proton weak interaction, nucl-th/0206039 v1, 2002, submitted to *Rev. Mod. Phys.*

[31] D.S. Beder and H.W. Fearing, Phys. Rev. D **39**, 3493 (1989).

[32] S. Weinberg, Phys. Rev. Lett. **4**, 575 (1960).

[33] Ya. B. Zel'dovich and S.S. Gershtein, Sov. Phys. JETP **8**, 453 (1959).

[34] L.I. Ponomarev and M.P. Faifman, Sov. Phys. JETP **44**, 886 (1976).

[35] J. Martino, Ph.D. thesis, U. de Paris-Sud (Orsay), 1982.

[36] http://www.triumf.ca.

[37] D.H. Wright *et al.*, Nucl. Instrum. and Methods **A320**, 249 (1992).

[38] W. Bertl, D. Healey, J. Zmeskal, M.D. Hasinoff, M. Blecher, and D.H. Wright, Nucl. Instrum. and Methods **A355**, 230 (1995).

[39] Department of Earth Sciences, University of Waterloo, Waterloo, Ontario, Canada N2L 3G1.

[40] T. Suzuki, D.F. Measday, and J.P. Roalsvig, Phys. Rev. C **35**, 2212 (1987).

[41] G.F. Knoll, *Radiation detection and measurement*, 2nd ed. (Wiley, New York, 1989).

[42] W.R. Leo, *Techniques for Nuclear and Particle Physics Experiments*, 2nd ed. (Springer-Verlag, New York, 1994).

[43] J.R.M. Annand, Nucl. Instrum. and Methods **A262**, 371 (1987).

[44] Model 3377, 32 Channel CAMAC TDC, LeCroy Research Systems, Chestnut Ridge, NY.

[45] T. Okuda, H. Yamazaki, M. Kawabata, J. Kasagi, and H. Harada, Nucl. Instrum. and Methods **A426**, 497 (1999).

[46] http://midas.triumf.ca.

[47] http://wwwinfo.cern.ch/asd/paw/.

[48] http://www.triumf.ca/physica/html/homepage.html.

[49] http://daq.triumf.ca/online/vdacs/index.html.

[50] http://daq.triumf.ca/nova/.

[51] R.A. Cecil, B.D. Anderson, and R. Madey, Nucl. Instrum. and Methods **161**, 439 (1979).

[52] P. Kammel *et al.*, Nucl. Phys. **A663-664**, 911 (2000).

[53] V. Bernard, H.W. Fearing, T.R. Hemmert, and Ulf-G. Meissner, Nucl. Phys. **A635**, 121 (1998).

[54] S. Ando, F. Myhrer, and K. Kubodera, Phys. Rev. C **63**, 015203 (2000).

[55] H.W. Fearing, R. Lewis, N. Moder, and S. Scherer, Phys. Rev. D **56**, 1783 (1997).

[56] S. Ando and D-P. Min, Phys. Lett. B **417**, 177 (1998).

[57] T. Meissner, F. Myhrer, and K. Kubodera, Phys. Lett. B **416**, 36 (1998).

[58] E. Truhlik and F. Khanna, On Radiative Muon Capture in Hydrogen, nucl-th/0102006 v2, 2001.

[59] S. Ando, F. Myhrer, and K. Kubodera, Analysis of Ordinary and Radiative Muon Capture in Liquid Hydrogen, nucl-th/0109068 v2, 2001.

[60] V. Bernard, T.R. Hemmert, and Ulf-G. Meissner, Nucl. Phys. **A686**, 290 (2001).

[61] N.C. Mukhopadhyay, Phys. Rep., Phys. Lett. **C30**, 1 (1977).

VITA

Jessica Higgins Deseret Clark

Jessica Higgins Deseret Clark was born in Salt Lake City, Utah, on July 24, 1973. She graduated from East Anchorage High School in Anchorage, Alaska in 1991. During her undergraduate education, she spent one year at the University of Edinburgh in Scotland. She received a Bachelor of Science degree with High Honors in physics from the College of William and Mary in Virginia in 1995. She entered the physics graduate program at the College of William and Mary in Virginia in 1995. She received a Master of Science degree in physics from the College of William and Mary in Virginia in 1997. Since 2000 she has served as the Public Outreach Specialist for the American Physical Society in College Park, Maryland. This dissertation was defended on October 25, 2002 at the College of William and Mary in Virginia.